Electron-Lattice Interactions and Ultrafast Structural Dynamics of Solids

Dissertation
zur Erlangung des Grades eines
Doktors der Naturwissenschaften
am Fachbereich Physik
der Freien Universität Berlin

Lutz Waldecker

Berlin 2015

This work was done between October 2011 and October 2015 in the Max-Planck Research group 'Structural and electronic surface dynamics', headed by Dr. Ralph Ernstorfer, associated to the department of Physical Chemistry (Prof. Dr. Martin Wolf) at the Fritz Haber Institute of the Max Planck Society.

Erstgutachter: Dr. Ralph Ernstorfer
Zweitgutachter: Prof. Dr. Dr. h.c. mult. Ludger Wöste
Drittgutachter: Prof. Dr. Martin Aeschlimann

Datum der Disputation: 20.05.2016

Abstract

In this thesis, the interactions of electrons and lattice vibrations of solids are studied. Femtosecond laser pulses are used to prepare non-equilibrium states. The pathway of the following relaxation dynamics is governed by the interplay of electrons and nuclei. Experiments based on the pump-probe scheme allow to study these pathways on their fundamental time-scale and therefore the underlying interaction mechanisms. Complementary femtosecond optical- and diffraction techniques were applied to investigate different aspects of the electronic and structural dynamics. Specifically, an experimental apparatus for femtosecond electron diffraction (FED) was designed, constructed and applied. Four different material systems were studied.

The incoherent scattering of electrons with phonons was investigated in the simple metal aluminium. Using femtosecond electron diffraction, the rate of energy transfer from photoexcited electrons to the lattice was measured as a function of excitation level. The dynamics of the system are modeled with rate equations, describing the energy transfer between electrons and phonons. The data is compared to first principle density functional theory calculations, and a model including temperature- and frequency dependent electron-phonon coupling is developed, quantitatively matching theory and experiment.

Photoexcitation of antimony changes the potential energy surface of the lattice, which directly launches a specific optical phonon mode. Subsequently, this phonon mode decays while simultaneously electrons and other lattice vibrations equilibrate. Here, the excitation and decay of this strongly coupled mode and the competition with incoherent electron-lattice interactions is investigated.

The compound $Ge_2Sb_2Te_5$ (GST) is a prominent member of the class of phase change materials, which are characterized by their large contrast of optical and electronic properties between their metastable amorphous and crystalline phases. Here, an irreversible phase transition from the crystalline to the amorphous state is induced with femtosecond laser pulses. Combining single-shot variations of FED and single-shot femtosecond optical spectroscopy, the first steps of the amorphization process are investigated. Large and immediate changes in the dielectric function are observed, which are followed by a significantly slower heating of the lattice.

Semiconducting transition metal dichalcogenides (TMDCs) are producible in isolated atomic layers, as their atomic structure is highly anisotropic. This anisotropy is reflected in its properties and becomes most pronounced in the isolated monolayers. Here, different electronically excited states are created by different laser excitation conditions, and the subsequent coupling to lattice vibrations is studied, constituting the basis for future experiments on layered materials and heterostructures.

Kurzfassung

In dieser Arbeit werden die Wechselwirkungen zwischen Elektronen und Gitteratomen in Festkörpern untersucht. Ungleichgewichts-Zustände werden hierzu mit Femtosekunden Laserimpulsen präpariert. Der Verlauf der folgenden Relaxationsprozesse hängt dabei von den Wechselwirkungen zwischen Elektronen und Kristallgitter ab. Zeitaufgelöste Messungen, basierend auf dem Pump-Abfrage-Prinzip, ermöglichen es, diese Prozesse auf der ihr eigenen Zeitskala zu beobachten. Im Zuge dieser Arbeit wurden komplementäre optische und Beugungs-Methoden entwickelt und angewendet um verschiedene Aspekte der strukturellen und optischen Relaxationsdynamiken zu untersuchen.

Die inkohärenten Streuprozesse von Elektronen mit Phononen wurden in Aluminium als Funktion der Anregungsdichte mit Femtosekunden-Elektronenbeugung untersucht. Die Dynamik des Systems wird mit Ratengleichungen, die den Energieübertrag beschreiben, modelliert. Die Daten werden mit *ab initio* Dichtefunktionaltheorie Rechnungen verglichen. Ein Modell, welches temperatur- und frequenzabhängige Kopplungsparameter zulässt, wird entwickelt und bringt Theorie und Experiment in quantitative Übereinstimmung.

Photoanregung von Antimon ändert die Potenzialfläche der Gitteratome, was zur direkten Anregung einer spezifischen Phononenmode führt. Im darauffolgenden klingt die Anregung dieser Phononen ab, und Elektronen und Gitterschwingungen equilibrieren. Die Anregung und der Zerfall dieser stark gekoppelten Phononen und der Zusammenhang mit inkohärenten Elektron-Phonon Wechselwirkungen wird untersucht.

Die Verbindung $Ge_2Sb_2Te_5$ (GST) ist ein prominenter Vertreter der Klasse von Phasenwechselmaterialien, welche sich durch einen großen optischen Kontrast zwischen ihren metastabilen kristallinen und amorphen Phasen auszeichnen. Mit einer Kombination von Einzelschuss-Varianten von fs-Elektronenbeugung und optischer Spektroskopie werden die ersten Schritte der laserinduzierten Amorphisation von GST untersucht. Es wird gezeigt, dass durch Photoanregung große und quasi-instantane Änderungen der dielektrischen Funktion hervorgerufen werden, welche von einem deutlich langsameren Energieübertrag an das Kristallgitter gefolgt werden.

Halbleitende Übergangsmetall-Dichalkogenide (TMDCs) sind aufgrund ihrer anisotropen Struktur in einzelnen atomaren Schichten herstellbar. Diese Anisotropie spiegelt sich in ihren Eigenschaften wider, und ist in isolierten Einzellagen besonders ausgeprägt. Unterschiedliche elektronisch angeregte Zustände werden hier durch Laseranregung erzeugt, und die darauffolgende Kopplung mit Gitterschwingungen studiert, was als Basis für künftige Experimente an Einzellagen dienen kann.

Contents

1. Introduction

The properties of solids, molecules and biological systems are determined by the mutual interaction between the atoms, of which they are composed. Understanding microscopic processes and macroscopic functionality of matter thus requires the understanding of the interplay of its constituents. The large number of particles in condensed matter systems makes the description of these interactions a highly complex problem.

One standard approach in the description of condensed matter is to separate the motion of electrons and the ones of the atomic cores ('Born-Oppenheimer' or 'adiabatic' approximation). Caused by the large difference in mass, electrons move much faster than the nuclei. For the electrons, the forces exerted by the nuclei therefore only change slowly (i.e. adiabatically). The nuclei themselves feel an effective force, which is the time-average of the forces that the fast moving electrons apply on them. By decoupling the two subsystems, interactions between them are neglected and need to be introduced again as electron-lattice interactions. These interactions determine fundamental properties in solid state systems, ranging from electrical- and heat transport to the emergence of superconductivity via Cooper-pairs, the existence of Peierls-distorted materials and charge density wave systems. Understanding these interactions is therefore equally important, both, for fundamental research, as well as in the design and implementation of new materials in devices.

Without external perturbation, the forces of all particles in a material balance out, and its macroscopic properties are stationary, i.e. the system is in equilibrium. This means that, while the physical properties of a material can be measured directly, the underlying interactions can not, but rather need to be inferred indirectly. Where there is several techniques to do so (e.g. by analyzing tunneling spectra), an intuitive and direct approach is to study the time-evolution of a system after applying a sudden external stimulus. With basic atomic processes evolving on a femto- to picosecond (10^{-15} – 10^{-12} s) timescale, the realization of a time-resolved experiment measuring fundamental atomic properties only became possible with the availability of short flashes of light in the early 1990's, when self mode-locked Ti:Sapphire laser were developed. In the applied time-resolved experiments, a laser pulse is used to initiate a reaction (pump pulse) and

a second, delayed one (probe pulse) is used to measure the state of the system after a certain time delay. By repetition of the experiment with different delays between the pulses, a sequence of snapshots of the temporal evolution of the material is recorded.

Pump laser pulses employed are mostly in the visible to near infrared spectral region and therefore mostly create electronic excitations. In this way they induce non-equilibrium situations, in which interactions between particles do not cancel out, but cause a net energy transfer between them and thus a relaxation towards a new equilibrium. The strength of the laser excitation determines the setting for the subsequent relaxation pathway, and therefore its experimental determination. In the case of relatively low excitation, a measurement can be seen as an experimental counterpart to perturbation theory, in which one induces small deviations and infers ground-state or quasi-equilibrium interactions from the relaxation dynamics. Higher excitation levels can be used to study metastable or transient states which are short lived, e.g. an intermediate step of an irreversible phase transition or of a chemical reaction. The isolated investigation of such transient states is only possible with time-resolved techniques.

The evolution of different microscopic or macroscopic properties of solids can be measured by employing diverse probe pulses, which interact with the sample in a certain way. Laser pulses in the near infrared to the ultraviolet spectral region mainly interact with the outer electrons of the solid, i.e. electrons in the valence- or conduction band. Time-resolved photoemission experiments employ those pulses and can be used to map the evolution of electronic states. All optical experiments indirectly measure properties of the electronic structure as well, as here changes to the optical pulses through their interaction with the electrons are detected. X-rays and charged massive particles, like electrons, interact with all electrons of the material, i.e. with its electronic density or the electrostatic potential, respectively. Except for the lightest elements, these are dominated by the core-electrons, which are situated around the nuclei and directly follow their motions. X-rays and charged particles are therefore most sensitive to lattice properties, like the local arrangement of atoms, their long-range order and vibrational excitations. The latter two have in this thesis been investigated with diffraction techniques, which have been successfully applied to study the atomic structure of matter since the discovery of diffraction patterns by M. von Laue and W. Bragg in the early 1900's. The combination of the pump-probe scheme with diffraction techniques, by the creation of short x-ray or electron probe pulses, therefore allows to study the evolution of lattice properties on their fundamental length- and timescale. An illustration, summarizing the introduction to the employed techniques, and the fundamental physical properties of solids accessible with them, is shown in figure 1.1.

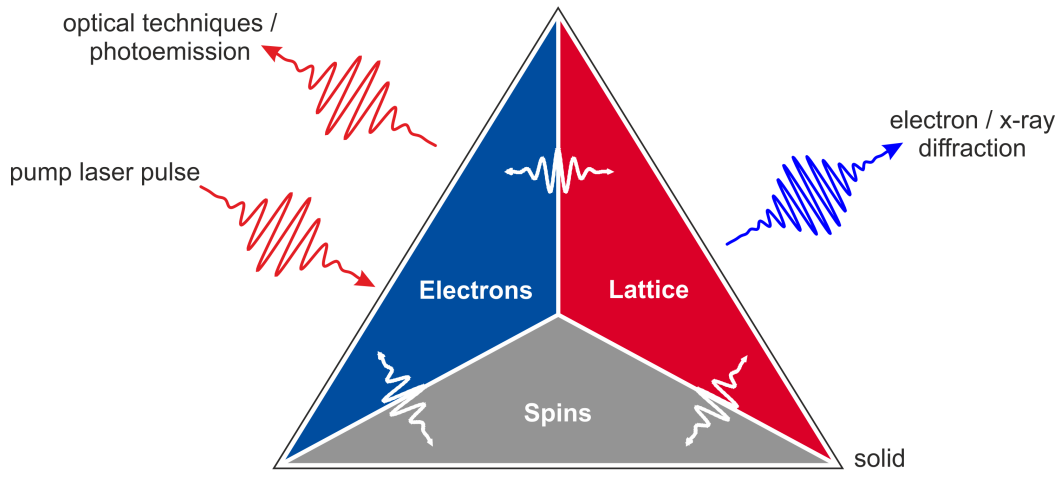

Figure 1.1.: Depiction of the principle of time-resolved experiments, as applied in this thesis. A pump laser pulse excites the electrons of a solid, driving the system out of equilibrium. By the interactions of electrons with lattice vibrations, this results in a relaxation of the system towards a new state. Spin excitations are important in some systems, but are beyond the scope of this work. Optical probe pulses are applied to probe the state of the electronic system at certain time-delays and electron diffraction measurements are used to investigate the lattice dynamics. The dynamics are analyzed to draw conclusions about the interactions of electrons and lattice.

The coupling of electrons to the lattice manifests itself by a transfer of energy between them. With time-resolved techniques, this transfer can be followed in real-time by observing changes in the electronic system or by measuring the energy arriving in the lattice. In this thesis, I report on the investigation of the interaction of laser-excited electrons with lattice vibrations in four different material systems in the light of different open questions. For aluminium, which is a prototype solid state system due to its simple lattice and electronic structure, the energy transfer due to incoherent electron-phonon collisions is investigated and a microscopic picture is obtained by comparison to first principle calculations. In antimony, photoexcitation changes the potential energy surface of the atoms, which launches phonons by the DECP (displacive excitation of coherent phonons) mechanism. The excitation and decay of those phonons, and the coupling to other lattice vibrations is investigated. The evolution of optical properties and the long-range order of the lattice of $Ge_2Sb_2Te_5$, a member of the class of phase change materials, are measured. By extending the measurements to excitation levels driving a photoinduced phase-transition between its two metastable crystalline and amorphous phases, the measurements contribute to a long-standing discussion about the pathway which the transition takes. The difference in the coupling of localized and delocal-

ized electronic states to phononic vibrations is examined in the layered semiconducting transition metal dichalcogenide WSe_2. All aforementioned studies became possible by designing and implementing a setup for femtosecond electron diffraction, which shows some major improvements in time-resolution over previously available setups.

The following gives an outline of this thesis and a short introduction to the material systems which were investigated.

Development of a femtosecond electron diffractometer

In recent years, the concept of pump-probe experiments has been applied in a large variety of experiments. Also diffraction techniques have been combined with the pump-probe scheme, with the aim to visualize the evolution of a crystal structure after photoexcitation with a laser pulse. Whereas pulsed x-ray sources with high brightness are realized in large-scale facilities, such as free-electron lasers or synchrotrons, laboratory-scale x-ray experiments suffer from comparably low photon numbers [Els14]. The high scattering cross section of electrons loosens this constraint and allows to build time-resolved electron diffraction experiments in very compact laboratory scale setups [Mil10].

One main focus in the development of electron diffraction setups is the time-resolution, which has so far been limited by electron pulse durations on the sample position. These ranged from few picoseconds in early setups [Wil84, Dan94] to few-hundreds of femtoseconds in some recent designs [Heb08, Kas10]. Calculations have shown that pulse durations below 100 fs are easily achievable for pulses containing a single electron [Aid10]. However, due to the repulsive action of Coulomb-forces between electrons, which lead to a temporal broadening of the pulses [Siw02], it remains a challenge to achieve similar pulse durations for higher bunch charges.

In chapter 2, a setup for femtosecond electron diffraction is described, which was designed and implemented in the course of this work. Its design aims at minimizing the electron propagation distance before the sample and therefore reduces the broadening that electron pulses experience [Wal15a]. Multi-body simulations were performed to calculate the propagation of the electrons, suggesting that pulse durations of around 100 fs can be achieved with pulses containing more than 10^3 electrons. This constitutes a significant improvement in time-resolution achievable in table-top electron diffraction experiments, enabling the studies performed in the following.

Electron-phonon coupling in Al and Sb

A generally valid, microscopic description of the out-of-equilibrium dynamics of materials would require the precise knowledge of the distributions of electrons and phonons at all times as well as their exact interactions. The high dimensionality of this problem, however, renders a universally valid description virtually impossible, and requires (material-specific) approximations. The most common solution is to assume thermal distributions for electrons and phonons, i.e. to apply Fermi-Dirac and Bose-Einstein statistics. The evolution of non-equilibrium states is then described by applying a two-temperature model (TTM), which describes the temporal evolution of the two distributions by the evolution of two temperatures [Ani74]. This approach is followed in thousands of publications, modeling the non-equilibrium dynamics of materials.

Simple metals, such as aluminium, constitute a model system in theoretical and experimental solid state physics. Their model character results from their electronic structure, which is well described as a free electron gas, and their cubic atomic arrangement with a one-atomic unit cell. Here, the applicability of the TTM to the description of the out-of-equilibrium dynamics of the simple metal aluminium is examined. By combining electron diffraction experiments with first principle calculations performed in a collaboration by J. Vorberger (MPI-PKS, Dresden), it is found that the notion of Bose-Einstein statistics describing the phonon population at all times, is improper. This is a consequence of the coupling strength from electrons to phonons which differs between different phonon branches. A refined model, which allows for non-BE phonon distributions, the 'non-thermal lattice model' (NLM), is introduced. By considering the coupling between the electrons and the three phonon branches individually, the model is able to describe the key mechanism transiently leading to a non-thermal lattice. A guideline is given, for which materials the NLM is expected to be applicable or even a necessary refinement to accurately describe the out-of equilibrium dynamics.

Strong electron-lattice correlations lead to a more complicated electronic (and lattice) structure in antimony. Photoexcitation of electrons has pronounced effects on both, which makes the description of the non-equilibrium dynamics even more complex. A quasi-immediate shift of the lattice potential energy surface, due to the excitation of electrons, triggers atoms to move towards the new minimum, around which they start to oscillate. This motion can be described as a single, coherently excited, phonon mode [Che90, Zei92].

At the same time, electrons release energy to a broad range of phonons via incoherent electron-phonon scattering processes. Whereas the excitation of the coherent phonon mode has been studied for a wide range of excitation conditions, the relaxation

dynamics of electrons via incoherent electron-phonon scattering and the decay of the coherent phonons have not been measured directly. In this chapter, electron diffraction measurements are applied on polycrystalline samples of antimony, which allow to simultaneously follow the excitation of different phonon modes.

Photoinduced crystalline to amorphous phase transition of $Ge_2Sb_2Te_5$

The ternary compound $Ge_2Sb_2Te_5$ (GST) belongs to the class of phase change materials (PCMs), which combine a unique set of properties. At room temperature, they exhibit long-lived, metastable crystalline and amorphous states with vastly different optical and electrical properties. Light or current pulses can be used to reversibly switch the material from one into the other state. This combination is routinely exploited in data storage media, such as CDs or DVDs, and the material has a wealth of new opto-electronic applications on the horizon [Lok14, Hos14].

Despite their wide-spread use, the microscopic origin of the optical and electrical contrast between the two phases is debated [Shp08, Hua10]. Whereas the established way to initiate the phase transition in devices is to melt the material and then control the cooling rate [Koh06], the existence of optically induced non-thermal phase transitions has been predicted by several groups [ST98, Kol04, Kol11]. So far, no direct study of the pathway of crystalline order during the photoinduced phase transition was available.

In this chapter, femtosecond optical spectroscopy and electron diffraction measurements are combined to study the evolution of the optical properties and the crystalline structure after photoexcitation. The studies are conducted at a wide range of excitation conditions, from the regime of reversible excitation to the excitation densities inducing the phase transition. In the latter, single pump laser pulse cause irreversible changes to the sample, and single-shot variations of the optical and diffraction measurements are applied. These allow to follow the dynamics of optical and structural properties as the phase transition proceeds.

Electron-lattice coupling in semiconducting transition metal dichalcogenides

The discovery of isolated, atomically thin graphene [Nov04] and its unusual characteristics has triggered tremendous further research on its basic properties, its usability in devices and in the identification of other two-dimensional materials. Shortly later, the class of layered transition metal dichalcogenides (TMDCs) was found to be producible in stable monolayers [Nov05b] as well. As two-dimensional semiconductors, they con-

stitute an especially interesting class for nanoscale optical and electronic devices, as concepts of the well-established semiconductor technology can be applied.

The reduced dimensionality of these materials has very pronounced effects on macroscopic properties, like the emergence of strong luminescence in monolayers, caused by the transition from an indirect- to a direct semiconductor, which all semiconducting TMDCs undergo [Jin13]. Large excitonic binding energies and a large spin-splitting of the valence bands constitute further particularities of the materials. Such special electronic features are expected to also effect other fundamental properties, like the coupling to lattice vibrations, which themselves should constitute an anisotropy.

In this chapter, different electronic states are prepared by the pump laser pulses. Driving an excitonic resonance, electronic states are populated, which are localized in the Brillouin zone and interband transitions are driven to create a more delocalized electronic population. The coupling of these differently prepared excitations to lattice vibrations is studied in the TMDC WSe_2. The experiments constitute a basis for future work on monolayer samples as well as heterostructures of different layered materials [Gei13].

2. Experimental techniques

The techniques applied in the course of this work are based on the pump-probe scheme, in which femtosecond laser-pulses are used to photoexcite electrons in a specimen and probe pulses are sampled over different delay-times, acquiring snap-shots of the evolution of the studied property. This chapter is intended to introduce the experimental approaches followed in this work.

The evolution of vibrational excitations of the crystal lattice is investigated with femtosecond electron diffraction (FED). Since the planning and implementation of a setup for FED has been a considerable part of this work, it will be described in detail in the following section. Simulations of the propagation of electron pulses are presented, characterizing the electron pulse duration at the sample position and therefore the achievable time-resolution of the experiment. The dynamics of the optical properties have been measured by femtosecond optical spectroscopy, which is introduced in section 2.2. The measurements on phase change materials, presented in chapter 5, aimed at understanding an irreversible phase transition, for which single-shot variations of both types of measurements have been employed. These are described in sections 2.1.4 and in 2.2.3, respectively.

Parts of this chapter have been published in [Wal15a] and [Wal15b].

2.1. Femtosecond electron diffraction

Diffraction techniques have, for many decades, been successfully applied to study the atomic structure of matter. The determination of atomic structure by neutrons, x-rays and electrons is therefore discussed in most textbooks on solid state physics [Kit05, Ash76]. A more specific introduction to the physics of electron-matter interaction and electron diffraction can be found in [Pen04].

Time-resolved electron diffraction experiments are based on the pump-probe measurement scheme with optical pump laser pulses photoexciting the sample and synchronized

electron pulses which diffract off it, probing the lattice structure at a specific time delay. Early setups were developed in the 1980's and 1990's [Wil84, Dan94] and achieved few picoseconds of time-resolution. Despite growing interest and a lot of ongoing development in recent years, it remains a challenge to achieve short electron pulses with high electron numbers at the sample position. Whereas calculations have shown that pulses containing a single electron can have durations well below 100 fs [Aid10], the repelling action of Coulomb forces between electrons stretch the pulses as they propagate. The temporal broadening of electrons can be described in a phase-space picture of the electron-pulse [Siw02] (momentum in propagation direction vs position in propagation direction) . During propagation, the electron pulse develops a linear dependence of momentum to position within the pulse, with electrons in the front of the pulse having higher momenta. This effect comes due to the vacuum dispersion of electrons, but is amplified by the Coulomb forces. The effect is therefore more pronounced the more electrons a pulse contains. Theoretically, this linear distribution can be inverted, such that the electrons at the trailing edge have larger momenta, which leads to a recompression of the pulse during further propagation. Therefore, several schemes have been proposed [Fil06, vO07, Kas09]. One scheme, using a radio frequency cavity to decelerate the leading and accelerate the trailing electrons, has recently been implemented by a few groups [Cha12, Gao12, Man12]. Even though pulse lengths below 100 fs can theoretically be achieved for pulses containing up to 10^6 electrons [vO07], the time resolution in those experiments is limited to few hundreds of femtoseconds, caused by jitter in the synchronization of RF-cavity and the laser pump pulses [Cha12, Gao12].

The setup presented in the following is based on a different approach, which was first pursued in the group of R. J. D. Miller (see e.g. [Siw02, Heb06]). By minimizing the propagation distance of the electron pulses towards the sample, the action of repulsive Coulomb forces and therefore the temporal broadening is reduced [Wal15a]. This concept led to the implementation of a diffraction setup with an overall electron pulse propagation distance of only 10 mm for electron energies up to 100 keV. To calculate the propagation of electron pulses and evaluate how experimentally accessible parameters influence the electron pulse duration at the sample position of this setup, multi-body particle tracing simulations are presented in section 2.1.3.

2.1.1. Optical- and diffraction setup

Fig. 2.1 shows a schematic drawing of the electron diffraction setup and the most important optical elements. A Ti:sapphire multi-pass amplified laser system (Femtolasers Femtopower PRO) is used as the main laser source. It provides laser pulses with a tem-

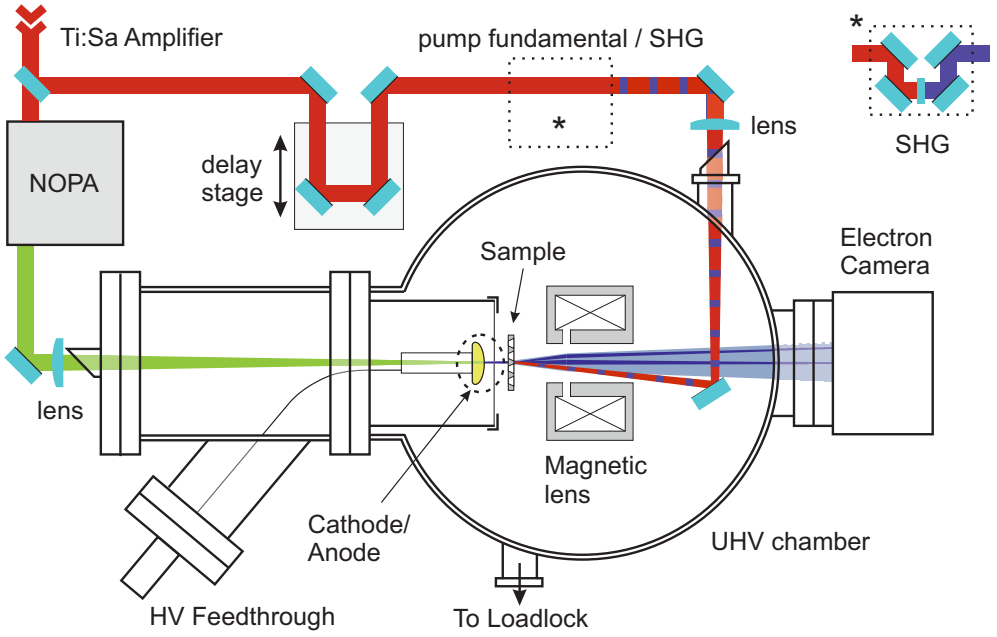

Figure 2.1.: Schematic of the experimental setup for femtosecond electron diffraction. A femtosecond laser delivers pump- and probe pulses. In the probe-arm, it drives a NOPA, the pulses of which emit electrons from a photocathode in a two-photon process. The field between cathode and anode accelerates the electron pulses, which diffract of the sample and are detected with an electron camera. A delay stage changes the pump-probe delay, allowing to record time-resolved data. By inserting a set of mirrors, the pump wavelength can be changed from the fundamental (800 nm) to the second harmonic (400 nm) of the laser.

poral width of 30 fs and a pulse energy of up to 800 µJ. Its central wavelength is 800 nm (photon energy 1.55 eV) and the repetition rate of the laser is 1 kHz. The lasers pulse energy can variably be divided between the pump- and the probe arm by a half-wave plate and a polarizing beamsplitter. In normal operation, 60-70 µJ are sent into the probe arm where the laser drives a custom built non-collinear optical parametric amplifier [Wil97], which amplifies pulses with the central wavelength tunable in the visible spectral region. The layout of the NOPA is shown in figure 2.2 a). Typically, the NOPA is operated in a wavelength range between $500 - 600$ nm central wavelength. A spectrum of the NOPA is shown in 2.2 b). The output is compressed in a prism compressor and the pulse duration after compression is measured with an autocorrelator to be in the range of $30 - 40$ fs (an autocorrelation trace is plotted in 2.2 c)). The compressed pulses are used to photo-emit electrons from a photocathode, which are subsequently accelerated up to energies of 100 keV in the electron gun, which they eventually leave through a hole in the anode. Since the electron gun is the heart of the diffraction setup,

it will be described in detail in section 2.1.2 and parameters influencing the electron pulse duration will be discussed in section 2.1.3.

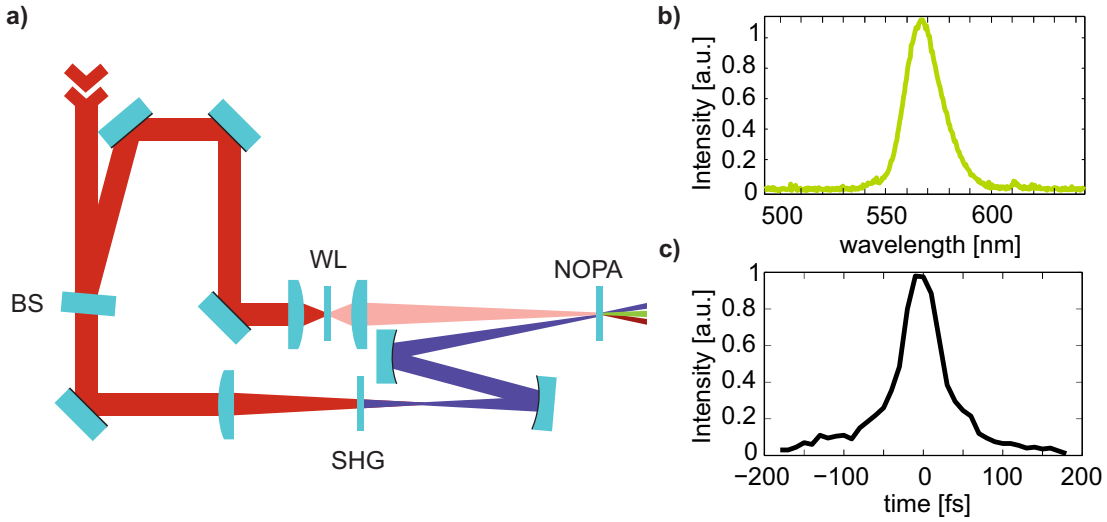

Figure 2.2.: **a)** Schematic of the noncollinear optical parametric amplifier. WL: white light generation, BS: beam splitter, SHG: second harmonic generation, NOPA: crystal for optical parametric amplification. **b)** Typical spectrum of the NOPA. The central wavelength is chosen to be only slightly above the workfunction of the cathode. **c)** Autocorrelation trace of the output of the NOPA. The pulse duration is approximately 40 fs.

Pump laser pulses

The pulse energy of the pump pulses can be adjusted with a pair of a motorized wave-plate and a thin film polarizer. The pump wavelength can be conveniently changed to the second harmonic (400 nm central wavelength) by changing the beam path with a set of three removable mirrors. The two beam paths are adjusted such that their optical length is similar. The second harmonic is generated by focusing the pump pulses into a BBO crystal (an introduction to non-linear optics is found in many textbooks, see e.g. [Boy08]), and the remaining fundamental is filtered with an accordingly coated dielectric mirror. The dispersion of the 2nd harmonic after the BBO is kept small by using a reflective curved mirror for recollimation and a CaF_2 lens for focusing of the pulses. The window to the vacuum chamber is made of a 2 mm thick slab of CaF_2 as well, which shows a comparably low dispersion at 400 nm. Without recompression of the 2nd harmonic pulses, a pulse duration of below 100 fs on the sample was calculated for optimally compressed 800 nm pulses.

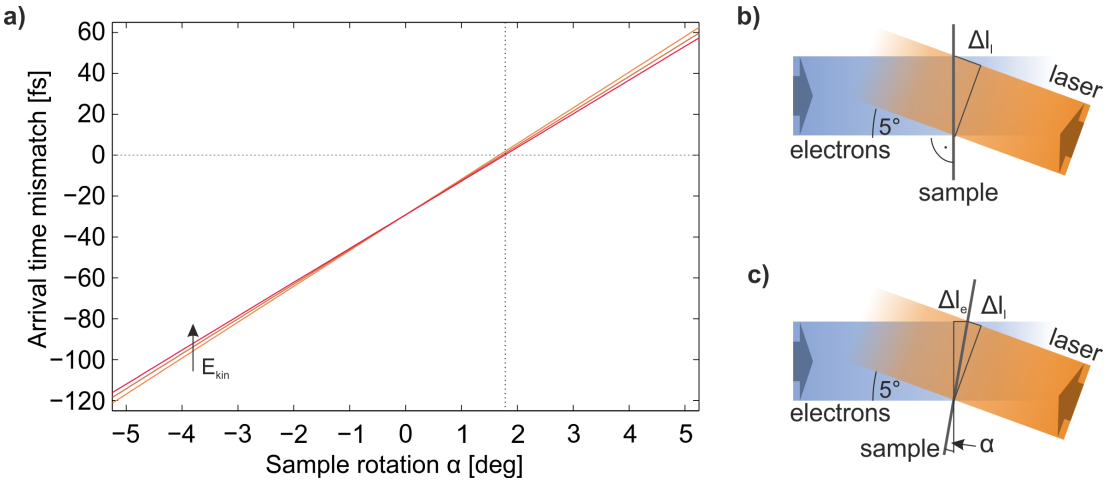

Figure 2.3.: **a)** Difference in arriving time of pump and electron probe pulses on two sample positions spaced by 100 µm as a function of sample rotation. The kinetic energies of the electrons are 80, 90 and 100 keV. An angle of zero degrees denotes normal incidence of the electron pulses onto the sample. **b)** & **c)** Sketch of the origin of the arrival time mismatch. At normal incidence of the electrons, one side of the laser pulse travels Δl_l further than the other side. The sample can be tilted at an angle α, such that $\Delta l_e / v_e = \Delta l_l / c$.

The pump pulses are sent over a delay stage that changes the relative arrival time of pump and probe, and are then focused onto the sample. In the compact design described here, samples are close to the electron gun and the pump pulses hit the sample from the opposite side as the probe. Due to the typical thicknesses of the samples of below 100 nm, the excitation profile is homogeneous for most materials and differences in arrival time due to counter-propagating beams can be neglected. The angle of the pump pulses with respect to electron propagation axis is approximately 5 degrees. The angle of the sample defines the mismatch in arrival time of pump and probe pulses on opposite sides of the sample. For two points, separated by 100 µm, the difference in arrival time is shown in figure 2.3 a) for different angles of the sample with respect to the electron propagation axis. It can be seen that a rotation of a few degrees can induce a temporal degradation of several tens of femtoseconds, the origin of which is schematically drawn in b). The pump and probe arrive simultaneously on all positions of the sample, when $\Delta l_e / v_e = \Delta l_l / c$, where v_e is the velocity of the electrons and Δl_i are differences of distances of laser and electrons as defined in the sketch of figure 2.3 c). At an electron energy of 100 keV, a sample rotation of 1.7 degrees fulfills this condition. This angle does only differ by around 0.2 ° when decreasing the kinetic energy from 100 keV to 80 keV.

Samples

Electrons leaving the gun diffract off a sample, and diffraction images are taken in transmission geometry. Therefore, thin samples are required with typical thicknesses that range from single atomic layers up to 100 nm. In most of the experiments of this work, standard TEM-grids were used to support these films. In the experiments of chapter 5, irreversible changes were induced to to the samples by single laser shots, what made large sample areas necessary. These large samples need to be shifted to a new spot after each laser shot. In order not to change the zero time of the experiment, the interaction region on the sample of the laser- and the electron pulses is required not to move. The support for the samples therefore needs to be flat on a low µm level (10 µm corresponds to 100 fs in the geometry with counterpropagating pulses and electrons with 100 keV).

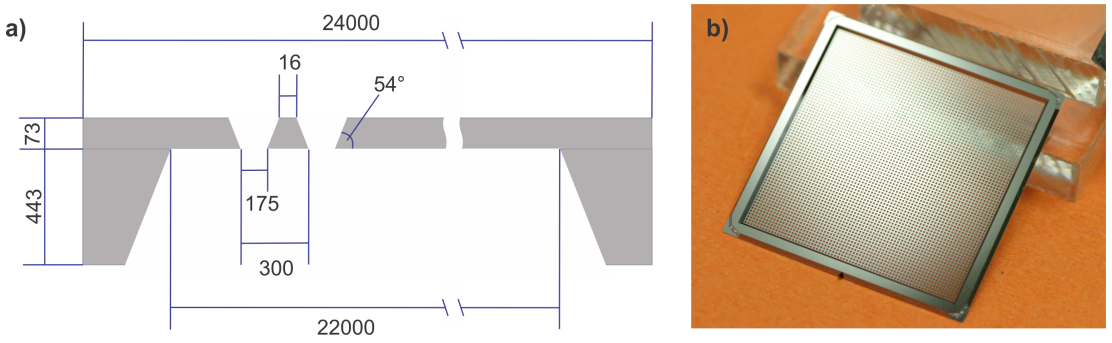

Figure 2.4.: a) Schematic cut through the custom-made Si-grids used as a support for big samples. The dimensions are given in µm. The angle of 54 degrees is given by the KOH etching technique. **b)** Photograph of the grid. Taken by L. Andricek.

Large area grids have been designed and produced in a collaboration with L. Andricek of the Halbleiterlabor der Max-Planck-Gesellschaft. A schematic drawing of the grid, including dimensions, and a photograph of the grids are shown in figure 2.4. The grids have 70 times 70 equally sized square holes, which are etched in a 73 µm thick Si-wafer. The etching is done with potassium hydroxide (KOH), resulting in the typical angles of the holes of 54.7 degrees. The thin wafer with the holes is bonded onto a frame, etched out of a thicker wafer, to increase the stability and the flatness of the sample. These grids can support a sample area of up to 21^2 mm^2 with a flatness of a few micrometers.

Both types of sample grids are supported by the same sample mount, which can be transferred in- and out of the chamber with a transfer-rod via a load-lock chamber. Thus, the main chamber does not need to be vented in normal operation and pressures typically reach values in the low 10^{-9} mbar range.

The samples can be translated in three dimensions with a motorized xyz-translation stage and tip and tilt angles can be controlled by two additional motors. The distance between anode and sample can be varied with the translation stage. The closest position to the gun, limited by the thickness of the sample mount, is 2 mm. At this position, the overall propagation distance of the electron pulse is as short as 10 mm.

The temperature of the samples can be changed by cooling the sample mount, which is connected by a copper braid to a reservoir that can be filled with liquid nitrogen. Since so far no heating system has been installed, the temperature range achievable is limited to room temperature and the temperature which is reached when cooling with liquid nitrogen. This temperature depends on the sample geometry and the quality of the heat connection to the mount and will therefore differ from sample to sample. The temperature of the mount has been monitored with a thermocouple as a function of time after starting the cooling with liquid nitrogen. It reached a steady state after one hour at a temperature of 195 K. The temperature of the sample will probably be a bit higher due to radiative heating of the surrounding, but might be on the order of 200 K. A better insulation of the sample mount and a radiation shield around the sample might decrease the reachable temperatures.

Magnetic lens

To reduce the propagation distance of the electron pulse towards the sample, the magnetic lens, which focuses the electrons onto the detector, is placed behind the sample, in contrast to earlier setups with a lens before the sample [Dwy06]. This configuration of the setup is adapted from a layout introduced recently [Ger12, Ger15]. The design significantly decreases the electron bunch propagation distance and avoids temporal distortions due to path length differences induced by the magnetic lens [Wen12]. The position of the lens is controlled by a three-axis manipulator, with which the position of the lens can be set to be centered with the electron beam. The lens has a magnetic steel cladding with a gap (shrouded coil, see e.g. [Lie55]) and a hole diameter of 40 mm. Spherical aberrations, intrinsic to magnetic lenses [Mar47], are smaller the closer the lens is placed to the sample, since the beam diameter increases with propagation distance. Simulations of the focusing of diffracted beams have in addition been carried out with the simulation package GPT (the simulation package is described in section 2.1.3). These show that different diffraction orders are focused at slightly different positions in propagation direction. The practical alignment of the setup is therefore done such, that the low order diffraction orders with the highest intensity are best separated.

The spatial resolution of the diffraction images depends on the transverse coherence of the electron beam as well as on the resolution of the imaging system, consisting of the magnetic lens and the camera. By taking the width of a diffraction spot of a sample with a well known lattice cell parameter, one can estimate the coherence length [Kir13b]. In fact, this number is a lower bound of the coherence of the electron pulse, since it can be reduced by the imaging system. Figure 2.5 shows a diffraction image of the layered material WSe_2. From this image the coherence at the sample position is derived, following Kirchner et al. [Kir13b], by comparing the ratio of peak width s_i to peak separation d with a simulated diffraction pattern of a coherently illuminated diffraction grid with N slits [Bor01]. At a sample position of 12 mm behind the anode, the coherence length is estimated to be 6 nm. In diffraction images taken closer to the gun, where the temporal resolution is expected to be better, the ratio w/d increases. Since the beam diameter is small here, also the coherence length is observed to be smaller [Kir13b]. However, a contribution of the imaging system to the decreased resolution can not be ruled out.

Having a lens behind the sample enables imaging a magnified real-space image onto the detector, what allows for easy sample positioning and characterization.

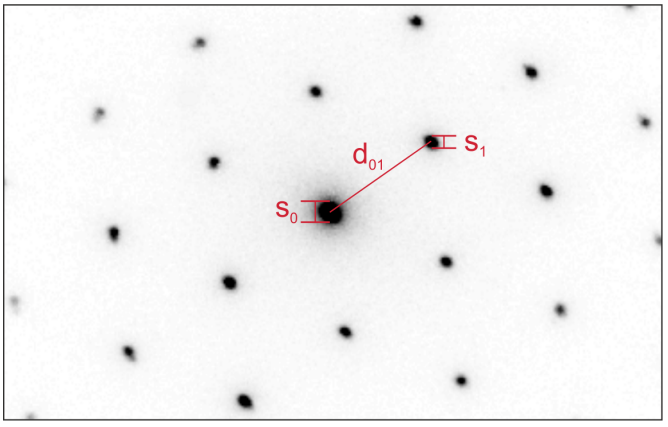

Figure 2.5.: Detail of a diffraction pattern of WSe_2. The spot sizes of the zero order s_0 and first order s_1 diffraction peaks, as well as their spacing d_{01}, are indicated, from which the coherence of the electron pulses can be estimated.

Detector

An efficient detection system is a central part of every experiment. For the diffraction setup, specifically, a detector with a high spatial resolution, high dynamic range, a fast read-out and low noise as well an insensitivity to light is wanted. Whereas different

devices show some advantages over others, at the time of planning the experiment, a commercial electron camera (TemCam F416, TVIPS), was considered to be the best solution available. It consists of a phosphor screen that is fiber-coupled to a CMOS chip with 16 MPixels. The camera is capable of every-electron detection if the raw images are properly analyzed (a detailed description of how the diffraction images are processed is given in Appendix A). The maximum read out speed is around 8 fps (region of interest and binning), which was higher than any CCD chip available. The phosphor screen gives a significantly higher dynamic range than cameras for direct-electron detection. With a few companies investing in the development of direct electron detection cameras, further improvements in read-out speed, and thus dynamic range, are expected. The front of the phosphor screen was coated, on delivery, with a thin film of 'black aluminium' (no further details were given by TVIPS) to make the camera insensitive to visible light. However, the thickness was not sufficient to block scattered light from the laser pump-pulses. For a better shielding, the thickness of the film was increased by vacuum-deposition of a 50 nm thick layer of aluminium on the front of the phosphor screen. The additional film decreased the sensitivity to light markedly. However, for a complete shielding an even thicker layer would be needed.

2.1.2. Electron gun

The electron gun is one of the central parts of the electron diffraction setup. It provides femtosecond electron pulses, which are optically synchronized to the pump laser pulse and can therefore be used in the diffraction experiments.

The gun consists of a photocathode, which is set to a negative potential. The accelerating field is created by the potential difference to a grounded anode, which is mounted at a well defined distance. Electrons are emitted into the high field region by illumination of the cathode with a laser pulse and are subsequently accelerated by the static field. The pulses eventually leave the acceleration region through a small hole in the anode and propagate towards the sample.

The compact design of the entire diffraction setup is continued in the electron gun. For the desired electron energy of 100 keV, the anode to cathode distance is minimized to the smallest distance for which no field emission is observed. In the current design, 8 mm could be realized. The geometry of cathode and anode was designed to have the maximum field in the center of the cathode, where the electrons are created. The anode is made from a highly flat and polished 5 inch Si-wafer, which has a laser-drilled hole of 150 µm in its center. The cathode's shape is an approximation to the shape of the uniform field electrode described by Bruce [Bru47]. The field strength at the maximum

voltage of 100 kV reaches 12.5 MV/m and is therefore only slightly smaller than the field for vacuum break-through of a perfectly homogeneous surface, which has been reported to be on the order of 20 MV/m [Lat95]. A simulation of the field distribution on the cathodes surface, done with COMSOL Multiphysics, is shown in figure 2.6 b).

With the front side of the gun being blocked by the anode, photoemission of electrons needs to done with a laser pulse arriving from the backside. The cathode therefore has a hole in its center, in which a 5 mm thick sapphire plate has been fitted, such that its surface is planarly aligned with the cathodes surface. The entire cathode is then coated with a 20-30 nm thick film of gold, on top of a 2 nm thick film of chromium, which is used as a buffer layer for increased adhesion of gold on sapphire. The vacuum deposition of the films is done at a base pressure of $10^{-}5$ mbar. The films therefore might contain low amounts of oxygen and other contaminations. All parts of the cathode are polished to prevent sharp edges which would facilitate undesirable field emission. Furthermore, the few µm wide gap between the sapphire plate and the metal body of the photocathode, which arises from the assembly process, is filled with a vacuum compatible glue before coating.

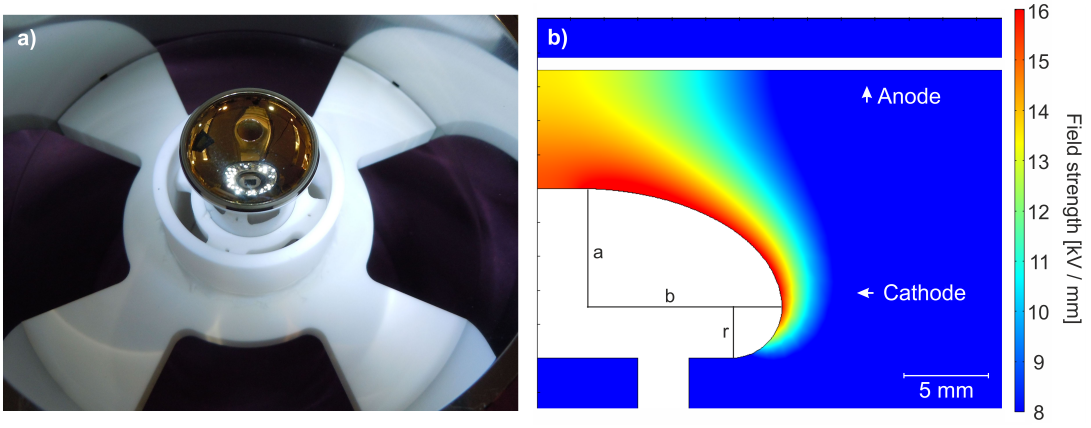

Figure 2.6.: **a)** Photograph of the photocathode mounted in the gun with the anode removed. The white ceramic keeps the cathode in the center of the gun and insulates it from the housing. **b)** Half-profile of the photocathode (the left edge is the axis of rotational symmetry) and simulated electric field strength on the surface.

Electrons are emitted by illuminating the gold-coated sapphire of the photocathode from the back side with the output of the NOPA. The work function of the gold film is measured by changing the wavelength of the NOPA and determining the photon energy at which no electrons are emitted any more. The work function changes slightly between

different cathodes, but typical values are around 4.4 eV. This value is much lower than literature values for gold, which report a work function of 5.3 eV [Sac66]. This might be caused by several effects, e.g. the use of thin films and possible contamination of the films due to the preparation conditions. On top, the Schottky-effect lowers the work function of the gold film by roughly $\Delta W \approx 130\,\mathrm{meV}$ at fields of 12.5 MV/m.

The transverse and longitudinal coherence of an electron pulse increases for lower excess energy in the emission process [Mic08]. The excess energy of the electrons can be controlled by changing the central wavelength of the NOPA. Since the NOPA is operated to produce pulses in the visible spectral region, two photons are needed to emit electrons from the photocathode. In normal operation, the central photon energy is adjusted to be 2.2 eV (central wavelength of 565 nm), such that an electron absorbing two photons initially, i.e. before acceleration through the static field, has little kinetic energy.

The laser pulses used for photoemission have a certain temporal and spectral width, which are intrinsically connected by the uncertainty relation. In the process of photoemission, both widths are imprinted on the electron bunch. The way in which these parameters influence the electron pulseduration at the sample position is investigated in section 2.1.3. A typical spectrum and an autocorrelation trace can be found in figure 2.2 b) and c).

The potential of the photocathode is set with a high precision power supply (Heinzinger PNChp 100000). It is specified to have a 10^{-5} RMS voltage stability of the maximum voltage, i.e. its RMS fluctuations are approximately 1 V. A commercial feedthrough, made of a big ceramic insulation, was initially used to connect the power supply with the photocathode. The feedthrough, however, was found to be very fragile. Small arcs were found to make it locally conducting, evoking consecutive arcs at the feedthrough and the photocathode. A custom feedthrough was therefore designed and assembled, which is found to be more robust and much smaller. Since a commercialization is considered, no further details will be given here.

2.1.3. Electron pulse propagation

The repelling action of Coulomb forces between electrons within an electron pulse makes the description of their propagation and therefore the prediction of their pulse duration at the sample position a non-trivial problem. Whereas the pulse duration is the limiting factor for time resolution of electron diffraction experiments today, its experimental determination is challenging as well. Pulse durations have been measured by scattering of electrons off a standing wave, created by a short laser pulse [Heb06],

and variations of this method have been proposed [Kir13a]. In this section, simulations of the propagation of short electron pulses are presented. From these, pulse duration at the sample position are calculated.

Simulation details

The simulations were done with a fully relativistic multi-body particle tracing code (general particle tracer (GPT), Pulsar Physics). The software simulates the propagation of a pulse containing N electrons by calculating the propagation of a pulse containing N_m macroparticles. These have a mass of $N \cdot m_e/N_m$ and charge $N \cdot q_e/N_m$, where m_e and q_e are the mass and charge of an electron. Full particle-to-particle interactions are calculated for each time-step of the simulations and a Runge-Kutta solver is used to calculate the propagation of the macroparticles. It is found that 1000 macroparticles are sufficient for converged simulations of electron bunches containing up to 10^4 electrons in the geometry presented in the following.

The macroparticles are created at different simulation times around zero with a Gaussian temporal distribution of FWHM τ_l, representing the laser pulse duration. They are accelerated in a static electric field of 12.5 MV/m, created by two flat surfaces. The particle density of the electron bunch is assumed to follow a Gaussian distribution in both transverse directions, with an initial spatial width at creation of d_l. Each particle is assigned an energy and momentum at their creation in the simulation. The initial momenta's directions are distributed uniformly on a half-sphere in forward propagation-direction. The energies of the macroparticles follow a Gaussian distribution and the energy width is dependent on the laser's parameters. Assuming that the laser pulse is Fourier-limited, its energy bandwidth is calculated from the pulse duration τ_l by $\Delta E_l = 0.44 \cdot h/\tau_l$. The electron energy width is calculated as the laser's bandwidth, convoluted with a Gaussian distribution of 100 meV width to obtain $\Delta E_{\text{initial}} = ((0.44 \cdot h/\tau_l)^2 + 0.1^2)^{1/2}$ eV to account for local inhomogeneities of the presumably polycrystalline photocathode. The distribution spans from zero to 3 sigma with the center being at one sigma.

Electron pulse durations were calculated by taking the standard deviation of the simulated electron positions within the pulse at a fixed time-point of the solver and division by their average velocity. The sample position was assumed to be at a distance of 10 mm from the cathode, which corresponds to the closest possible measurement position of the apparatus. Pulse durations on the sample position were therefore calculated for the time-points of the solver, where the average position was closest to 10 mm. Since

the distributions were close to Gaussian, all pulse durations in the following are given in FWHM, calculated from the standard deviations.

Simulation results

The propagation of electron pulses containing a single electron has been studied analytically [Aid10]. It has been found that their pulse duration increases with emission bandwidth $\Delta E_{\text{initial}}$ and with increasing laser pulse length. Since both are ultimately connected by the uncertainty relation, the shortest electron bunch is achieved for a specific time-bandwidth product.The dependence of electron pulse duration on electron number and laser pulse length, calculated with the GPT code, is shown in figure 2.7. The second x-axis on the upper edge has been added to show the effect of photoemission in a two-photon process (two photon photoemission, 2PPE) as used in the experiments presented in this work. Due to the second-order nonlinearity of the photoemission process, the effective pulse length is lowered by a factor of $\sqrt{2}$, whereas the bandwidth is increased by the same factor, what results only in a shift of the abscissa. The effective laser spot size d_l changes for the same reasons and was chosen to be 50 µm (1PPE), corresponding to 71 µm (2PPE), close to typical experimental values. The considered range of one to 10^4 electrons corresponds to the experimentally accessible range.

Simulations, for which space charge effects have been switched off (red curve) qualitatively reproduce the expected shape of the analytical expression for single electron pulses [Aid10]. Pulses containing more than one electron and including space charge follow similar curves (blue lines). However, they are shifted towards longer pulse durations with increasing electron numbers due to the increasing impact of Coulomb-forces within the pulse. For the given parameters, the simulation predicts an overall space-charge induced broadening of the pulselength of 10% for a pulse containing 10^3 electrons and 100% for 10^4 electrons with respect to single-electron pulses.

The effects of space charge are further specified by investigating the dependence of initial electron density on the pulse duration at the sample position. Figure 2.7 b) and c) show the dependence of electron pulse duration on laser spot size, defining the electron pulse diameter, and electron number per pulse. In both cases, the optimal laser pulse length $\tau_{l,1PPE} = 25\,\text{fs}$ has been used for the simulation. The figures show an increase of pulse duration with higher initial electron density, i.e. a small bunch diameter and a higher electron number.

This shows that, whereas a high number of electrons per pulse immediately translates to better statistics in the diffraction images, it also leads to longer pulses. Increasing the bunch diameter is advantageous for having short pulse durations, since it partly com-

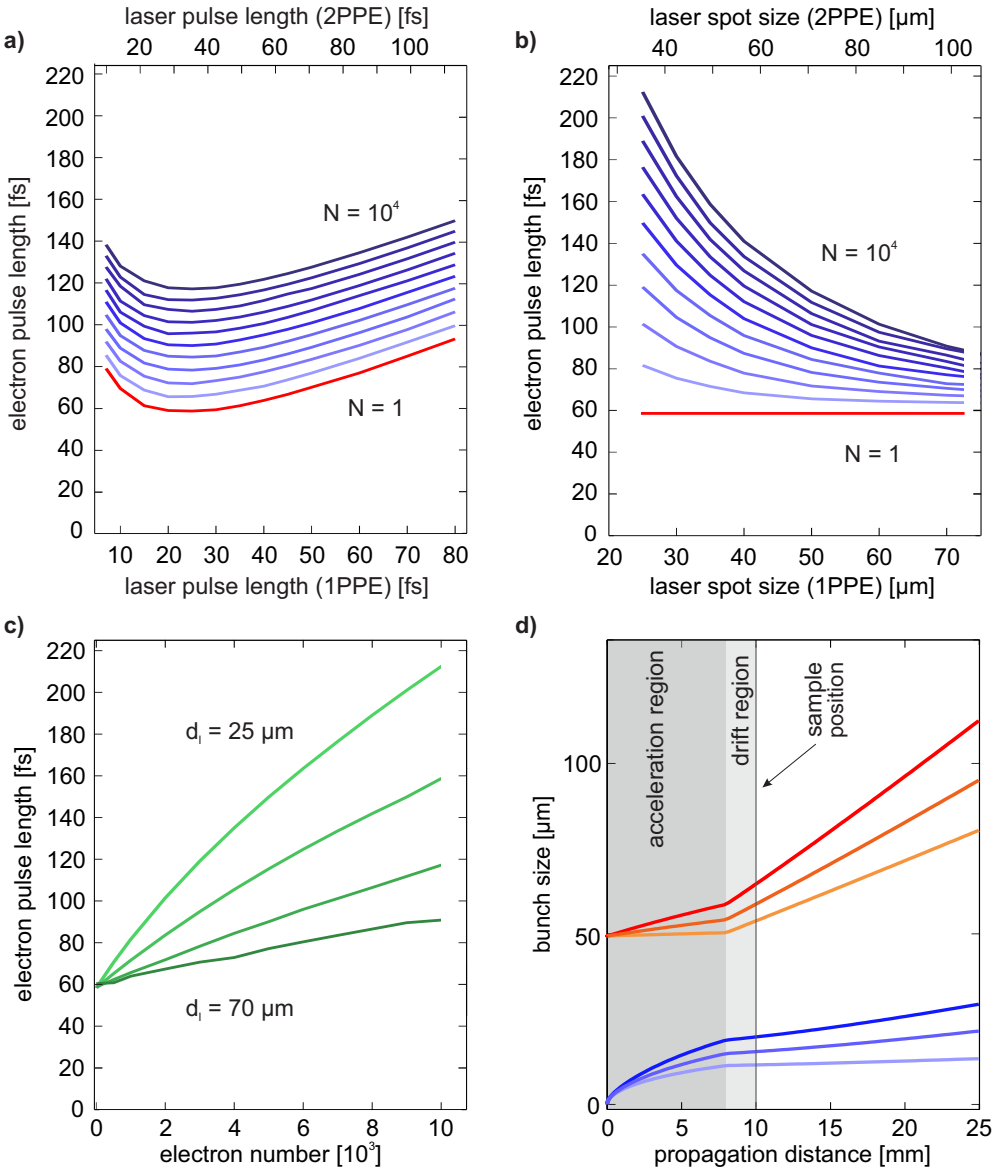

Figure 2.7.: Results of the simulations of electron propagation with the GPT code. **a)** Electron pulse duration as a function of laser pulse duration and number of electrons per pulse (red: one electron, blue: 10^3 to 10^4 electrons in steps of 10^3, light to dark). **b)** Electron pulse duration as a function of laser spotsize and different numbers of electrons per pulse (colors as in a)) **c)** Electron pulse duration on the sample as function of electron number for laser spotsizes of $d_l = 25$ (light), 35, 50 and 70 µm (dark). **d)** transversal (red) and longitudinal (blue) FWHM bunch sizes for 10^3, $5 \cdot 10^3$ and 10^4 electrons (light to dark).

pensates the spread caused by the high electron number. However, there are practical limits for the electron bunch diameter. In particular, sample sizes of thin freestanding films are limited, as larger samples are increasingly fragile and heat removal becomes difficult. In addition, the temporal mismatch of non-collinear pump and probe pulses increase with beam sizes, as discussed previously and shown in figure 2.3.

In recent years, several models, analytically describing electron pulse propagation, have been proposed [Siw02, Qia03]. They use a mean-field approach to calculate the temporal broadening Δt_{el} caused by space charge effects. The models assume a cylindrically shaped electron bunch with diameter r_t, which stays constant during propagation. With d being the cathode-anode distance, V_0 the potential difference between them and L the propagation distance in real space, the total temporal broadening due to space charge has been given to be [Qia03]

$$\Delta t_{\mathrm{el}} = \frac{e^{1/2} m^{1/2}}{\sqrt{2}\pi\epsilon_0} \frac{N}{V_0^{3/2} r_t^2} \left(\frac{L^2}{4} + d^2 \right) \tag{2.1}$$

A qualitative agreement of the GPT simulations with the predictions of these models, namely a linear dependence on electron number and a $1/r_t^2$ dependence can be found for small electron numbers per pulse, whereas for higher electron numbers per pulse they deviate. A quantitative comparison is difficult even in the case of low electron numbers, because of the geometrical assumption of a cylindrical bunch shape in the analytical models.

An assumption of the models is that transversal distances between electrons are much bigger than distances in longitudinal (propagation) direction ($r_b \gg l$). Figure 2.7 d) shows longitudinal and transversal bunch diameters during the propagation through the setup. Both change dynamically, opposed to the assumptions of the models. Especially, passage of the electron bunch through the anode changes the divergence of the bunch, because of the hole acting as an Einzel-lens. For higher electron numbers, longitudinal and transversal bunch sizes become comparable in magnitude in conflict with the assumption $r_b \gg l$ of these models. This illustrates the importance of using multi-body simulations for the accurate calculation of the propagation of femtosecond electron bunches. The simulations shown here are used as a reference for the alignment of the experiments presented in this thesis. They can also serve as a guideline in the design of future compact femtosecond electron diffraction setups.

2.1.4. Electron diffraction in the single-shot regime

Studies of the lattice dynamics of irreversible processes require special adaptations of the diffraction experiment described in 2.1. The time resolved electron diffraction experiments in chapter 5.3 have been carried out with single pump and probe pulses per recorded diffraction image. After each pump-probe cycle, the samples were moved to a fresh spot.

In the single-shot experiments, large area Si-grids were used to support the thin films (see section 2.1.1). Using large areas of samples in a single measurement requires that the temporal and spatial overlap do not depend on the sample position, what means that the sample surface needs to be flat and parallel to the movement of the stage shifting it. The flatness was ensured by the design of the grids themselves. The alignment of the grids for a parallel motion to the stage's direction was done by repeated measurements of the lattice heating dynamics under reversible conditions in three different corners of the sample. The zero-time of the measurements was fitted and compared. The picomotors of the sample mount were then used to tilt the sample such, that the corner, where the heating dynamics started later in the experiment, was shifted away from the electron gun (towards the pump). After alignment, the extracted onset of the heating dynamics was within 250 fs at all measurement positions.

To select single laser pulses from the 1 kHz pulse train delivered by the laser system, a combination of a chopper and a fast shutter with 3 ms opening time (Uniblitz LS6) were used. The chopper was set to reduce the repetition rate to 250 Hz, with two consecutive pulses coming through and two being blocked. The shutter was then used to select one of the two pulses. The synchronization of the electron camera, shutters to select or block the pump pulses and the pulse picking was done with a LabView program and a pulse selecting device built by the electronic workshop of the FHI. The master trigger came from the software which opens or closes the pump shutter and then gives out a TTL-pulse via an analog-digital (A/D) converter. This pulse is used to trigger the camera, which is set to a 30 ms exposure time. At the same time, it is fed to the pulse selector, where it acts as a 'gate'. The second input to the device is the trigger from the laser amplifier, which is electronically divided by 4 to 250 Hz ('trigger'). The pulse selector is activated by the gating pulse and gives out a single TTL pulse which is synchronized to the first trigger pulse after activation by the gate. A schematic representation of the trigger and gating sequence is shown in figure 2.8 a).

The measurements were done by taking a series of three diffraction images at each sample position: a static image (with the pump pulse blocked by a shutter), the pump-

probe image, and a second static image. The first image was used to check the initial sample quality. If the diffracted intensity of the image was below an empirically define threshold, this sample position was excluded from averaging. The third image was taken to check the final state (at quasi-infinite time delay) of the sample. A typical diffraction image is shown in figure 2.8 b). Single electron events can be identified in the image.

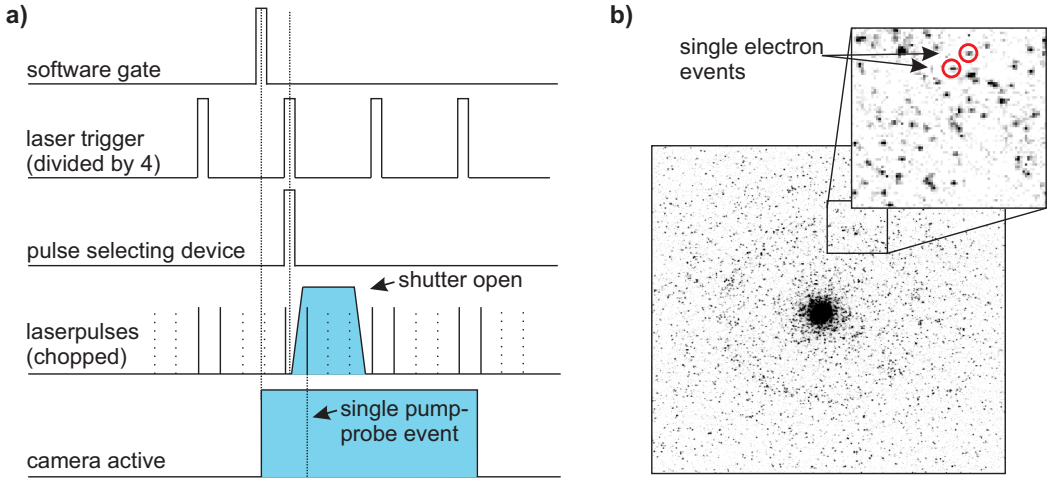

Figure 2.8.: **a)** Trigger sequence for generating single electron diffraction images. A software trigger (gate) starts camera acquisition. It is also fed to a pulse selector, the output of which is a TTL pulse, synchronized to the next laser trigger pulse after activation by the gate. The fast shutter opens and closes with this signal. Since the laser is chopped, its 3 ms transition time is short enough to select a single laser pulse. **b)** Diffraction image from a single laser pulse. Single electron events can be detected with the camera (see inlet).

2.2. Femtosecond optical spectroscopy

The propagation of light is fully determined by Maxwell's equations, which can be found in almost any textbook on electrodynamics and optics (see e.g. [Bor01]). In a medium, light interacts with the charges of the material and therefore induces a time- and position dependent polarization $P(\vec{x}, t)$. At the same time, this polarization acts as a source of radiation. The quantity connecting the amplitude and phase of the external field $E(\vec{x}, t)$ with the polarization of the medium is the susceptibility χ. The susceptibility incorporates all fundamental interactions of light with the solid, which in the visible spectral region are manifold, such as induced electronic intra- and interband transitions, excitation of lattice vibrations, formation of excitons, polarons,

etc. It therefore is a function of frequency ω, wavevector $\vec{k}$ and amplitude of the electromagnetic field. The measurement of frequency-, wavevector, linear- and non-linear dependence of the susceptibility therefore contains a wealth of information on the fundamental interactions present in the solid, but entanglement of all the processes is mostly not trivial.

Using ultrashort laser pulses in an all optical pump-probe type experiment allows to follow changes in the optical properties of a sample after photoexcitation. These changes might then be attributed to a fundamental process in the sample, such as heating of electronic and lattice subsystems [Bro90], the launch of coherent phonons [De 85, Zei92], or induced (structural) phase transitions [Wal12] etc. The following section will introduce the methods used in this work and will discuss how measured quantities can be connected to fundamental physical properties.

2.2.1. Reflectivity and transmissivity of thin film multilayer structures

Boundaries between media of different index of refraction give rise to reflection (and refraction) of light. The amplitude of reflected and transmitted light depends on the dielectric constants of the two media, but also on the incident angle, the sample geometry and the polarization direction of the light. For a single interface, Fresnel's equations connect reflected and transmitted intensities with these parameters. However, the situation gets more complicated if one considers the reflection of thin films with thicknesses smaller than the coherence length of the light. Reflected intensities of the front and the back surface can interfere constructively or destructively and thus change the observed reflectivity and transmission. A convenient way to treat multiple reflexions is given by the transfer matrix formalism, which can be used to treat reflections from arbitrary many thin layers. For simplicity, only the case of normal incidence onto a multilayer sample is considered here. For a derivation of the equations, see e.g. [Bor01].

The characteristic matrix of a thin film with complex refractive index $n = \sqrt{\epsilon_1 + i\epsilon_2}$ and thickness δ, which is surrounded by two semi-infinite media is given by:

$$M = \begin{pmatrix} m_{11} & m_{12} \\ m_{21} & m_{22} \end{pmatrix} = \begin{pmatrix} \cos(k\delta) & \frac{1}{k}\sin(k\delta) \\ -k\sin(k\delta) & \cos(k\delta) \end{pmatrix} \tag{2.2}$$

where k denotes the wave vector $k = 2\pi n/\lambda$. The coefficients of reflection and transmission are calculated from the matrix elements of the characteristic matrix. If the wave

vectors in the first and the last medium are indicated by k_1 and k_l, the coefficients can be expressed as:

$$r = \frac{(m_{21} + k_1 k_l m_{12}) + i(k_1 m_{22} - k_l m_{11})}{(-m_{21} + k_1 k_l m_{12}) + i(k_1 m_{22} + k_l m_{11})} \tag{2.3}$$

$$t = 2ik_1 \exp -ik_l \delta \frac{m_{11} m_{22} - m_{12} m_{21}}{(-m_{21} + k_1 k_l m_{12}) + i(k_1 m_{22} + k_l m_{11})} \tag{2.4}$$

Stacks of thin layers can be treated by simple multiplication of their characteristic matrices M_i.

$$M = M_N \cdot ... \cdot M_2 \cdot M_1. \tag{2.5}$$

From the resulting matrix M, the reflected and transmitted amplitudes are calculated in the same way as indicated above for the characteristic matrix of a single film.

2.2.2. Measurement of transient optical properties

To measure photoinduced changes in the optical properties on the ultrafast timescale, all optical pump-probe schemes have been applied in this work. The probe-pulses are split off the pump-pulse with a beamsplitter. In the most simple case, neither of the pulses is modified in spectral or temporal shape and the intensity of the probe pulse is kept well below the one of the pump-pulse to not induce any changes to the sample with it. Whereas pump-induced changes can be measured with many different optical techniques, measuring different physical quantities (e.g. rotation of the polarization, spectral absorption, ...), the most easily accessible quantities are the reflected R or transmitted T intensities of the probe pulses. Both can directly be measured with a photodetector, such as a photodiode or a bolometer, which is placed in the beampath. By varying the delay Δt between the pump- and the probe pulse with a delay stage, their evolution in time, $R(t)$ and $T(t)$, can be recorded.

Since pump-induced changes are typically small, they are commonly amplified with Lock-In amplifiers. To do so, the pump-pulses are periodically blocked with a rotating chopper-wheel, such that the pump-induced signal is periodically switched off and on. The Lock-In amplifiers then apply a narrow-band frequency filter at the frequency of the chopper. This attenuates the noise and amplifies the pump-induced signal, enabling one to measure signals below the noise level of the detector (e.g. the photodiode). The smaller the bandwidth of the frequency-filter, the longer (more periods of on-and off) the Lock-In amplifier needs to integrate to measure a meaningful signal.

As shown in the previous section, absolute numbers of the reflectivity and transmission depend not only on the material's fundamental properties, but also on the geometry of the sample and the measurement. In an extreme case, an increase in transmission could

coincide with an increase in absorption. For a quantitative discussion of pump-induced changes, it is therefore beneficial (and sometimes necessary) to investigate changes in the dielectric function rather than changes in transmitted or reflected intensities only.

Even though the dielectric function is not an observable quantity per se, its value and evolution in time can be retrieved when sufficient independent information is measured. This can be done in various ways, e.g. by an ellipsometry-type of experiment (difference in reflectivity of s- and p-polarized light) or by the reflectivity at different angles of incidence. A simple option, if measurements are done on thin films with known thickness, is the simultaneous measurement of the reflected and transmitted intensities $R(t)$ and $T(t)$. In this case, the equations of the matrix formalism can be numerically inverted to obtain the refractive index or, equivalently, the dielectric function at the frequency of the probe wavelength.

2.2.3. Frequency domain single-shot spectroscopy

The standard technique to measure laser induced changes in reflected or transmitted intensities of a material is based on Lock-In amplification, as described in 2.2.2. This technique, however, requires that changes induced by the pump pulses are reversible, i.e. that the reflectivity (transmission) relaxes back to the initial value before the next pump-pulse hits the sample. For measurements in which a single pump laser pulse is sufficient to induce an irreversible change to the sample, this is not fulfilled and alternative methods are needed. This chapter introduces a technique that encodes the transient optical properties in the spectrum of a single laser pulse, which has been called "frequency domain single-shot spectroscopy" (FDSS) [Bed92, Shk04]. This non-standard technique was used to measure changes in the dielectric function of the phase change material $Ge_2Sb_2Te_5$, described in chapter 5. Other methods, capable of measuring dynamics in of the optical properties in a single shot have been described in [Wak00, Shi14], but will not be further discussed here.

A sketch of the FDSS technique is shown in figure 2.9. A compressed laser pulse is split into a pump- and a probe pulse. The probe pulse passes through a prism made of a highly dispersive glass (SCHOTT SF10) with a total optical path length of 180 mm, thereby stretching it to about 10 ps pulse duration. With the material's dispersion being linear in the spectral region of the laser, the probe pulses exhibit a linear time-frequency correlation (linear chirp). The pump and probe beam's relative timing is fixed such that roughly 1/3 of the probe pulse has passed through the sample at the time the pump pulse arrives. As a result, each frequency of the probe pulse arrives at

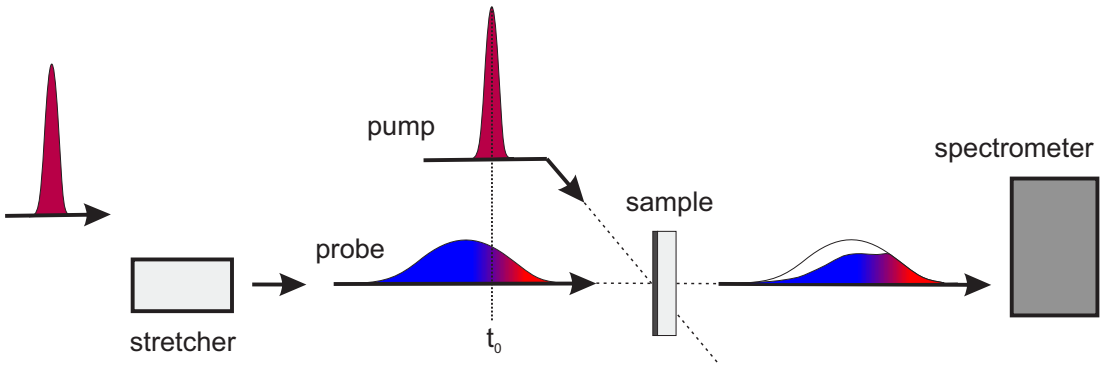

Figure 2.9.: Schematic drawing of the spectral encoding technique. The probe pulse is given a linear chirp, such that different frequencies have different relative delays to the pump pulse. A spectrometer is used to measure spectral intensities and therefore a pump-probe trace in a single shot.

the sample with a different relative delay with respect to the pump pulse, parts of it having positive, other parts negative delay.

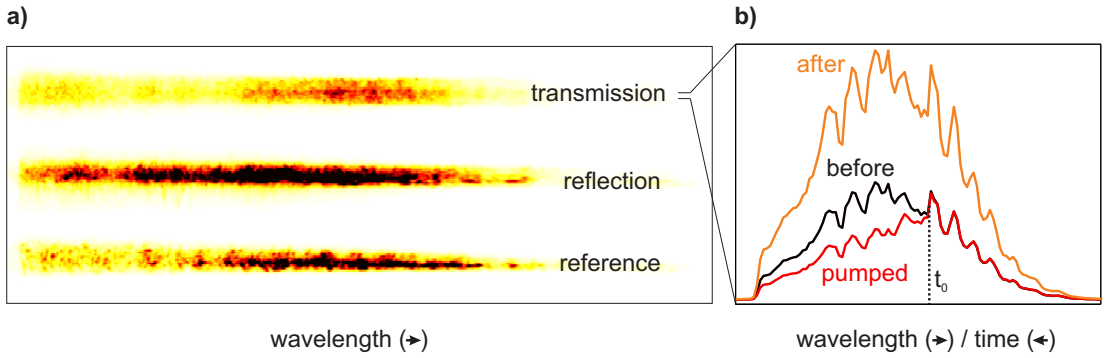

Figure 2.10.: **a)** Raw spectrometer image with three spectra recorded in parallel (reflection, transmission, reference). **b)** Vertically integrated transmission spectra of three consecutive spectra taken at the same sample position. Without pump pulse ('before'), with pump pulse ('pumped') and again without pump pulse ('after').

Three spectra are measured simultaneously with an imaging spectrometer to be able to later calculate the dielectric function from the data. Therefore, three fibers are connected with a vertical offset to the spectrometer's entrance slit. Two fibers collect the intensity of the transmitted and reflected probe pulses, respectively, and the third fiber collects a split-off part of the pulse before it reaches the sample. The latter acts as a reference for correct changes of the laser's spectrum. The three spectra have a vertical offset in the spectrometer and are recorded with a CCD camera. A typical image of

the spectrometers camera is presented in figure 2.10 a), showing three simultaneously measured, vertically separated spectra.

Three consecutive images are taken at each sample position. The first spectrum ('before') is taken without a pump pulse on the sample, the second ('pumped') is taken with a pump and probe pulse on the sample and the third ('after') is taken without pump pulse to investigate if permanent changes were induced. Figure 2.10 b) shows a series of three consecutively taken spectra of the transmitted intensity of the pulses. The temporal overlap of pump and probe in the pumped spectrum is visible in the raw data and is indicated in the plot. The relative changes in transmission $\Delta T/T$ and reflection $\Delta R/R$ are obtained by dividing the intensity of the spectra taken with the pump pulse by the spectra before $\Delta X/X = I_{X,pumped}/I_{X,before}$.

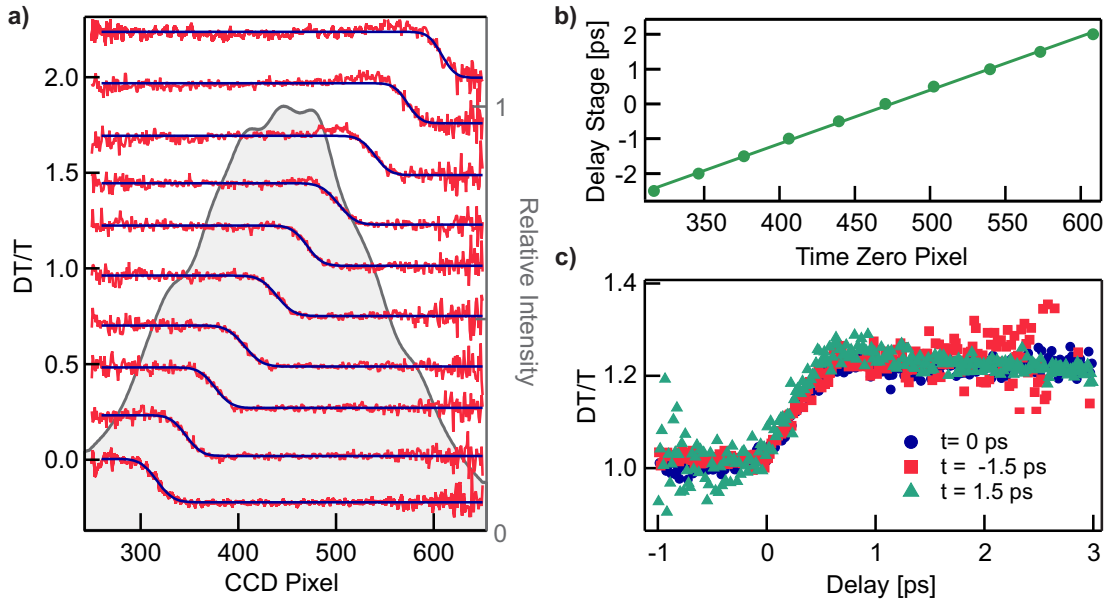

Figure 2.11.: Calibration of the time axis for frequency-time conversion. **a)** Pump-induced optical dynamics for different positions of the delay stage. The dynamics are fitted with a step function. The gray area shows the spectral intensity of the laser pulses, explaining the higher noise on the sides of the traces. **b)** The zero position of the fit is plotted against nominal pump-probe delay. The linear dependence shows the linear chirp of the probe pulses. **c)** After shifting the time traces from a) by the appropriate time delay, the exact same dynamics are observed. This demonstrates that the measured dynamics are independent of wavelength within the frequency window used.

Assuming that the pump-induced changes are independent within the window of probe frequencies, the temporal changes can be assigned by simply replacing the wavelength-axis with the pump-probe delay. The frequency-to-time calibration of the measured

spectra is achieved by using a motorized delay stage to change the relative arrival time between pump and probe beams. The relative changes in reflected intensity of a photoexcited film of $Ge_2Sb_2Te_5$ is shown in figure 2.11. The increased noise on the sides of the traces is caused by the reduced intensity in the wings of the spectrum (the spectrum is shown as a shaded area). The time zero position can be found by fitting an error function to the signal at each delay (solid lines), which is then used as a marker for the calibration. Figure 2.11 b) shows the extracted time zero positions, plotted against the delay calculated from the positions of the delay stage. It shows that the chirp of the pulse is linear with a slope of the calibration line of 15.4 fs/pixel in the shown measurement. Fig.2.11 c) shows three pump-probe traces from figure 2.11 a), shifted by their relative delay. It can be seen that the traces lie well on top of each other, which demonstrates that the photoinduced changes of the optical properties of $Ge_2Sb_2Te_5$ are independent of the probe wavelength in the frequency window used.

Due to the increased noise on the extremes of the traces, the spectral range used in the analysis therefore needed to be confined and only 5 ps of the dynamics were evaluated. The temporal overlap was chosen such that about two thirds of the spectrum were used to map the dynamics after time zero.

The theoretical temporal resolution of pump-probe experiments employing chirped probe-pulses has been shown to be similar to the resolution of an experiment using transform limited pulses [Pol10]. A perfectly built setup would thus have a temporal resolution of around 40 fs, considering the spectrum of the Ti:Sapphire amplified laser used. Due to imperfect alignment of the setup, the time-resolution of the experiments presented in chapter 5 was on the order of few hundreds of femtoseconds.

3. Lattice vibrations

A crystal lattice is a mathematical construction describing the periodic arrangement of atoms in crystals (note that crystals without translational symmetry exist [She84, Int92], but are beyond the scope of this work). The repeating atomic motive is defined by the unit cell, which is anchored at each lattice site. Together, the lattice and the unit cell describe the equilibrium position of each atom in a perfect crystal. Microscopically, the positions correspond to the minima of the potential energy surface, which is set by the complex interactions of all atomic cores and electrons.

The periodicity of crystal structures and the interactions between neighboring atoms leads to the description of atomic motion in solids as collective vibrations. These collective vibrations constitute a basis for describing atomic motion in solids and, since they exhibit particle properties, are called phonons. The derivation of basic properties of phonons, such as the dispersion relations for simple crystal structures, is found in many textbooks on solid state physics [Ash76, Kit05]. This chapter is intended to give a brief overview of real-space motion of atoms, their excitation mechanisms and the influence of phonon distributions on diffraction and optical experiments, which will be used in this work.

3.1. Real space motion of atoms and phonon distributions

In the treatment of lattice vibrations, it is commonly assumed that the forces on an atom are a linear function of their displacement. This is similar to the statement that each atom feels a harmonic potential, for which it is called harmonic approximation. In the harmonic approximation, a phonon mode of frequency ω and wavevector k leads to a motion of all atoms of the shape

$$u(x,t) = u_0 \cdot \cos(kx) \cdot \cos(\omega t). \tag{3.1}$$

The amplitude u_0 of this motion can be calculated and related to the occupancy of the phonon mode via the basic relation that the time average of kinetic energy and potential energy are equal in a harmonic oscillator. The time average of the square of each atoms displacement (also called mean square displacement, MSD) is $\langle u^2 \rangle = 1/2 \cdot u_0^2$, because $\langle \cos \omega t^2 \rangle = 1/2$. For $n \gg 1$ phonons of frequency ω it is given by

$$\langle u^2 \rangle = \frac{2(n + \frac{1}{2})\hbar}{\rho V \omega} \approx \frac{2n\hbar}{\rho V \omega}, \tag{3.2}$$

where ρ is the materials density, V its volume and $\hbar$ is Planck's constant h divided by 2π. A comparison of two phonon modes of same occupancy but different frequency shows that their real-space amplitude, and therefore the mean square displacement, are different by

$$\frac{\langle u_1^2 \rangle}{\langle u_2^2 \rangle} = \frac{\omega_2^2}{\omega_1^2}. \tag{3.3}$$

The nature of phonons as being collective excitations, or quasi-particles, relates to the fact that they are bosons with a chemical potential μ equal to zero. In a crystal, which is in thermal equilibrium, the mean number of excited phonon modes therefore follows Bose-Einstein statistics. The time-averaged occupancy of a mode of energy $\hbar\omega$ is therefore given by

$$\langle n \rangle (\hbar\omega) = \frac{1}{e^{\frac{\hbar\omega}{k_B T}} - 1}. \tag{3.4}$$

To calculate the mean square displacement of atoms in a thermal state, one needs to sum over the contributions of all phonon modes of the solid. The phonon modes are described by the phonon density of states $g(\omega)$ (see e.g. [Kit05]), and their occupancy is given by the BE-distribution. In this case, the MSD is given by [Sea91]

$$\langle u^2 \rangle = \frac{3\hbar}{2M} \int_0^\infty \coth\left(\frac{\hbar\omega}{2k_B T}\right) \frac{g_n(\omega)}{\omega} \, d\omega, \tag{3.5}$$

where M is the atomic mass, T is the temperature of the system and $g_n(\omega)$ is the normalized phonon density of states, i.e. the density of states for which $\int g(\omega) = 1$.

In this thesis, laser pulses are employed to create non-equilibrium situations between electrons and phonons. The excited electrons then equilibrate with the phonons by transferring energy to them. In such a situation, the phonons must not necessarily be in a thermal state. This situation is specifically studied in chapters 4.1 & 4.2. The implications of such states is discussed there.

3.2. Phonons in diffraction experiments

The theory of diffraction, as developed by W. Bragg and M. von Laue, assumes the atoms in a crystal to be rigid and the lattice to be perfect. In a real system, however, atoms vibrate around their equilibrium position. These vibrations locally distort the crystal from its perfect periodicity. In diffraction experiments, particles are thus scattered from an imperfect lattice, which leads to a decrease in scattered intensity in the Bragg-peaks and an increase of incoherently scattered intensity in between them. The influence of the vibrations on the scattered intensity I can be quantified via the mean square displacement $\langle u^2 \rangle$ of the atoms around their equilibrium position. The intensity of a Bragg peak with scattering vector $s = 2 \sin \Theta / \lambda$ is given by:

$$I = I_0 \cdot \exp\left(-4\pi^2 \langle (\boldsymbol{u} \cdot \boldsymbol{s})^2 \rangle\right), \tag{3.6}$$

where I_0 is the intensity of a Bragg-reflection from a perfect crystal and bold symbols indicate the vector character of the displacement and the scattering vector. In the case that the vibrations are isotropic, $\langle (\boldsymbol{u} \cdot \boldsymbol{s})^2 \rangle = \frac{1}{3} \langle u^2 \rangle s^2$ and the measured intensity becomes

$$I = I_0 \cdot \exp\left(-\frac{4}{3}\pi^2 \langle u^2 \rangle s^2\right). \tag{3.7}$$

Materials with a non-cubic unit cell, such as Sb, which is investigated in chapter 4.2, can show anisotropic properties, like thermal expansion [Whi72]. Also the mean square displacement can contain anisotropic contributions, i.e. it can be different between specific crystallographic directions. For Sb and the somewhat similar elements As and Bi, the anisotropic contributions to the MSD have been investigated in terms of contributions in the directions parallel and perpendicular to the c-axis [Sos75, Fis77]. Except for Bismuth, however, no significant anisotropy has been found. The data on antimony, presented in chapter 4.2 can therefore be analyzed as described here.

Thermal phonon distributions, as defined in the last section, are characterized by the BE-distribution of the phonon modes. Equation 3.5 connects the mean square displacement to this distribution, and therefore to a temperature. The MSD in equation 3.7 is therefore often replaced by the temperature dependent Debye-Waller B-factor $B(T)$ [Pen04]

$$\frac{4}{3}\pi^2 \langle u^2 \rangle = B(T) \tag{3.8}$$

Even though equations (3.5) and 3.8 provide an analytical expression for the Debye-Waller B-factor, it is typically more convenient to use an empirical expression for $B(T)$.

Typically, a polynomial of degree 4 is used, and tabulated prefactors of standard elements and compounds can e.g. be found in [Pen04].

With the equations above, it is possible to calculate a lattice temperature from a diffraction experiment if the intensities I_0 are known. Alternatively, the lattice temperature T can be calculated from the ratio of intensities $I_{\mathrm{rel}} = I(T)/I_{\mathrm{ref}}$ of the intensities $I(T)$ of the Bragg-peaks with respect to the intensities I_{ref} at a reference temperature T_{ref}. By combining and rewriting equations (3.7) & (3.8), one obtains

$$-\frac{\ln(I_{\mathrm{rel},s})}{s^2} = B(T) - B(T_{\mathrm{ref}}). \tag{3.9}$$

In general, this equation is not solvable analytically, but can be solved numerically to obtain the temperature of the lattice from the relative intensities of the measured diffraction peaks. The left side of equation 3.9 is used in the data-analysis throughout this work, since it also allows to compare the evolution of different Bragg-peaks with scattering vector s. The validity of this equation in a time-resolved experiment is not necessarily given, as phonons can potentially be in non-thermal states. The validity of the equation will be discussed in all chapters with respect to the respective investigated materials.

3.3. Coherent phonons

Coherence is a property of waves; two parts of a wave are defined to be temporally (spatially) coherent if they have a fixed phase-relationship in time (space). Equally, phonons of a certain mode are said to be coherent, if they are excited with a defined phase relationship, such that a macroscopic, collective oscillation of atoms can be observed. Phonons of a certain mode, which are excited by a stimulus in a time-window shorter than their oscillation period, exhibit this relationship and oscillate in phase. This has already been observed in early femtosecond optical pump-probe measurements performed in the 1980's [De 85, Ros86]. Later, such oscillations were not only found in molecular systems, but also in the semimetals Bi and Sb [Che90, Zei92]. Today, the detection of coherent lattice oscillations has even become a spectroscopic tool for investigating changes in the lattice potential [Wal12, Sto14].

Two basic mechanisms of the excitation of coherent phonon modes have been identified [Dek00]. Figure 3.1, which has been taken from [Ish10], illustrates the two mechanisms, called 'impulsive' (Raman) excitation and 'displacive' excitation (DECP, displacive excitation of coherent phonons). In both cases, a time-dependent force $F(t)$ is exerted on the atoms, starting a damped oscillation. The origin of the force in the impulsive

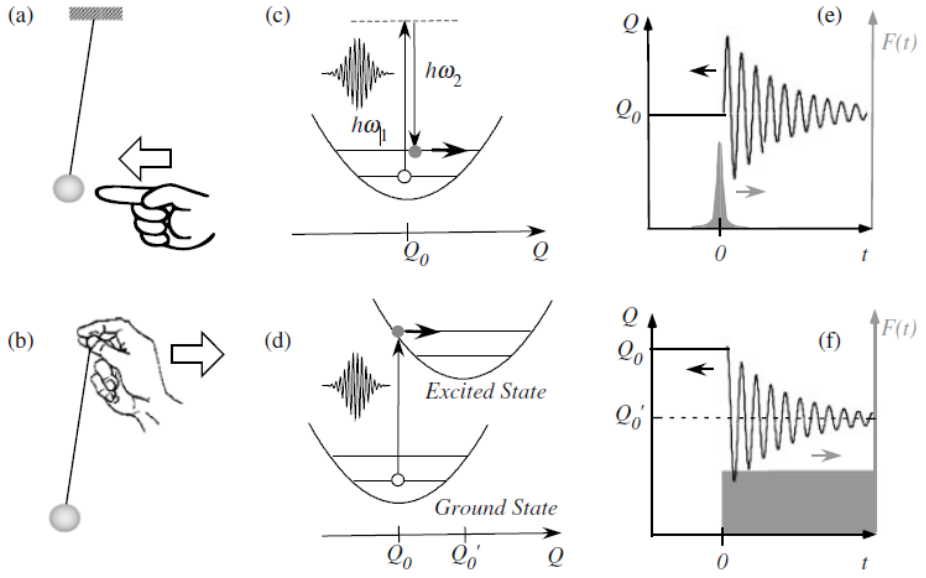

Figure 3.1.: Excitation mechanisms for coherent phonons. **a)**, **c)** & **e)** Impulsive excitation, in which a photon is absorbed into a virtual state and emitted by creation of a phonon (Raman-scattering). The lattice potential stays unchanged. **b)**, **d)**, **f)** Displacive excitation of phonons. The laser pulse is absorbed into a real electronic state, with a shifted equilibrium position of the atomic nuclei. Image taken from [Ish10].

excitation is the Raman-excitation of phonons, as depicted in c). A photon is absorbed by an electron, which is excited into a virtual state. It then re-emits a photon of different frequency together with a phonon. The temporal shape of the excitation is approximated by a Dirac δ function, due to the typically short pulse-duration compared to the phonon oscillation period. The atoms oscillate in the ground state potential and thus have a sine character, i.e. the amplitude is zero at $t = 0$, as seen in c). In the displacive excitation mechanism, the laser is absorbed by the medium and electrons are excited into a real state [Zei92]. This can shift the minimum of the potential energy surface Q_0 to a new value Q_0'. Atoms, which were at Q_0 before photoexcitation, are collectively accelerated towards Q_0' and start an oscillation around this new minimum. Since the oscillation starts in a displaced position it has a cosine character. In a solid, where the excitation can not be described by a simple two-level system, the redistribution of electrons in the excited states can lead to phase shifts compared to the pure cosine character [Bot13]. Figures a) and b) show the mechanical analogs to the two mechanisms: a pendulum is set to oscillation by a kick to the massive bob (impulsive excitation) or by pulling the rod's pivot point to a new position (displacive excitation). It has been pointed out by some that both mechanisms can be described

by the same Raman-formalism by taking the lifetimes of the states into account [Gar96, Ste02, Rif07].

The most common technique to study coherent lattice vibrations is optical pump-probe spectroscopy, which is introduced in chapter 2.2. The detection of oscillations in measurements of the transient reflectivity is possible if the change of the susceptibility χ with respect to the atomic displacement Q is non-zero [Dek00]

$$\Delta R = \frac{\partial R}{\partial n}\Delta n(t) \approx \frac{\partial R}{\partial \chi}\frac{\partial \chi}{\partial Q}Q(t), \tag{3.10}$$

where Q is the atomic displacement coordinate and $\partial\chi/\partial Q$ is the Raman tensor. A quantitative analysis of optical experiments, retrieving the real-space motion of atoms, is possible if the changes of the optical properties with the displacement coordinate are known. This information, however, can by today only be retrieved from high-level theory, like density functional theory calculations [Kat13] and is so far only available for few systems.

Diffraction experiments are sensitive to atomic motion, in the sense that they measure an ensemble average of atomic displacements. Whereas isotropic and incoherent phonons are well described by the mean-square displacement $\langle u^2 \rangle$ acting on the intensity of Bragg-peaks, the coherent motion of atoms leads to atomic displacements in the crystallographic direction of the phonon and thus has different effects on different Bragg-peaks. Measuring the intensity of a Bragg peak of the respective direction, the coherent motion can directly be visualized [ST03, Joh08].

3.4. Phonon dynamics and time-resolution

In time-resolved experiments, the observable dynamics are limited by the pulse durations of pump- and probe pulses, but can be influenced by other factors as well (e.g. by finite angles between pump and probe, see chapter 2.1.1). In an experiment with an instrument response function of τ_{exp}, the measured dynamics are given by the dynamics of the sample, convoluted with a Gaussian function of width τ_{exp}. This becomes important for measurements where the dynamics proceed on the same timescale as the instrument response function. The measurements on aluminium, presented in chapter 4.1 show that previously reported measurements have presumably been limited in time-resolution. In the course of this work, the time-resolution is included in the fits and models, by convoluting in all fits and models with a Gaussian function.

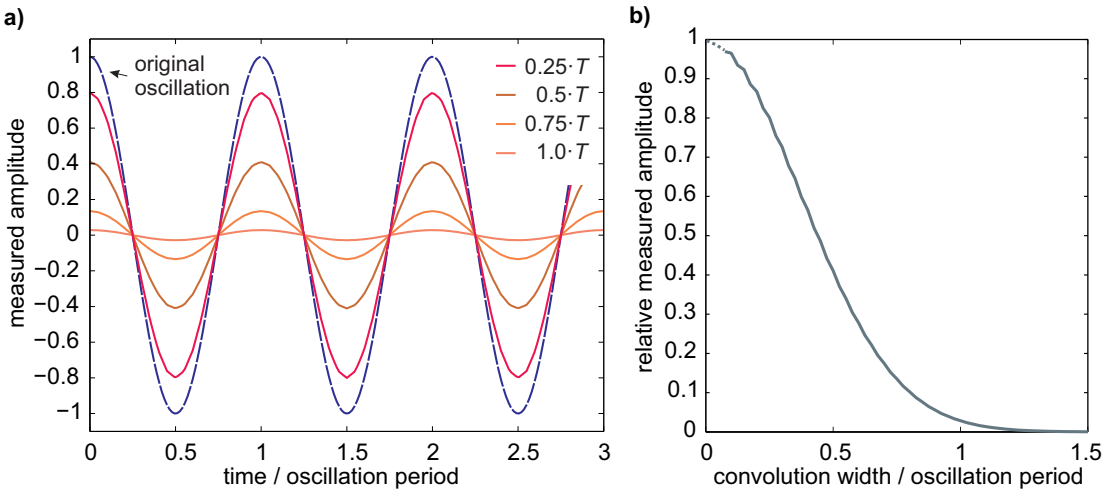

Figure 3.2.: a) Cosine oscillation of period T and amplitude of unity (purple curve), convoluted with a Gaussian function of width $0.25 \cdot T$, $0.5 \cdot T$, $0.75 \cdot T$ and $1 \cdot T$ **b)** Simulated relative oscillation amplitude, which would me measured in an experiment as a function of its convolution width.

In order to be able to observe coherent oscillations in any kind of time-resolved measurements, the time-resolution of the experiment needs to be on the order of the oscillation or better, as otherwise the oscillations are smeared out by the experiment. This can be challenging for some materials, e.g. in diamond, a coherent phonon mode of 40 THz (25 fs oscillation period) is observed [Ish06]. The reduction of the measured amplitude of an oscillation in a time-resolved experiment is illustrated in figure Fig. 3.2. In a), a sinusoidal oscillation of amplitude 1 and period T is shown. The measured signal of this oscillation is simulated by convoluting the oscillation with a Gaussian function of different relative width $x \cdot T$. With increasing relative width of the Gaussian, i.e. with larger time-resolution, the measured amplitude decreases. Once the FWHM approaches the oscillation period, the measured signal almost vanishes. This is quantified in b), where the measured amplitude is plotted against the relative convolution width. The dotted line is an extrapolation to the pulsewidth of zero, for which the exact solution is trivial. For smaller convolution widths the numerical error was getting bigger because of a limited amount of points in the Fourier-transform. The detection limit for a coherent oscillation in a pump-probe experiment therefore does not only depend on its signal-to-noise level, but also on its time-resolution. This relation becomes important in the context of the measurements in chapter 4.2.

4. Electron-lattice interactions in the elements Al and Sb

The interaction between electrons and lattice vibrations is a key parameter to both ground state, as well as out-of-equilibrium properties of solids [Gri81]. Since many fundamental and technologically important processes are strongly influenced by it, e.g. the emergence of classical superconductivity through the formation of Cooper-pairs, the precise study of those interactions is a central topic in solid state physics. However, even in comparably simple systems, the possible interactions are complex due to the high dimensionality of the problem, rendering a universally valid description of electron-phonon couplings virtually impossible.

In this chapter, electron-phonon interactions are investigated in the two elements aluminium and antimony. These two materials illustrate two fundamentally different settings, in which pump-probe experiments can be applied. In both cases, models are presented, which describe the dynamics of the system and fundamental coupling parameters are retrieved.

In aluminium, the effects of photoexcitation on the lattice potential for electronic temperatures up to 6 eV have been shown to be small [Rec06]. The response of the material to intense laser irradiation can therefore be described with electronic and phononic distributions interacting in an equilibrium potential. For excitation densities below these electronic temperatures, a pump-probe measurement could thus be seen as an experimental equivalent to perturbation theory, since only their distributions are changed, whereas the environment is not. A combined theoretical and experimental study of the microscopic pathways of the energy transfer from photoexcited electrons to the lattice is presented, which allows to build a detailed picture of the redistribution of energy in aluminium via electron-phonon interactions. The applicability of the two-temperature model (TTM), which is a widely used model to describe the evolution of non-equilibrium subsystems by assigning temperatures to each of them, is re-evaluated.

Photoexcitation of antimony has, in contrast, very pronounced and direct effects on the potential energy surface, which is a consequence of a Peierls-like instability of the

lattice. Therefore, non-equilibrium effects need to be considered already at very low excitation densities. In particular, the lattice instability facilitates the excitation of coherent phonons, which collectively oscillate in the direction of the distortion [Ish10], in which the changes to the potential predominantly occur. Here, the competition of incoherent and coherent electron-phonon coupling processes, as well as decay mechanisms of coherent phonons, are studied with femtosecond electron diffraction.

The theory presented in section 4.1.1 has been written in collaboration with J. Vorberger, who also conducted the DFT calculations, the results of which are shown here. Parts of this chapter have been published in [Wal16].

4.1. Electron-phonon coupling in non-equilibrium states of aluminium

In the most basic case, in which the excitation of an electron does neither influence the states of all other electrons nor the equilibrium positions of the nuclei, the action of a laser pulse can be understood in terms of distribution functions of electrons and phonons in the equilibrium potential. The evolution of those distributions, however, can be arbitrarily complex and is extremely difficult to access experimentally. The most common approach in the description of non-equilibrium dynamics is thus to assume thermal Fermi-Dirac and Bose-Einstein distributions for electrons and phonons, respectively, and to describe the non-equilibrium quantum statics by a Boltzmann equation. For metals, S. I. Anisimov *et al.* introduced an empirical two-temperature model, utilizing this approximation and describing the energy transfer from excited electrons to the lattice with a single time-constant and later an electron-phonon coupling parameter [Ani67, Ani74]. P. B. Allen refined this approach by developing a microscopic theory in which he derived the electron-phonon coupling parameter from the Eliashberg function $\alpha^2(\omega)F(\omega)$, which is a quantity first deduced from tunneling experiments [Gri81]. It is defined as the product of the phonon density of states $F(\omega)$ and the phonon frequency-dependent electron-phonon coupling $\alpha^2(\omega)$ [All87, Gri81]. While Allen's work provides a link between the Eliashberg theory of conventional metals at low temperatures and the electron-lattice equilibration in laser-excited metals, the underlying assumptions, in particular the one of thermal distributions of electrons and phonons at all times and the independence of α^2 on the electron temperature, are questionable in the latter case of laser-generated non-equilibrium states.

In figure 4.1, DFT calculations (details are given in [Wal16]) of the Eliashberg function and the phonon DOS of aluminium are shown. While in a thermal state the population

of low-frequency phonons is higher than of high-frequency phonons (see the lines of Bose-statistics at three different temperatures), the frequency dependence of the coupling strength of electrons to phonons is the opposite. This suggests that a sudden injection of energy into the electrons, e.g. by photoexcitation with a short laser pulse, transiently generates a non-thermal phonon distribution.

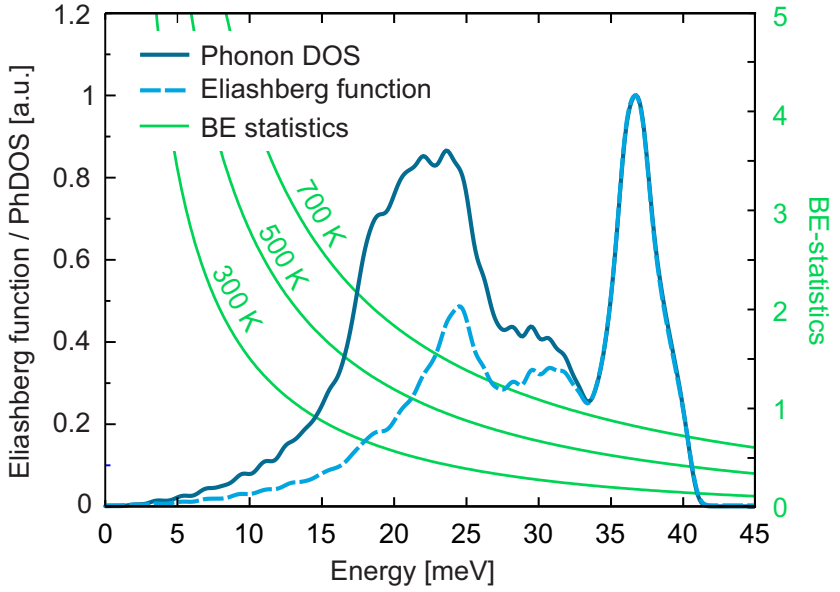

Figure 4.1.: Normalized phonon density of states and Eliashberg function of aluminium, calculated with DFT [Wal16]. The green lines represent the population probability, given by Bose-Einstein statistics, in a thermal state at various temperatures. The Eliashberg function shows an overproportionately strong contribution at higher phonon energies, suggesting that a sudden electronic excitation might lead to a transient non-thermal phonon distribution.

This section is organized as follows: the theoretical approach is described in section 4.1.1. The experimental approach is introduced in section 4.1.2 and electron diffraction experiments are presented in 4.1.3. In section 4.1.4, a two-temperature model is applied to fit the experimentally observed dynamics and to extract an electron-phonon coupling constant. In section 4.1.5, a new model is introduced, including the possibility of non-thermal phonon distributions in the equations modeling the time-evolution of the material. The predictions of this model are compared to the experimentally observed atomic mean squared displacements (MSD). In sections 4.1.6 and 4.1.7 the differences and implications of the non-thermal lattice model are discussed.

4.1.1. Microscopic description of non-equilibrium energy transfer between electrons and phonons

The temporal evolution of a system of electrons and phonons including electron-phonon coupling can be studied theoretically by means of a set of Bloch-Peierls-Boltzmann equations as proposed by Allen [All87]. This system of equations conserves the energy that is transfered from electrons to phonons and vice versa. In the spirit of the two-temperature model, the change in temperature is determined by the transfered energy from the one to the other subsystem. The electron-phonon energy transfer rate is given by a moment of the Bose distribution function $n_B(q,t)$ for the phonons [All87]

$$Z_{ep}(T_e,T_l,t) = \frac{\partial E_p(t)}{\partial t} = \sum_q \hbar\omega(q,T_e,T_l,t)\frac{\partial n_B(q,t)}{\partial t}\,. \tag{4.1}$$

Note that the phonon energies ω and therefore the energy transfer rate depend on the temperatures of the system. This moment can be obtained from the appropriate Boltzmann equation and reads in terms of the electron-phonon matrix element $M^q_{kk'}$ [All87]

$$\begin{aligned} Z_{ep}(T_e,T_l,t) &= \frac{4\pi}{\hbar}\sum_{qk}\hbar\omega_q(T_e,T_l,t)|M^q_{kk'}(t)|^2 S(k,k',t) \\ &\quad\cdot\delta\big(\varepsilon(k)-\varepsilon(k')+\hbar\omega(q,T_e,T_l,t)\big). \end{aligned} \tag{4.2}$$

The phonon and electron wave vectors are connected via $k-k'=q$ and the difference in single electron energies $\varepsilon(k)$ has to match the phonon energy $\hbar\omega(q)$. The thermal factor $S(k,k')$ is given by

$$S(k,k',t) = \big[f(k,t)-f(k',t)\big]\,n_B(q,t) - [1-f(k,t)]\,f(k',t) \tag{4.3}$$

and accounts for Pauli blocking in the scattering process of electrons via the occupations described by the Fermi functions $f(k,t)$. The standard approach in calculating this expression is to introduce the Eliashberg function as a generalized electron-phonon matrix element [All87]

$$\begin{aligned} \alpha^2F(\varepsilon,\varepsilon',\omega) &= \frac{2}{\hbar N_c^2 g(\varepsilon_F)} \\ &\quad\cdot\sum_{kk'}|M^q_{kk'}|^2\delta(\omega-\omega(q))\delta(\varepsilon-\varepsilon(k)\delta(\varepsilon'-\varepsilon(k'))\,. \end{aligned} \tag{4.4}$$

Here, $g(\varepsilon_F)$ denotes the value of the electronic density of states (DOS) at the Fermi edge. Variations of the Eliashberg function are found on a meV scale, whereas the typical structure of the electronic DOS varies on an eV scale. Thus, following X. Y. Wang *et al.* [Wan94], the approximation

$$\begin{aligned} \alpha^2F(\varepsilon,\varepsilon',\omega) &= \frac{g(\varepsilon)g(\varepsilon')}{g^2(\varepsilon_F)}\alpha^2F(\varepsilon_F,\varepsilon_F,\omega) \\ &= \frac{g(\varepsilon)g(\varepsilon')}{g^2(\varepsilon_F)}\alpha^2F(\omega)\,. \end{aligned} \tag{4.5}$$

is introduced here. Based on the same argument of scale between the phonon energies and the electronic energies, differences in the Fermi-distribution can be expressed as

$$f_e(\varepsilon-\hbar\omega)-f_e(\varepsilon) = -\hbar\omega\frac{\partial f_e(\varepsilon)}{\partial\varepsilon}\,, \tag{4.6}$$

and the electronic density of states

$$g(\varepsilon_F+\hbar\omega(q)) \sim g(\varepsilon_F). \tag{4.7}$$

This results in [Lin08]

$$\begin{aligned} Z_{ep}(T_e,T_l,t) = &-\frac{2\pi N_c}{g(\varepsilon_F)} \\ &\cdot\int_0^\infty d\omega(\hbar\omega)^2\alpha^2F(\omega,T_e,T_l,t)\Big[n_B^e(\omega,T_e)-n_B^p(\omega,T_l)\Big] \\ &\cdot\int_{-\infty}^\infty d\varepsilon\, g^2(\varepsilon)\frac{\partial f_e(\varepsilon,T_e)}{\partial\varepsilon}\,. \end{aligned} \tag{4.8}$$

The Bose functions contain the electron temperature in n_B^e and the lattice temperature in n_B^p. Input quantities are therefore the electron DOS $g(\varepsilon)$ and the Eliashberg function $\alpha^2F(\omega)$.

The heat capacities can be obtained from the various density of states. For the electrons, one finds

$$C_e(T_e,t) = \int_{-\infty}^\infty \frac{\partial f(\varepsilon,T_e,t)}{\partial T_e}g(\varepsilon)\varepsilon d\varepsilon\,. \tag{4.9}$$

Similarly, the lattice heat capacity is given by

$$C_l(T_l,t) = \int_{-\infty}^{\infty} \frac{\partial n_B(\varepsilon,T_l,t)}{\partial T_l} h(\varepsilon)\varepsilon d\varepsilon \,, \tag{4.10}$$

where $h(\varepsilon)$ denotes the phonon DOS.

4.1.2. The electron-phonon coupling in the time domain

In the past, a range of experimental techniques have been employed to investigate the electron-phonon coupling of metals quantitatively in equilibrium and non-equilibrium situations. Among the first were measurements of the phonon lifetime by neutron diffraction [Ste67], which, however, depend on electron-phonon and phonon-phonon scattering rates. The Eliashberg functions of metals have been determined by electron tunneling spectroscopy [McM65], which have to be done in the superconducting state at low temperatures. Angle-resolved photoelectron spectroscopy has been used to measure the electron-phonon coupling near surfaces through the experimental determination of the electron self-energy [Plu03].

Time-resolved measurements have also been applied to quantify the coupling between electrons and phonons. The most common approach is time-domain thermoreflectance measurements [EA87, Sch87a, Bro90]. While these measurements are easy to implement, the relation between spectroscopic observables, e.g. the reflectivity, and physical quantities of the non-equilibrium system is, in general, nontrivial. In particular, the respective contributions of electronic excitation, increasing phonon population and thermal expansion to the transient reflectivity are *per se* unknown and approximated by linear dependencies. Time-resolved photoelectron spectroscopy provides a more direct access to transient electron distributions which can be related to the electron-phonon interaction [Sen13]. In the case of simple metals, however, its intrinsic surface sensitivity makes a disentanglement of electron relaxation via the coupling to the phonon system, and electron transport out of the probed sample volume virtually impossible [Bau98, Hop09]. Strong exciting laser fields create surface charges, which disturb the measured signal and restrain these measurements to low excitation densities. Time-resolved diffraction provides direct information on the vibrational excitation of the crystalline lattice via the Debye-Waller effect (see chapter 3.2). The quantitative investigation of electron-phonon coupling in simple metals requires a high temporal resolution, not available in time-resolved electron diffraction until recently, and had not yet been undertaken to date.

The connection between the diffraction experiments and the theory, presented in the previous section, is given by the energy-transfer rates Z_{ep}. The standard approach in describing the dynamics of the excited material is the two-temperature model, which assumes phonons to follow Bose-Einstein and electrons to follow Fermi-Dirac statistics at all times. In the following sections, the TTM is applied on the diffraction data and is then expanded to investigate the implications of a non-thermal lattice on the temporal evolution of electron and phonon distributions. The electronic subsystem is in both cases assumed to be thermal at all times, since the non-equilibrium electron distribution, induced by the laser pulses, relaxes on the timescale of 10 fs [Bau98, Mue13], which is much shorter than the timescales of interest in this investigation. Additionally it is assumed that a spatially inhomogeneous excitation in the surface's normal direction due to the absorption profile of the laser relaxes on on the sub-100 fs time scale via fast electron transport [Bau98].

4.1.3. Electron diffraction measurements

All electron diffraction experiments of this chapter were done with the setup described in chapter 2. Special care was taken in the alignment of the setup to achieve an optimal time-resolution. The voltage was set to 98 kV at a cathode-anode distance of 8 mm. The output of the NOPA was attenuated to have an average of around 1000 electrons per pulse. According to the simulations presented in 2.1.3, the time-resolution is expected to be on the order of 100 fs.

The aluminium samples were bought from Plano GmbH. They are free-standing polycrystalline films of aluminium on standard TEM grids and have a nominal thickness of 32 nm. A typical diffraction image of these aluminium samples is shown in the inlet of figure 4.2 a), which was taken with an integration time of 5 seconds. By averaging the diffraction images in angular direction, as described in appendix A, radial averages (RAs) are obtained. For the later analysis, RAs of four to ten delay-scans were recorded and averaged. A typical radial average of aluminium is shown in figure 4.2 a) and the most prominent diffraction peaks are labeled. From the RAs, the peakheights and the background of inelastically scattered electrons are determined for every pump-probe delay by fitting pseudo-Voigt line profiles and an empirically chosen background function (Lorentzian + fourth order polynomial). A few refinement steps are used to increase the quality of the fit, as described in detail in appendix A. In this study, the energy of the pump pulses was varied to achieve absorbed energy densities in a range of 125 J/cm^3 to 840 J/cm^3. For the highest intensities, the repetition rate of the laser

was reduced to 500 Hz with a chopper wheel to avoid temperature offsets prior to time zero from consecutive pump pulses.

The evolution of the relative intensity of three selected Bragg-peaks, as well as changes in the integrated background between scattering vector $s = 0.2$ and $1.95\,\text{Å}^{-1}$, are plotted as a function of pump-probe delay in figure 4.2 b). The absorbed energy density in the measurement was $440\,\text{J/cm}^3$.

The intensity of all peaks decreases after photoexcitation at $t = 0$ and reaches a new steady-state within one picosecond. On the same timescale the intensity of diffusely scattered electrons in the background increases. Both can be attributed to a transfer of energy from excited electrons to the lattice. The energy transfer to the lattice leads to a larger amplitude of the atoms movements, and therefore a higher time-averaged mean square displacement $\langle u^2 \rangle$ from their equilibrium position. As discussed in chapter 3, this motion decreases the intensity of the Bragg diffraction peaks.

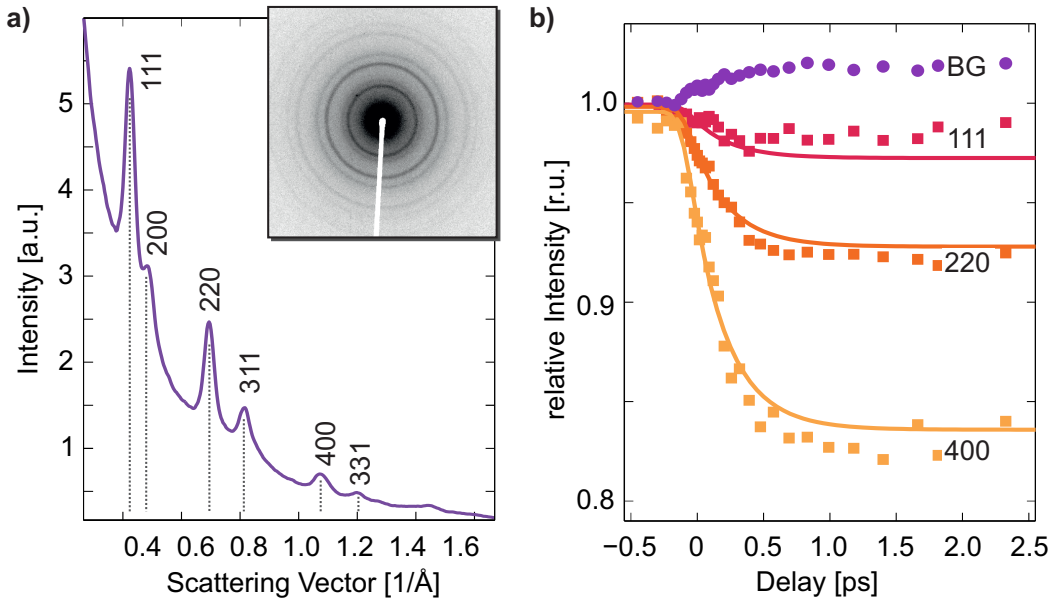

Figure 4.2.: **a)** Radial average of aluminium with the raw diffraction image, from which it is calculated, shown in the inlet. The most pronounced Bragg reflections are labeled. **b)** Temporal evolution of the relative intensity of three diffraction peaks and the integrated background. The solid lines are a global fit to all diffraction peaks (details in the text), showing that the lattice vibrations are isotropic.

The measured relative intensities of the Bragg peaks $I_{\mathrm{rel}}(t)$ can be represented in a form that does not depend on the scattering vector and therefore allows for averaging of all fitted peak heights (see also equations 3.9 & 3.8)

$$-\frac{3}{4\pi^2}\frac{\ln(I_{\mathrm{rel},s}(t))}{s^2} = \langle u^2\rangle(t) - \langle u^2\rangle(t < t_0). \tag{4.11}$$

In the following, the (111), (220) and (311) reflections as well as the averaged (331)/(420) and (531)/(442) reflections, the latter of which are too close together to be separated during fitting, are taken into account. A fit of this averaged quantity with a mono-exponential decay, convoluted with a Gaussian function of 150 fs FWHM, yields a time constant of $\tau = 350 \pm 45$ fs for the dataset shown. The background rises with a time constant of $\tau = 270 \pm 20$ fs. The solid lines in Fig. 4.2 b) are derived from the mono-exponential fit to the averaged quantity by inversion of Eq. (4.11). The amplitude and temporal evolution of each peak is reproduced well by the fit, indicating that the energy transfer from electrons to phonons is isotropic.

Both time constants from the fit are significantly shorter than previously reported values, but larger than the convolution width of 150 fs, which accounts for the instrument response function. Reported values for the lattice heating time constant of aluminium are (550 ± 80 fs, [Nie06]) for the lattice temperature increase, (1.0 ± 0.1 ps, [Zhu13]) for the Bragg peak decay time and (0.7 ± 0.1 ps, [Zhu13]) for the rise-time of the intensity of inelastically scattered electrons. All experiments were done at comparable excitation levels. A possible explanation is therefore the limited time-resolution of the cited experiments, which was in all cases very close to the measured time constants.

4.1.4. Two-temperature model

In the TTM, the temporal evolutions of the electronic and phononic subsystems are described by two coupled differential equations, which quantify the energy flow between them. The electron-phonon coupling parameter $G_{ep} = Z_{ep}/(T_e - T_l)$ and the heat-capacities C_e and C_l connect the energy flow to the temperature difference $(T_e - T_l)$ of electrons and lattice

$$C_e(T_e)\frac{\partial T_e}{\partial t} = G_{ep}\cdot(T_e - T_l) + f(t - t_0)\,, \tag{4.12a}$$

$$C_l(T_l)\frac{\partial T_l}{\partial t} = G_{ep}\cdot(T_e - T_l)\,. \tag{4.12b}$$

The function $f(t)$ models the energy input from the laser system and is taken here as a Gaussian function of 50 fs FWHM, close to the measured pump laser pulse duration. Its temporal integral is the energy density u_E, which is injected into the system.

For a comparison of the data to the predictions of the model, the measured Bragg-peak intensities are converted into a mean-square displacement according to Eq. (4.11). Tabulated data of the equilibrium Debye-Waller B-factor [Pen04] is then used to translate this into a lattice temperature. The lattice temperatures reached at long delay times are in good agreement with the expected temperature rise calculated from the absorbed energy density and the static heat capacity of aluminium, showing that the fit of the peak intensities converges reliably.

The differential equations (4.12a) of the TTM are solved numerically to obtain the theoretical evolution of the electronic and the lattice temperatures. The electronic and lattice heat capacities C_e and C_l are taken from the DFT calculations, which are described in detail in [Wal16]. By leaving the absorbed energy density u_E, the electron-phonon coupling parameter $G_{ep} = G_{ep}(u_E)$ and the zero time of the experiment as a free parameter, the difference of the experiment and the TTM are numerically minimized. For a detailed description of the fitting procedure and its implementation, see appendix B. The data (circles) is plotted together with the best fits obtained (solid lines) in figure 4.3 a) for three datasets. In the entire range of employed excitation densities, the TTM is able to excellently reproduce the data. The fitted coupling parameters are shown in figure 4.3 b). However, using the electron-phonon coupling from the first principle calculations (see section 4.1.1) as an input to the TTM, the model predicts a rise time of the lattice temperature which is too quick in comparison to the data.

Z. Lin *et al.* introduced a temperature dependent electron-phonon coupling, which they retrieved from DFT calculations [Lin08]. The increase in the fitted coupling parameter with increasing excitation density of this work confirms that the effect of electronic temperature on the coupling parameter can not be neglected, since a higher excitation density is equivalent to a higher average of electronic temperature during the relaxation dynamics. Therefore, a temperature-dependence of the coupling parameter $G_{ep} = G_{ep}(T_e)$ is included in the fit of the two-temperature model. The electronic-temperature dependence is restricted to being linear, $G_{ep}(T_e) = g_0 + g_1 \cdot T_e$, as for more complicated dependences the fits do not converge. For a description of the implementation in the fits, see appendix B. The result is shown in figure 4.3 c) as solid blue line with the shaded area indicating the 1-σ error. The data is shown up to a temperature of 4000 K, which is the highest electronic temperature $T_e(t)$ transiently reached at the highest excitation density. The dotted line is the result of Z. Lin *et al.* and the solid

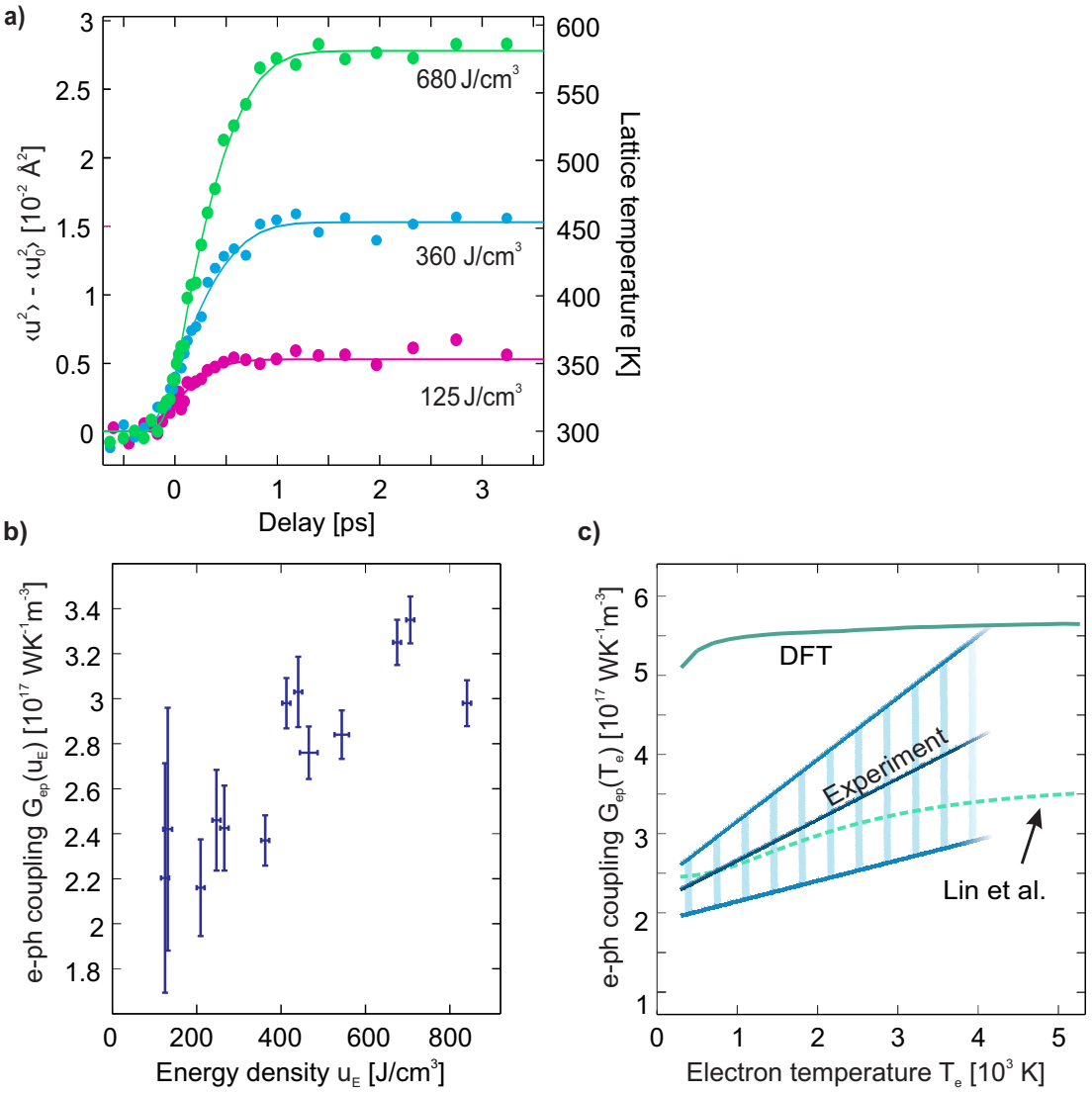

Figure 4.3.: **a)** Measured lattice temperature (circles) and simulated temperature with a TTM with optimized parameters. **b)** Electron-phonon coupling parameter G_{ep} as a function of absorbed energy density u_E. **c)** Electron-phonon coupling dependence on electronic temperature obtained by averaging all measurements. The shaded gives visualizes the standard deviation. The green line shows $G_{ep}(T_e)$ obtained from DFT calculations by evaluating Eq. (4.8). The dashed light green line is the result from [Lin08].

green line corresponds to the coupling parameter, which is calculated by integrating over the Eliashberg function (equation 4.8) shown in figure 4.1.

Whereas the experimentally determined $G_{ep}(T_e)$ is in good agreement with the results from [Lin08], a qualitative and quantitative disagreement with $G_{ep}(T_e)$ from the first principle DFT calculations shown here is found. First, the low-excitation limit of the experimental G_{ep} is approximately a factor of two smaller than the value obtained from the *ab initio* calculations. Second, the T_e-dependence of the theoretical $G_{ep}(T_e)$ is much less pronounced compared to the experimental results. The good agreement between the experimental results and the theoretical results of [Lin08] are, however, presumably artificial. In brief, the low T_e onset of their theoretical curve is scaled with the value obtained from thermoreflectance measurements employing a TTM analysis [Hos99]. The agreement in the low-T_e onset of G_{ep} therefore indicates consistency of the TTM analysis presented here with the results of [Hos99] in the same framework, rather then with the calculations. The shape of the curve of Z. Lin *et al.* might be dominated by an artifact due to technical details of the DFT calculations [Wal16].

In summary, the analysis of the diffraction data and the first principle calculations in the framework of a TTM lead to a quantitative disagreement of the resulting coupling parameters $G_{ep}(T_e)$. In the following section, a new approach in the interpretation of the coupling is presented, which lifts the assumption of thermal phonon distributions.

4.1.5. Non-thermal lattice model

The comparison of Eliashberg function and phonon DOS, shown in Fig. 4.1, reveals a strong coupling of electrons to phonons of high frequencies. This implies that the laser-induced non-equilibrium between electrons and phonons transiently leads to non-thermal phonon distributions. In other words, the phonon distribution is not resembled by the product of a Bose-Einstein function and the phonon DOS for a certain time during electron-phonon equilibration. For other materials exhibiting strong coupling to specific phonon modes, this view is well established. Examples include graphite [Sch11, Cha14] or antimony, which is studied in chapter 4.2.

With its unit cell containing one atom, aluminium exhibits three acoustic phonon branches. Their contributions to the phonon DOS have been studied by static diffraction techniques and have been found to be well separated in frequency [Wal56, Ste67]. Similarly, the contribution of the three phonon branches to the Eliashberg function can be identified. M. M. Dacorogna *et al.* calculated the phonon branch and $\vec{q}$-resolved electron-phonon coupling in aluminium along high-symmetry directions and concluded that there was no dominant contribution from a specific phonon branch [Dac85]. DFT

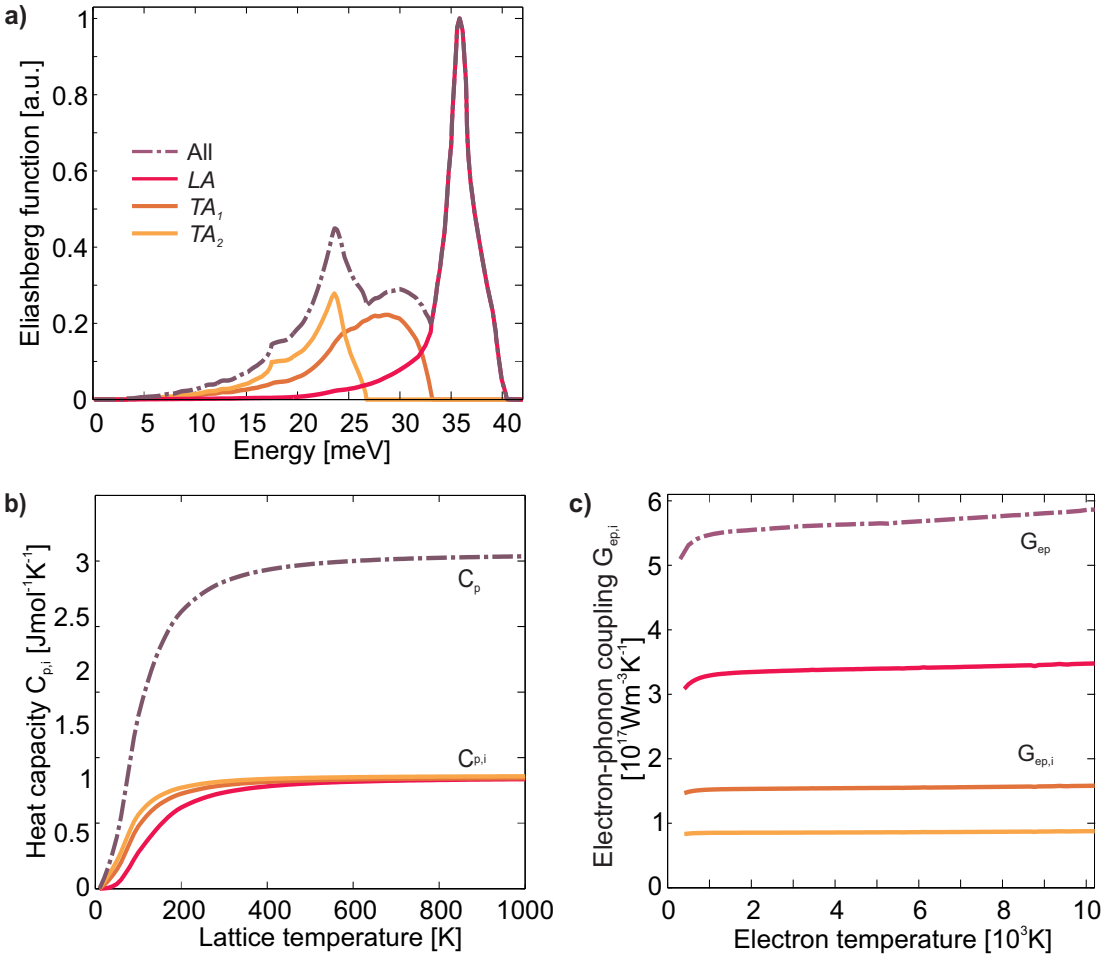

Figure 4.4.: **a)** DFT calculation of the Eliashberg function and the contributions of the three acoustic phonon branches $\alpha^2 F_i(\omega)$ to it, with $i = TA_1, TA_2, LA$. **b)** Heat capacities of the three phonon branches and of the entire lattice as a function of lattice (branch) temperature. **c)** Electron-phonon coupling $G_{ep}(T_e)$ calculated for the entire lattice and the individual phonon branches $G_{ep,i}(T_e)$ as function of electronic temperature.

calculations performed in the full Brillouin zone lead to a different picture. Figure 4.4 a) shows the individual contributions of the three phonon branches to the Eliashberg function. These are calculated from the partial Eliashberg functions, as described in [Wal16]. A clear spectral separation of the three contributions is observed, in particular, the high frequency peak dominating α^2F can completely be attributed to the longitudinal acoustic (LA) phonon branch. The partial phonon DOSs and Eliashberg functions are used to calculate the heat capacities $C_{p,i}$ and, with Eq. (4.8), the coupling parameters $G_{ep,i}$ of the three branches $i = TA_1, TA_2, LA$ as a function of electronic temperature T_e. The values are compared to those of the entire phonon spectrum in Figs. 4.4 b) & c). Whereas the partial heat capacities are very similar for all T_l relevant in this work (i.e. above room temperature), the electron-phonon coupling differs by up to a factor four between the TA_2 and the LA branch.

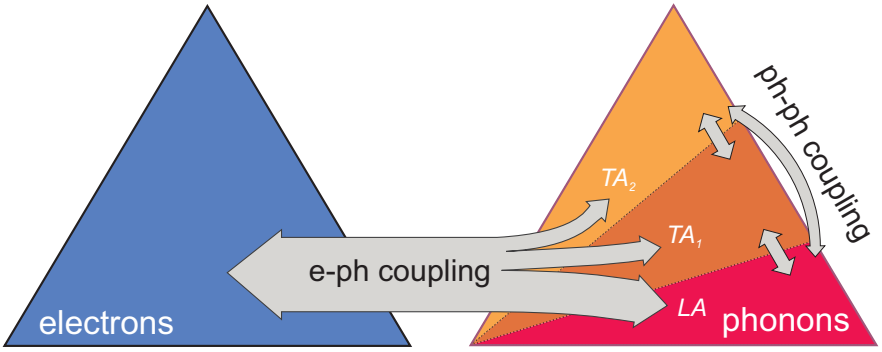

Figure 4.5.: Depiction of the concept of the non-thermal lattice model: The phonon-system is divided into subsystems (corresponding to the three acoustic phonon branches). An electron-phonon coupling parameter is calculated for each phonon branch and the energy-transfer is treated separately. In addition, the branches exchange energy between them via phonon-phonon coupling.

With the partial coupling constants and heat capacities at hand, the TTM is now expanded and a new model ('non-thermal lattice model', NLM) is introduced, which allows for non-equilibrium between individual phonon subsets. A schematic drawing of the NLM is shown in Fig. 4.5. The phonon subsets are chosen to correspond to the three phonon branches, and each branch is assumed to be thermal and thus defined by a temperature $T_{p,i}$. To account for phonon-phonon scattering processes, leading to a direct transfer of energy between branches i and j, a phonon-phonon coupling parameter $G_{pp,ij}$ is introduced. Due to a lack of experimental or theoretical determination and for increased stability of the fits, it is assumed to be of same magnitude between all branches $G_{pp,ij} = G_{pp}$. Its magnitude is determined by fitting the NLM to the experimental data. The energy flow is determined by the partial electron-phonon $G_{ep,i}$ and phonon-phonon

coupling constants and the temperature differences $(T_e - T_{p,i})$ and $(T_{p,i} - T_{p,j})$ between the subsystems. The evolutions are given by a set of four coupled differential equations

$$C_e(T_e)\frac{\partial T_e}{\partial t} = \sum_{i=1}^{N} G_{ep,i}(T_e) \cdot (T_e - T_{p,i}) + f(t - t_0), \tag{4.13a}$$

$$C_{p,i}(T_{p,i})\frac{\partial T_{p,i}}{\partial t} = G_{ep,i}(T_e) \cdot (T_e - T_{p,i}) + \sum_{j \neq i} G_{pp,ij} \cdot (T_{p,j} - T_{p,i}). \tag{4.13b}$$

The total energy transfer between electrons and lattice is in this model simply given by the sum of all partial energy transfers.

In the framework of the NLM, a conversion of the measured mean square displacement to a lattice temperature via the Debye-Waller B-factor is not meaningful. Instead, the temperatures of each phonon branch calculated by the model can be transferred to the total MSD of the atoms, which can then be compared to the measurements. The contribution of each phonon branch is calculated from the respective temperatures by applying equation 3.5 to the normalized partial phonon density of states $h_{n,i}(\omega)$

$$\langle u_i^2 \rangle = \frac{3\hbar}{2M} \int_0^\infty \coth\left(\frac{\hbar\omega}{2k_B T_{p,i}}\right) \frac{h_{n,i}(\omega)}{\omega}\, d\omega. \tag{4.14}$$

With the phonon branches being orthogonal, the total MSD is calculated from the individual contributions by summing up their contributions

$$\langle u^2 \rangle = \sum_{i=1}^{3} \langle u_i^2 \rangle. \tag{4.15}$$

Figure 4.6 a) compares the MSD determined experimentally with the MSD obtained with the optimized solution of the NLM, where $C_e(T_e)$, $C_{p,i}(T_{p,i})$ and $G_{ep,i}(T_e)$ are taken from the *ab initio* calculation and G_{pp}, u_E and t_0 are optimized iteratively. The only free parameter affecting the dynamics of the MSD is G_{pp}. Note that for a $G_{pp} \to \infty$, the dynamics of a TTM are obtained. An excellent agreement between data and NLM is found for all performed measurements using a phonon-phonon coupling of $3.5 \cdot 10^{17}\,\mathrm{W/(Km^3)}$. Even though literature values for phonon-phonon couplings are elusive for aluminium, it has been concluded from neutron-diffraction measurements that electron-phonon and phonon-phonon coupling are of similar magnitude [Tan10], which is consistent with the observation here.

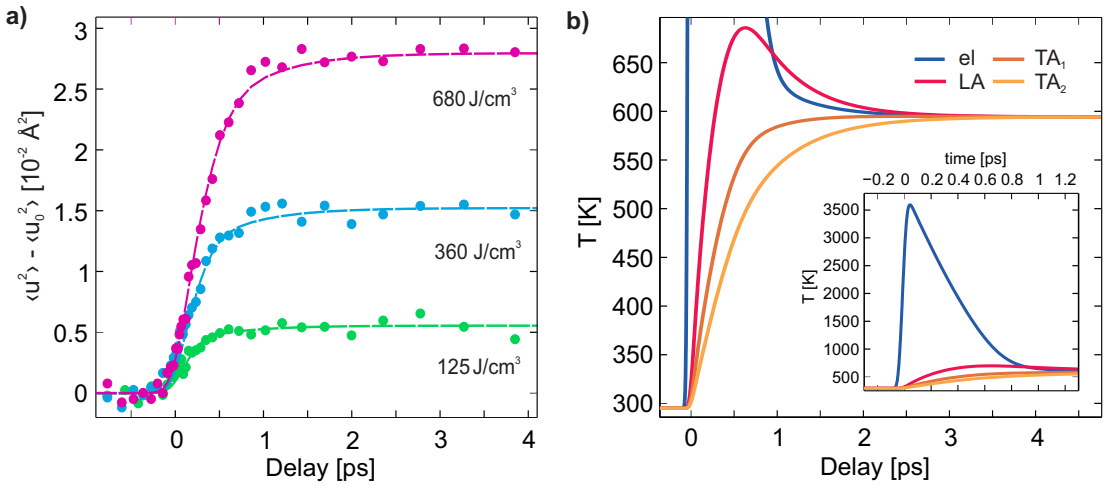

Figure 4.6.: **a)** Measured mean square displacement (MSD) as a function of delay (circles) and calculated evolution predicted by the non-thermal lattice model with a phonon-phonon coupling of $3.5 \cdot 10^{17}$ W/(m^{3}K) (dashed lines). All other material parameters were taken from DFT calculations. **b)** Evolution of the temperatures of electrons (blue, inset) and the three phonon branches for the same parameters as in a).

Figure 4.6 b) shows the temperatures $T_e(t)$ and $T_{p,i}(t)$ of the optimized solution of the NLM. The different evolution of the temperatures of the three branches is striking and shows the transient non-thermal state of the phonons. As expected from the previous discussion, $T_{p,LA}$ rises faster than the temperature of the transverse branches. It overshoots to a maximum temperature before it decreases again and eventually equilibrates with the two other branches.

4.1.6. Energy flow in the models

Whereas the TTM and the NLM can both be applied to describe the temporal evolution of the measured MSD with similar quality, the two models differ significantly in their physical implications. An important practical difference is the predicted dynamics of the energy flow between electrons and phonons. Figure 4.7 shows the evolution of the energy content in electrons and phonons, which is first injected into the system by the laser pulse through excitation of the electrons at $t = 0$. The energy content in the electron- and phonon systems is calculated from their temperatures calculated by the two models and the respective heat capacities. In the NLM, the energies of the three phonon branches are summed up to obtain the total gained energy in all lattice degrees of freedom.

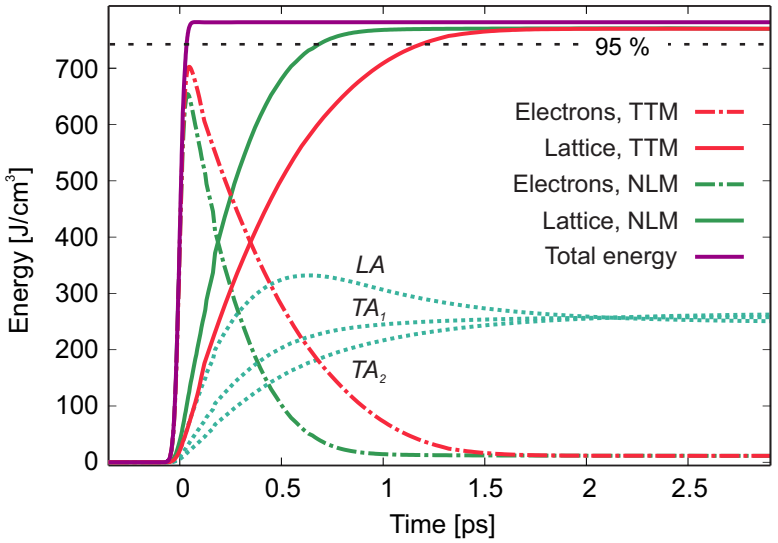

Figure 4.7.: Temporal evolution of the energy content in the electronic and lattice subsystems retrieved from the solutions of the NLM and the TTM, best fitting the data. The black dashed line indicates 95% of the energy which is eventually transferred from electrons to the lattice. The delay time at which 95% of the energy is transferred differs by around 50%.

It can be seen that the energy transfer from electrons to the lattice proceeds significantly faster in the NLM. The dotted line indicates the energy level corresponding to 95% of the energy, which is eventually transferred to the lattice. Between the two models, the time at which this level is reached differs by 40-60% for a given excitation density and ranges from as short as 300 fs in the NLM at low excitations to slightly above 1 ps in the TTM at high excitation densities.

The few-100 fs timescale of energy transfer in aluminium shows that incoherent energy transfer from electrons to the lattice can be extremely fast. This implies that also photoinduced phase transitions occurring on a sub-picosecond timescale can be purely caused by incoherent energy transfer.

4.1.7. Implications of the non-thermal lattice model

The experimental basis of this chapter is the time-resolved measurement of the atomic mean-square displacement caused by all phonons of aluminium. A direct measurement of non-thermal phonon distributions could be done by the time- and momentum-resolved measurement of inelastically scattered x-rays [Tri10, Zhu15] or electrons of a single-crystalline thin film of aluminium. The refinement of the description of electron-

phonon coupling including phonon-specificity is not only relevant for the evolution of impulsively generated strongly non-equilibrium states [Siw03, Leg13]. Equally important, in quasi-stationary non-equilibrium situations like the flow of electrical current caused by an electrical potential difference, energy dissipation from the electrons to the lattice is governed by the same coupling phenomena.

The concept of subdividing the lattice degrees of freedom into phononic subsystems for describing the energy flow in a material, as introduced here for the case of aluminium, may be applied to a range of materials. In the case of metals, a pronounced spectral dependence of $\alpha^2(\omega)$ suggests that this approach should be followed. A subdivision into the phonon branches may even be a necessary approach to accurately describe the dynamics of all materials, which show strong spectral or phonon-branch dependences and in which the phonon-phonon coupling is not much larger than the electron-phonon coupling. More complex materials may require partitioning into a larger number of phononic subsystems, specifically if strongly coupled modes are involved (see also chapter 4.2). Another refinement, which can be implemented in a similar way, are non-thermal electron-distributions, which might need to be considered for materials exhibiting weak electron-electron scattering [Mue13]. *Ab initio* calculations can provide guidance for identifying the appropriate subsystems, as demonstrated here.

4.2. Non-equilibrium phonon dynamics in antimony

Whereas in a perfect metal electrons are quasi-free and almost perfectly delocalized, most other materials exhibit more complex electronic states or bands. Accordingly, the excitation of electrons in between bands is more likely to change the real-space electronic distribution. This modifies the average Coulomb forces on the nuclei and therefore the potential energy surface of the lattice. Such materials include group IV semiconductors like Si, where photoexcitation drives transitions from bonding- to antibonding states [Har08], some metal oxides where the bonding orbital character changes [Bot13], materials with ionic bonding [Sti12] or charge density wave (CDW) systems [Eic10] as well as Peierls-distorted systems like Bi and Sb, in which electron-lattice correlations play a big role. Photoexcitation of those materials with short laser pulses does therefore not induce relaxation dynamics in an unperturbed potential energy landscape, but rather modifies the landscape itself, adding to the complexity of the description of non-equilibrium dynamics.

Changes of the potential energy surface can occur as changes of its slope [Ern09] or the position of its minima [Zij06]. The latter modifies the equilibrium position of an atom in the crystal structure and triggers an adjustment of the atom's average position. With atomic motion being fairly slow, photo-induced changes of the potential energy surface by femtosecond laser pulses occur almost instantaneously on the timescale of the oscillation period of the nuclei. In such a situation, the resulting motion towards the new minimum of all atoms is initiated collectively. The resulting motion is a driven oscillation of all atoms around their new potential energy minimum, as described in detail in chapter 3.3. Such coherent vibrations have first been observed in the 1980's, when some groups found oscillations in optical pump-probe measurements on molecules [De 85, Ros86]. Shortly after, oscillations were also found in similar measurements on the semimetals antimony and bismuth [Che90, Zei92].

The appearance of fairly large coherent oscillations of the lattice in Sb can be related to its, compared to other elements, rather unusual potential energy surface and crystal structure. A sketch of the crystal structure is shown in figure 4.9. Antimony crystallizes in an α-arsenic (A7) lattice, which can be seen as a distorted simple cubic structure. Driven by a Peierls-like instability (for a general introduction see e.g. [Pat10]), a (fictive) cubic unit cell is elongated along one of the body diagonals, i.e. the (111)- or z-direction. In a second step, atoms on this line pair up [Nee86]. The energy cost that such a lattice distortion demands, is overcompensated by the gain of energy in the electronic system. Figure 4.9 b) shows a calculation of the potential energy surface of bismuth

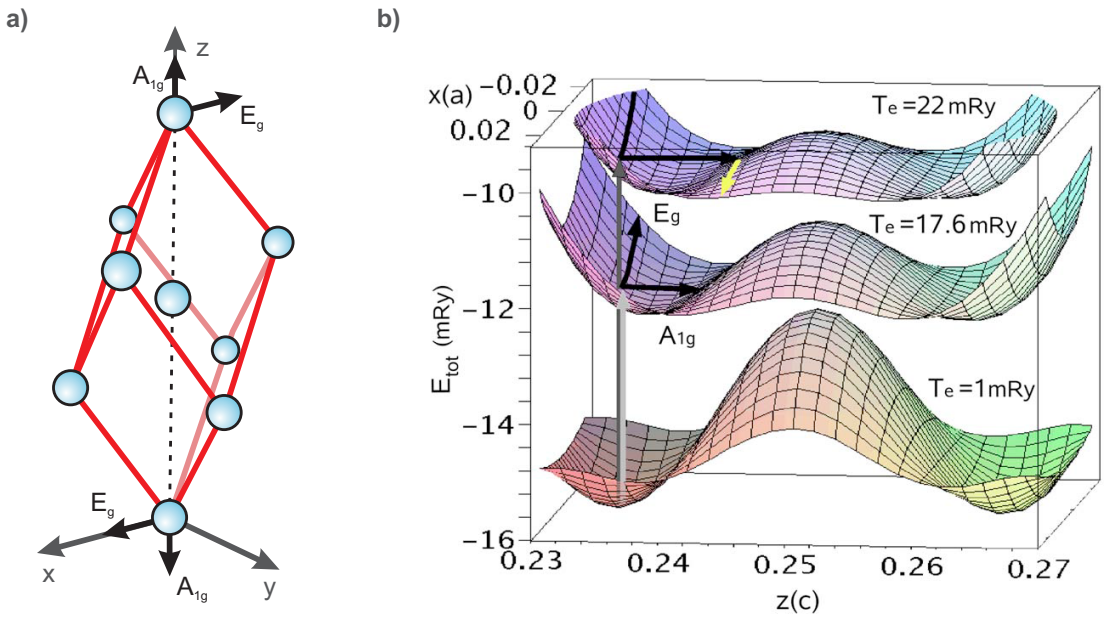

Figure 4.8.: Unit cell of antimony. The A7 structure is obtained by a Peierls-like distortion of a simple cubic structure. The direction of A_{1g} and E_g phonon modes are depicted. Adapted from [Ish10]. **b)** Calculation of the potential energy surface for the ground and electronically excited states of bismuth (qualitatively similar for antimony, see text). Excitation changes the position of the minima along the (111) direction, what leads to the displacive excitation of A_{1g} phonons. Taken from [Zij06].

[Zij06, Dia09], which demonstrates the effect of the Peierls-instability. Due to the largely similar structural and phononic properties of antimony, the surface is assumed to be qualitatively similar in antimony [Ish08]. The landscape exhibits two minima of the potential energy surface, which are in equal distance to the position of an unperturbed cubic unit cell at $0.25 \cdot c$, where c is the size of the unit cell in z-direction. The two minima are initially equivalent, but the atoms along the z-direction are trapped alternatingly in the left or the right one, leading to an alternation of long and short bonds, i.e. a pairing of atoms. At elevated electronic temperatures, which is achieved e.g. by photoexcitation (gray arrow), the minimum of the potential energy surface shifts in the z-direction towards the more symmetric point of the cubic structure. A sudden transition between the two states is accomplished e.g. by femtosecond laser pulses and it constitutes a model case of the DECP-mechanism, described in chapter 3.3. Since the direction of motion of the excited phonon mode does not change the symmetry of the crystal structure, it is named A_{1g} mode [Dre08]. Its direction is depicted as black arrows in a) and b).

The excitation and the decay of coherent phonons in antimony and bismuth has been studied extensively by optical techniques in a wide range of excitation conditions, i.e. at various temperatures, pump photon energies and excitation densities (e.g. [Has98, Ste02, Ish06, Ish08]). Whereas the DECP mechanism of the excitation of coherent phonons could be deduced from these measurements [Zei92, Zij06] and is widely accepted, the decay of oscillations in the optical signals can have different origins. Two processes contribute to the decay of the optical oscillations, namely dephasing of the phonons and decay by phonon-phonon scattering [Has10] or phonon-electron scattering, i.e. by energy transfer to other excitations. In experiments on bismuth, it was concluded that dephasing would only play a minor role [Has98, Bos08]. In another work, however, a revival of phonon oscillations was found [Mis04], which shows that dephasing does plays a role in the decay of the optical signal.

Other techniques have been applied to study properties of the coherent phonons in more detail. Using time- and angle resolved photoemission spectroscopy (trARPES), the dynamics of the electronic structure and the coupling of the coherent oscillations to specific electronic states was investigated [Pap12, Fau13]. Diffraction measurements have been applied to directly access the dynamics of the optical phonons near the melting threshold [ST03, Fri07]. Since these measurements were done at grazing incidence on bulk samples, they are influenced by carrier diffusion into the bulk [Joh08]. Above the threshold for melting the material, non-thermal dynamics have been observed on free-standing bismuth samples with time-resolved electron diffraction measurements [Sci09].

Despite the large amount of diverse studies on the dynamics of the excitation of coherent phonons, a full picture of the dynamics of antimony and bismuth after photoexcitation remains elusive. Specifically, the coupling of electrons to other lattice vibrations, and thus the relaxation dynamics of the potential energy surface, have not been measured directly, since suitable methods have so far not been available. In this section, the coupling of excited electrons to the coherent phonon modes as well as to all other phonons via incoherent electron-phonon scattering processes is studied. The simultaneous measurement of the two processes is enabled by electron diffraction measurements on polycrystalline Sb samples, which allow to follow both processes in parallel.

4.2.1. Free-standing samples

Antimony can be grown in single crystals of several millimeter size and then be polished in any crystallographic direction. However, the need for free-standing films in electron diffraction experiments sets constraints on such macroscopic preparation techniques.

Thin films of antimony can be obtained by vacuum deposition of a thin film of the material on a dissolvable substrate. The choice of substrate strongly influences the crystallographic orientation and the growth in crystalline domains (single crystalline / polycrystalline). On two of the most common substrates, NaCl and Mica, Sb has been reported to grow in a polycrystalline manner with a mixture of (100) and (110) orientations out of plane [Pat79].

The antimony samples used in the experiments of this chapter were prepared by the group of V. Pruneri at the ICFO in Barcelona. The samples were grown on two different surfaces. A layer of 30 nm of Sb and a 10 nm thick capping layer of Si_3N_4 were deposited on 1) a polished NaCl crystal and 2) on a 10 nm thick amorphous film of Si_3N_4, which had previously been deposited on the same type of NaCl crystal. The films were then transferred onto standard TEM grids by dissolving the NaCl in water and picking up the films floating on the surface. Hereby, the samples with a double-capping are expected to have a better stability, since the Si_3N_4 prevents contact to the water and thus oxidation.

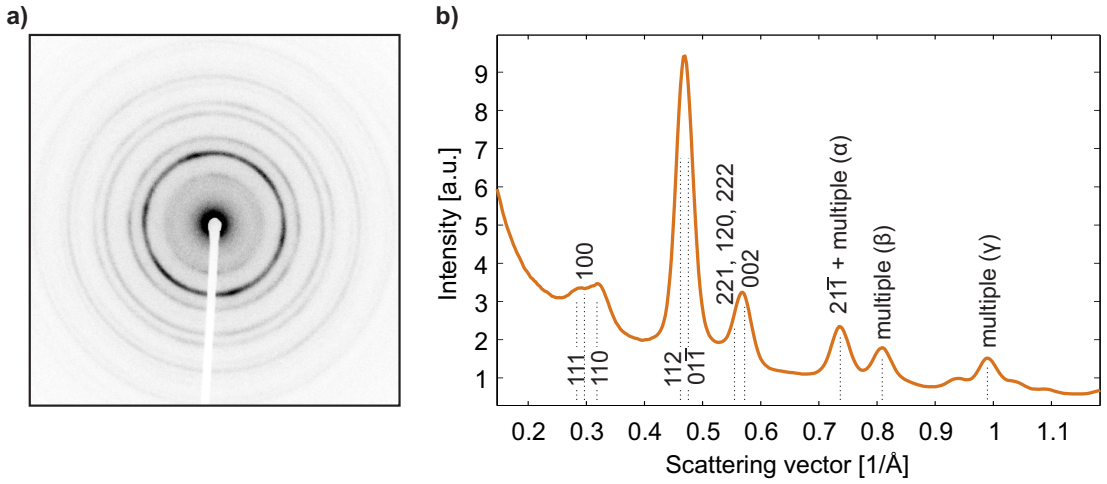

Figure 4.9.: a) Diffraction image of a thin polycrystalline antimony film. Small variations in the intensity in the angular direction show that the films have a preferential orientation. **b)** Radial average calculated from the diffraction image. The peaks used in the analysis are marked with dotted lines and labeled. At higher scattering vectors, measured Bragg peaks consist of several reflections and are therefore labeled with Greek letters for later referencing.

Figure 4.9 a) shows a diffraction pattern of antimony grown on amorphous Si_3N_4 and b) the radial average calculated from it. The very low intensity of the (110)-peak indicates that the sample is oriented, with the (110)-direction being normal to the surface. The radial averages show little variation in peak-intensity compared to the

ones grown on crystalline NaCl crystals, meaning that their orientation is similar and in the direction which is expected [Pat79]. The occurrence of other crystallographic phases, as reported for vapor-deposited films [Akh79] is not observed.

Variations in relative peak-intensity are found by taking diffraction images at different sample positions. This can be attributed to the macroscopic texture of the films. Investigating the films in an optical microscope with reflected light illumination, the films were found to be slightly crumpled, with 'hills' and 'valleys' of up to 10 µm height. Parts of the samples surface are therefore not normal to the electron beam, resulting in some reflections to gain and others to loose intensity.

With the microscopic orientation of the sample being similar, the double-capped samples with their better stability against oxidation are preferred over the single-sided capped samples. To ensure comparability of different experiments, all optical and diffraction measurements of this chapter were thus performed with the free-standing double-capped samples.

4.2.2. Optical detection of the coherent A_{1g} phonon mode

The dynamics of coherent phonons in antimony and bismuth have been studied with optical techniques for more than 20 years (see e.g. [Che90, Zei92, Has98, Kat13, Ish10]). The optical measurements performed here were done on the free-standing samples as a means of characterizing the samples via a comparison of the extracted phonon-frequencies to literature values.

Optical pump-probe measurements were done with the output of a Ti:Sa oscillator (Femtopower Femtosource) running at a repetition rate of 75 MHz. Its pulse duration was measured to be around 25 fs FWHM, with a spectral width of 90 nm. The fluence for exciting the phonons was fixed, and calculated to be around 0.1 mJ/cm^2. The transient reflectivity was measured at room temperature and the reflected intensities of the probe pulses are detected with a photo-diode, connected to a Lock-in amplifier.

Figure 4.10 a) shows a measured trace of the transient reflectivity. At the overlap of pump and probe pulses at $t = 0$, a large signal is measured, which is ascribed to be the result of electronic coherence [Pal84]. The oscillations induced by the pump pulse for times $t > 0$ are clearly visible for several oscillation periods until their amplitude has decreased to the noise-level after several picoseconds. The dotted line is obtained by applying a moving average of the curve with a window size close to one oscillation

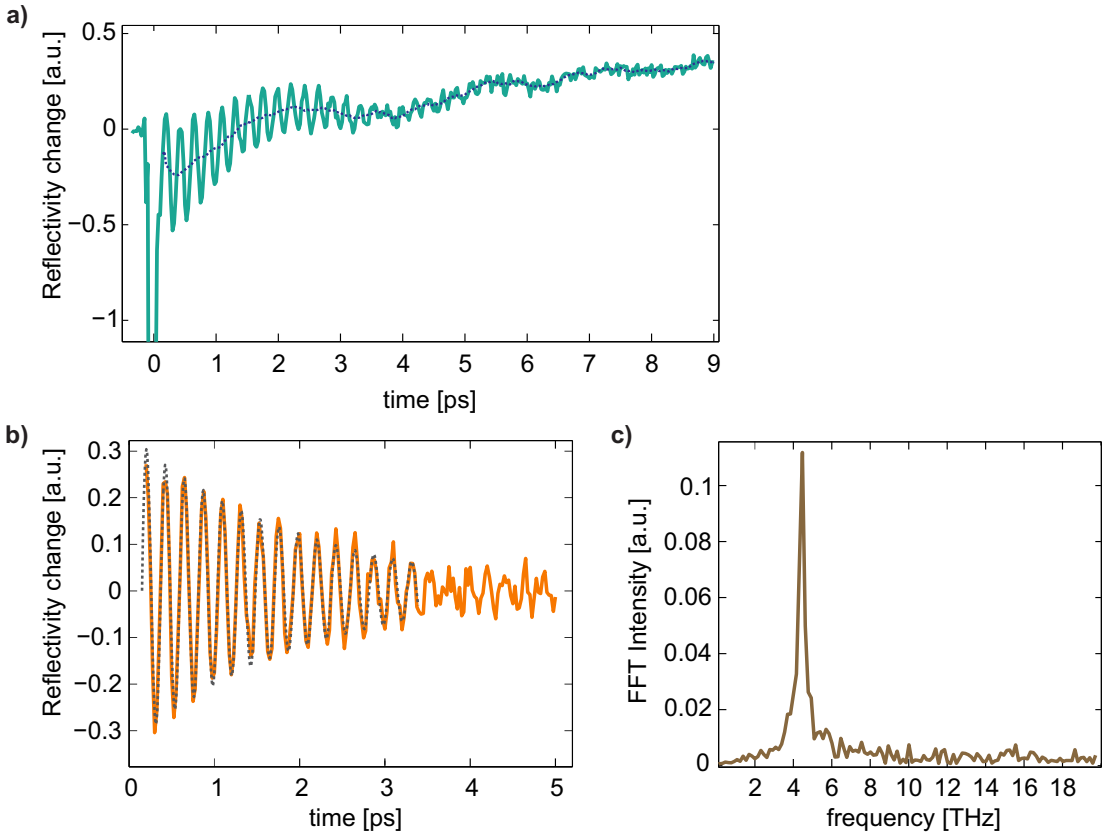

Figure 4.10.: **a)** Transient reflectivity trace of a thin film of Sb, excited with 30 fs, 800 nm laser pulses. The blue dotted line is the smoothed signal, which was subtracted to obtain: **b)** Data with long-term trend subtracted. The dotted line is a fit of a damped cosinusoidal oscillation. **c)** Fourier transform of b), showing a single frequency at 4.5 THz, in agreement with literature values.

period of the phonon. It thus only contains the long-term dynamics of the transient reflectivity.

Figure 4.10 b) shows the measured signal in a window from roughly 0 to 5 ps, from which the long-term dynamics have been subtracted. It thus predominantly contains the signal of the coherent phonon. In c), the Fourier-transform of the remaining oscillation is plotted. It shows a single frequency at 4.5 THz, which is in excellent agreement with previously reported frequencies of the A_{1g} mode of Sb at 300 K [Zei92, Ish08].

As seen in 4.10 b), the amplitude of the oscillation decays in the window of the measurement. A fit to the data with a cosinusoidal oscillation, multiplied by an exponential decay

$$I(t) = I_0 \cdot \cos(f/(2\pi) \cdot t + \Phi) \cdot \exp -t/\tau, \tag{4.16}$$

where f is the frequency of 4.5 THz and Φ is a phase, results in a very good fit. The timeconstant of the exponential damping is found to be τ of 1.95 ps, which is in the range of reported values [Zei92]. The timeconstant of the optically measured decay depends on the decay of the A_{1g} into different phonon modes via phonon-phonon coupling and via electron-phonon coupling, as well as on dephasing of the coherently excited phonons, the three of which are indistinguishable in the optical experiment.

4.2.3. Electron diffraction measurements

The diffraction experiments presented in this section were performed with the setup described in chapter 2.1. In addition to the general considerations about the alignment of the setup described there, several specific features of the Sb samples have to be considered. The intensity of the (111) peak, which is expected to most dominantly show the signatures of the coherent phonons, is very weak, since it is a super-lattice peak connected to the Peierls-distortion. With the (110) peak being very close in the diffraction image, a good spatial resolution is needed to be able to separate the two peaks. The best temporal resolution of the setup is achieved with the sample as close to the anode as possible, but the spatial resolution increases with distance from the anode. The position of the sample is therefore a compromise between temporal and spatial resolution. In the experiments here, an intermediate position with a distance of around 10 mm from the anode was chosen. At the time of the experiments, the voltage set to the photocathode could not exceed 90 kV due to instabilities of the photocathode and the electrical high-voltage feedthrough, which slightly lowers the accelerating electric field and with it the expected temporal resolution.

Diffraction images were taken with an integration time of 5 s. Radial averages are calculated from the images as described in appendix A and radial averages, taken with the same pump-probe delay, are then averaged (12 per delay point). A typical radial average is shown in figure 4.9. They are analyzed by fitting the background and the intensity of several diffraction peaks. The background function was empirically found to be well described with a $1/s^2$ dependence, where s is the scattering vector, and the peak shapes are fit with pseudo-Voigt line-profiles. For details on the fitting procedure see appendix A.

The evolution with pump-probe delay of the intensities of a set of Bragg-peaks for an incident fluence of 4.4 mJ/cm^2 is shown in figure 4.11 a). It can be seen that the temporal evolution of different Bragg-peaks are qualitatively different. Whereas the intensity of the (111)-peak drops almost instantaneously, the amplitudes of all other peaks decrease more slowly. The intensity of the (111) peak is only plotted for pump-

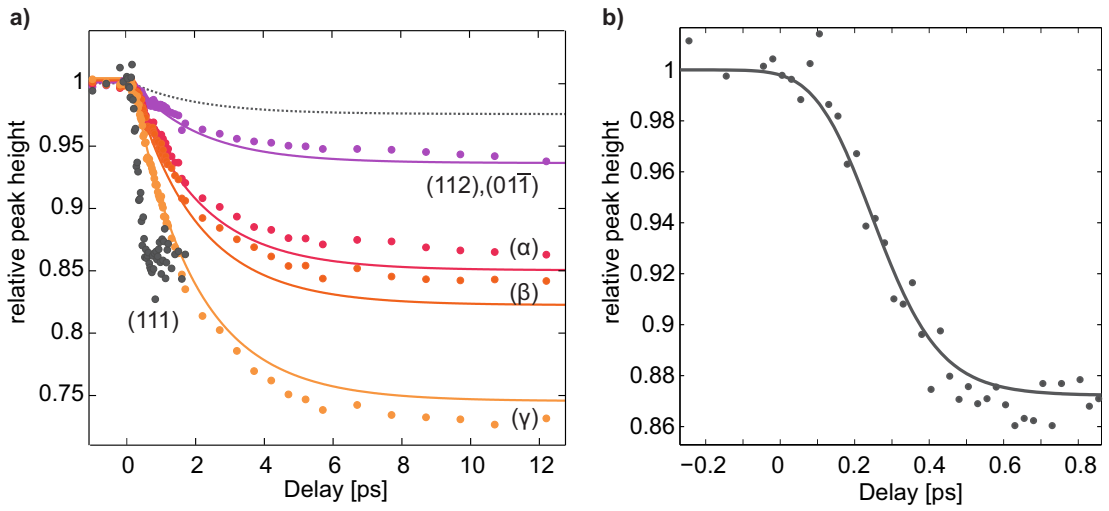

Figure 4.11.: a) Evolution of the intensity of several Bragg-peaks showing two distinct behaviors. The solid and dotted lines are derived from a global fit to all peaks excluding the (111) reflection. The dynamics of the (111) peak are clearly distinct from those of all other peaks. **b)** Zoom into the dynamics of the (111) peak. The drop in intensity is time-resolution limited. From the fit, an upper limit of the time-resolution of the experiment is deduced.

probe delays smaller than 2 ps, since the fit does not converge reliably for larger delays. This is caused by the limited coherence length of the electron pulses, which makes the (111) and (110) peaks overlap in the diffraction images. At short time delays, the background intensity and the intensity of the zero order and the (110) peak do not change significantly, such that the evolution of the (111) peak can still be retrieved. At larger delays, however, small shifts in the peak positions can not be distinguished from changes in the relative intensities of (111) and (110) peak. Further investigations with a higher spatial coherence or with differently oriented samples could resolve this issue.

The different evolution of the Bragg-peaks reflects the different mechanisms of energy-transfer from photoexcited electrons to the phonons. The excitation of phonons of the A_{1g} mode, which vibrate in the z-direction, is predominately observed in the respective (111) Bragg-peak. The decrease of the intensity of all other peaks is dominated by energy-transfer via incoherent electron-phonon scattering, on which the A_{1g} mode does not have a significant influence.

The incoherent energy-transfer is evaluated by analyzing the Bragg-peaks, excluding the (111) reflection. Similarly to the analysis of the aluminium data in section 4.1.3, the peaks are averaged in the form given by equation 3.9. A fit to this quantity with

a mono-exponential function yields a time-constant of (2.0 ± 0.1) ps. The solid lines in figure 4.11 a) are derived from this global fit. The good agreement of the data of all peaks with the fit shows that the incoherent energy-transfer is approximately isotropic and presumably couples to a broad range of lattice vibrations. Using tabulated Debye-Waller factors [Pen04], a temperature increase of (290 ± 9) K at long delay-times can be extracted from the data. Using values of the fluence, absorption of the multilayer sample and the static heat capacity of Sb, a heating of 380 K would be expected. The difference between the two values can be caused by various effects, e.g. by imperfect spatial overlap of the pump laser spot with the probe-pulses, decreasing the effective fluence on the sample. Heat transfer to the Si_3N_4 films is observed on longer delay times and is therefore excluded from causing the difference.

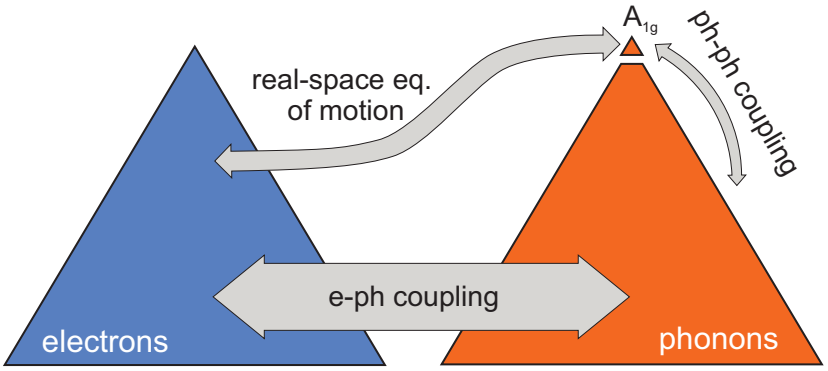

Figure 4.12.: Depiction of the model of the dynamics in antimony: The A_{1g} mode is separated from the description of all other phonon modes. It is included in a real-space equation of motion, the energy of which can be calculated classically. The lattice heating is described in a TTM, with a single electron-phonon coupling constant. The A_{1g} mode couples to the other lattice vibrations via phonon-phonon scattering and via the electronic subsystem.

The (111) peak is clearly not described by the incoherent and isotropic energy transfer. This is illustrated by the dotted line in figure 4.11 a), which is derived from the global fit to all other lattice peaks and shows its expected behavior in case there were no A_{1g} phonons excited. The measured amplitude is several times larger and the timescale on which it drops is significantly shorter. A zoom into the dynamics of the (111) peak within the first picosecond after photoexcitation is shown in figure 4.11 b). The shift of the minimum of the potential energy surface, which launches the A_{1g} mode, goes in hand with the electronic excitation, and therefore proceeds on the timescale of the exciting laser pulse. With a pump pulse duration of around 40 fs and a quarter of an oscillation period being 60 fs, the intensity of the peak is expected to drop within around 60 fs and then oscillate. The measured intensity of the peak decreases only

within few hundreds of femtoseconds, showing that the measured dynamics are limited by the time-resolution of the experiment. A fit of the peak with an error function yields a FWHM of the latter of (290 ± 30) fs, which constitutes an upper limit of the time-resolution of the measurement. Since electron-pulses are expected to have 100 fs duration at optimal conditions, the large time-constant might be caused by drifts in the laser-pointing, changing the temporal overlap over consecutive (but averaged) scans, a rotation of the sample of a few degrees (see chapter 2.1.1), broadened electron pulses due to the lowered voltage and an inhomogeneous excitation profile in the depth of the sample. It also explains the absence of oscillations in the (111) peak, as observed e.g. in x-ray diffraction experiments on bismuth [Fri07, Joh08], as they are smeared out in the measurement (see chapter 3.4).

4.2.4. Model of the dynamics

To describe the entire dynamics of electron- and phonon-distributions of photoexcited antimony, the classical two-temperature model is not suited, because the phonon distribution is in a clear non-thermal state, with the A_{1g} phonon mode being highly populated. Y. Giret *et al.* therefore suggested an expanded model which includes a classical real-space equation of motion for the A_{1g} mode in the coupled differential equations of the TTM [Gir11]. In this model, the equation of a driven and damped harmonic oscillator needs to be solved, and the resulting energy balance is afterwards included in the electronic and phononic subsystems. To calculate the intensity of a peak as a function of time, however, the contributions of the A_{1g} and the other phonons need to be separated again, retrieving back the TTM and the equation of motion of the harmonic oscillator. Here, the two problems will be treated completely separately, which is justified by comparing the energies in the different modes. Taking values of the frequency and the real-space amplitudes of the atom's motion and comparing it to the absorbed fluence as reported by H. Katsuki *et al.* [Kat13] (for bismuth), the energy in the A_{1g} mode is estimated to be 10^{-6} of the entire absorbed energy. A schematically representation of the model is shown in figure 4.12. The TTM is used as a first approximation to describe the dynamics of the incoherent energy-transfer, manifested in the evolution of all but the (111) Bragg-peaks. Solving the differential equation of a harmonic oscillator leads to the equation of motion of the A_{1g} phonon mode, which is treated as an independent mode from all other phonons. The decay of the A_{1g} mode proceeds via the coupling to electrons and via phonon-phonon coupling.

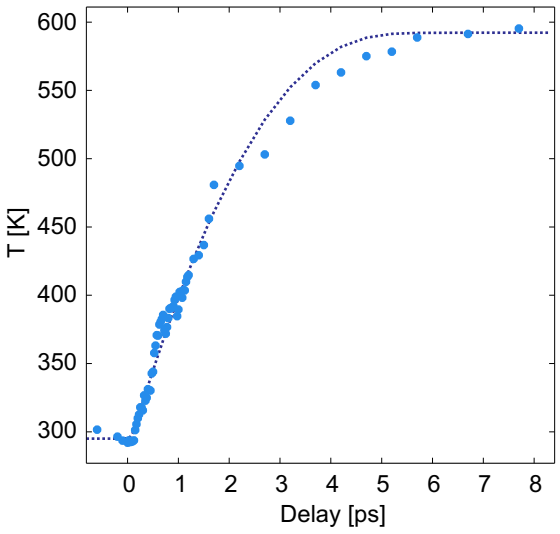

Figure 4.13.: Lattice temperature, calculated from the evolution of all but the (111) peak (diamonds) and fit of a two-temperature model (dotted line). The fit yields an electron-phonon coupling constant of $G_{ep} = 1.6 \cdot 10^{16}\,\mathrm{W/(m^3K)}$.

The real-space equation of motion of the A_{1g} mode is derived from the differential equation of a driven and damped harmonic oscillator. To solve those equations, the force on the atoms, given by

$$F(u(t)) = -\frac{v}{c}\left.\frac{\partial U_e}{\partial u}\right|_S, \tag{4.17}$$

needs to be known. Here, u is the phonon coordinate and $\partial U_e/\partial u|_S$ is the derivative of the electronic energy at constant entropy. This quantity could be calculated by DFT calculations [Gir11], but no value has so far been reported for antimony. The damping constant could potentially be retrieved from the electron diffraction measurements by the time constant with which the (111) Bragg-peak relaxes towards the value of a thermal state. Therefore, differently oriented samples or an increased coherence of the electron beam would be needed as described before.

Transient lattice temperatures were calculated from the evolution of the intensities of all but the (111) Bragg-peaks using tabulated Debye-Waller factors [Pen04]. A TTM was then fitted to the data as described in chapter 4.1.4 using an electron heat capacity factor of $\gamma = 0.119\,\mathrm{mJ/(molK^2)}$ [Ste83], where $C_e = \gamma \cdot T_e$, and a lattice heat capacity of $207\,\mathrm{J/(kgK)}$. The resulting fit is shown together with the data in figure 4.13. The value for the electron-phonon coupling factor resulting in the best fit was $G_{ep} = 1.6 \cdot 10^{16}\,\mathrm{W/(m^3K)}$ for the dataset shown. This value is more than one order

of magnitude smaller than the one of aluminium (see section 4.1.4), but is of similar magnitude as reported for bismuth [Gir11]. There, the reason for the much smaller electron-phonon coupling of bismuth in comparison to metals was attributed to the low density of states around the Fermi-level in bismuth, which presumably holds for antimony as well.

The model presented here assumes that the phonons (except the A_{1g} mode) are in equilibrium at all times. If the phonon-phonon coupling is much bigger than the electron-phonon coupling, this is a reasonable assumption, since an equilibrium of phonons can be established via phonon-phonon interactions, even if the coupling strength varies for different phonon branches. However, no literature values of the phonon-phonon coupling are available, but could be inferred from the measurements if the electron-phonon coupling strength would be calculated by DFT calculations, as shown in chapter 4.1.1. Increasing the spatial resolution in time-resolved electron diffraction experiments will allow to retrieve a reliable fit of the (111) peak over a larger range of delays and to infer the decay time of the A_{1g} phonon and therefore its coupling to all other phonons.

5. Crystalline to amorphous phase transition of $Ge_2Sb_2Te_5$

Phase change materials (PCMs) combine a unique set of properties which make them interesting to a wide variety of applications. Their functionality is based on the fact that, at room temperature, they exhibit long-lived metastable crystalline and amorphous phases with vastly different optical and electrical properties. Light or current pulses can be used to switch the material from one into the other state over a high number of cycles. The states of different resistivity and the ability to repeatedly switch the states of PCMs has been discovered in the early 1960's [Rao09, Ovs68]. Soon later, first patents were filed [Dew66] and PCMs were used as electronic data storage devices in the rare computers of that time. Today, they are still used in electronic data storage media, such as non-volatile flash memories [Lan05], but also in optical re-writable data storage, such as compact disks (CD), digital versatile disks (DVD) and Blu-ray disks. Their potential applications range from universal memories [Wut05] to flexible opto-electronic displays [Hos14], reconfigurable optical circuits [Rud13, Rio14] and logic devices [Lok14]. An introduction into history, properties and applications of phase change materials can be found in [Rao09].

The properties of phase change materials are found in many alloys of the ternary phase diagram of Ge, Sb and Te [Lan05, Len08], with a large number of PCMs lying on the GeTe - Sb_2Te_3 pseudobinary line. The compound $Ge_2Sb_2Te_5$ (GST) is a prominent compound of this line and is often considered to be a prototypical PCM. It has shown the fastest crystallization [Lok12] and amorphization rates [Lok14] measured to date and is therefore especially interesting for high-speed data storage applications.

The conventional pathway for amorphization is to heat the crystalline state above the melting point ($T_m = 615\,°C$ [Kol09]) and then rapidly quench the system to freeze in the disorder [Koh06]. However, in order to explain the speed of the amorphization in GST, alternative mechanisms have been proposed. Static measurements of the local atomic environment in the amorphous and crystalline phases have shown that the Ge ion's coordination changes from an octahedral surrounding in the crystalline phase to

a tetrahedral surrounding in the amorphous phase [Kol04]. This led to the proposal that, by optical excitation of a subset of bonds, the Ge ion's coordination would change through an 'umbrella flip' or 'ion-slingshot' transition, which would modify the lattice structure and optical properties on a 100 fs timescale [Kol04]. Similar conclusions have been drawn from time-resolved optical measurements on GeSb, where an ultrafast change in reflectivity [ST98], or the dielectric function [Cal01], were interpreted as an ultrafast phase transition to an amorphous or liquid state, respectively.

Amorphous GST is a semiconducting material with a bandgap of 0.6 - 0.9 eV and the crystalline (fcc) phase is a degenerate semi-conductor, therefore showing metallic properties like an enhanced DC conductivity [Rao09]. The optical contrast between the states for frequencies above the amorphous state bandgap has been explained in terms of resonant bonds in the crystalline state [Shp08, Hua10]. The concept of resonance bonds has been adapted from chemistry to solids by G. Lucovsky and R. M. White, who described a resonant bond as a many-body wave function, made from a linear combination of valence-bonds between atoms [Luc73]. In crystalline GST, half-filled p-type orbitals are aligned over next-nearest neighbor distances, such that bonds form, which can be modeled as resonant bonds, where the linear combination is done between the formation of a bond to one side of one atom and a bond to the other side. These extended bonds are rather delocalized and give rise to a large dipole matrix-element enhancement of the optical properties which is manifested in the large value of the real part of the dielectric function in the low energy (< 2 eV) region. The enhancement is lost when disorder between the next-nearest neighbors is introduced. This is the case for amorphous GST, despite the fact that the local bonding on the nearest-neighbor level remains relatively unchanged [Hua10, Car10].

The sensitivity of resonant bonds to bond alignment has also generated ideas for other non-thermal transformation pathways. Simulations have shown that distortions to a subset of bonds in the crystalline state of phase change materials can trigger a collapse to the amorphous state [Kol11]. As thermal heating affects all bonds, selective excitation of specific bonds could be a more efficient route to generate the amorphous phase, and it has been suggested that this may occur during the photo-driven phase transformation.

In this chapter, measurements of the evolution of optical and structural properties of GST are presented. Femtosecond optical spectroscopy is used to track changes in the dielectric function after photoexcitation. Whereas conventional Lock-in detection is used at reversible excitation conditions, a single-shot method using frequency encoding (see 2.2.3) is applied for fluences above the threshold for permanent amorphization, up to fluences leading to ablation. The response of the lattice is probed with femtosecond

electron diffraction below and above the threshold for phase change. The combination of the two methods allows for an unambiguous discrimination of electronically and structurally induced optical signals as well as for the investigation of the pathway of the photoinduced phase transition.

The optical measurements presented in this chapter were done in collaboration with S. Wall and T. Miller at the ICFO in Barcelona. The preparation and optical characterization of the samples has been done by T. Miller, M. Rudé, J. Osmond and V. Pruneri at the ICFO. Parts of this chapter have been published in [Wal15b].

5.1. Sample preparation and characterization

The $Ge_2Sb_2Te_5$ samples used in the experiments of this chapter have been prepared by RF co-sputtering from two stoichiometric targets of GeTe and Sb_2Te_3. The films were deposited on two different types of substrates. For the optical measurements, 30 nm of GST were deposited on 1 mm thick fused silica substrates (Corning Inc.) and protected with a 10 nm thick layer of Si_3N_4. Since thin, free-standing samples are required in the diffraction measurements (see chapter 2.1), for those experiments, the fused silica substrate was replaced by a second Si_3N_4 membrane of 10 nm thickness. The latter samples were first deposited on a polished NaCl crystal, which was later removed by floating the thin films on water to dissolve the NaCl. The films were then transferred onto large area silicon grids, which are described in 2.1.

The as-deposited samples of GST were heated to different temperatures and their state was characterized by optical and Raman measurements, or by optical measurements and static diffraction images, respectively. Homogeneous crystallization of the GST films was achieved by heating the samples to 200 °C for 1 h or more. Figure 5.1 shows the dielectric function of three different thermally prepared states of the GST samples, which were measured by ellipsometry. The values for the dielectric function reported here differ from those by Shportko *et al.* [Shp08] by a shift of the features of around 1 eV, but match the values reported in [Rao09, Par09] closely. The energy dependence of the dielectric function, however, shows the same trend in all cited works, with shifts occurring on the energy axis. The variation in the measured values reported here and the literature values may be caused by small variations in composition and by the preparation conditions, such as partial gas pressures or temperature gradients, in which the samples are grown (see e.g. [Kim98, Ols06, Rao09]). Additionally, the substrate and capping layer can induce strain, resulting in slightly different values to samples on different substrates.

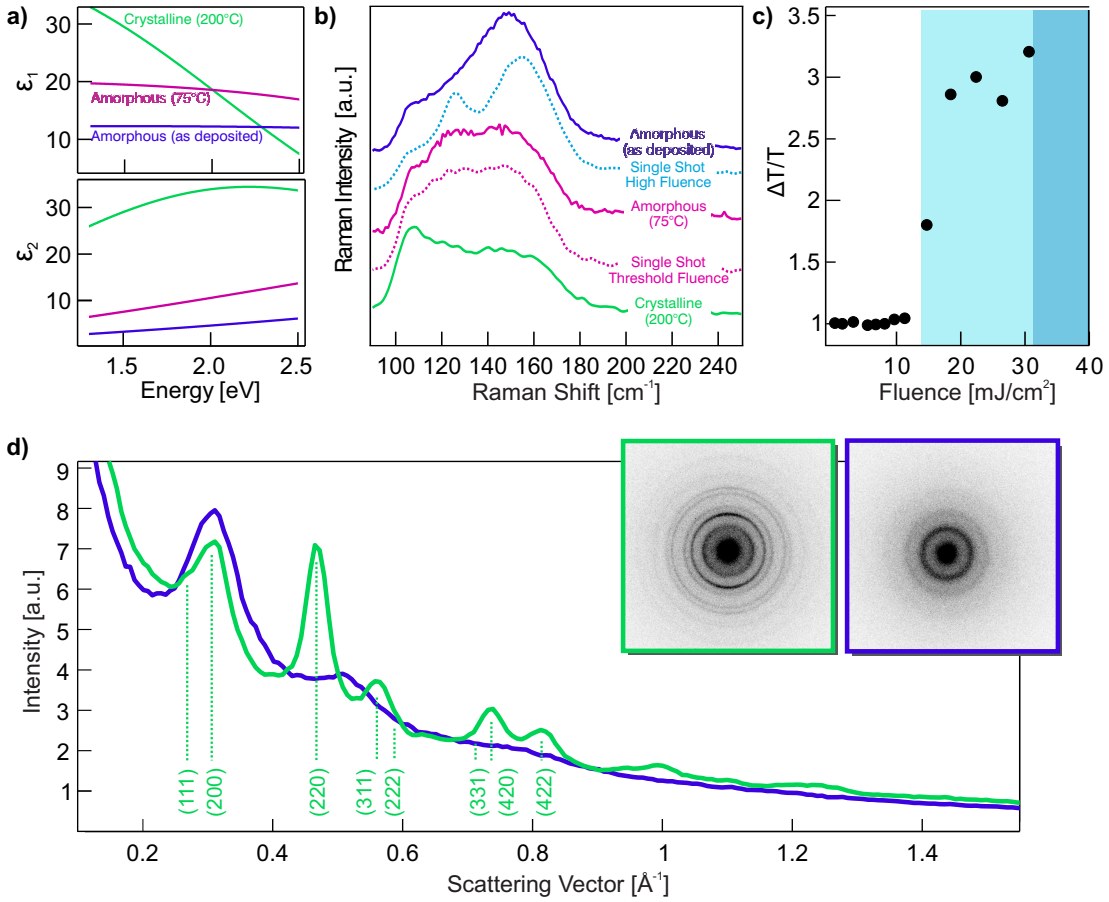

Figure 5.1.: Properties of amorphous and crystalline GST. **a)** Measured real and imaginary parts of the dielectric function of amorphous and crystalline GST. **b)** Raman spectra of as deposited, annealed amorphous and crystallized GST (solid lines), together with spectra recorded after single fs-pulsed laser excitation of the crystalline state (dashed lines). **c)** Permanent change in optical transmission after exposure of crystalline GST to single femtosecond laser pulses. A threshold of $14\,\mathrm{mJ/cm^2}$ is observed. Ablation occurs for fluences above $32\,\mathrm{mJ/cm^2}$. Each point is recorded on a fresh part of the crystalline sample. **d)** Radial averages of amorphous (blue) and crystalline (green) samples of GST (raw images in the inlet). Some Bragg reflections of the crystalline phase are indexed.

Figure 5.1 b) shows Raman spectra of the different states of GST, which are in excellent agreement with reported spectra [Něm09, Hsi13, And07]. The spectrum obtained after exciting an initially crystalline sample with a fluence just above the phase transformation threshold matches those of annealed (75 °C) amorphous samples, whereas regions excited with a higher fluence show features of the as-deposited phase spectra.

This indicates that the local bonding strongly depends on the temperature reached after excitation, even though long-range order is lost in both cases.

The permanent change in the optical transmission of a crystalline film induced by single sub-40 fs laser pulses with 1.5 eV photon energy is shown in figure 5.1 c). Above a threshold fluence, the sample switches to the amorphous state, demonstrated by the strong and permanent change in optical properties. Amorphization occurs at an incident threshold fluence of approximately $F_{th} = 14\,\mathrm{mJ/cm^2}$ which, in the linear absorption regime, corresponds to approximately 1 absorbed photon per unit cell of the cubic phase. Ablation was observed for fluences exceeding $32\,\mathrm{mJ/cm^2}$, but cracks in the film can already for fluences slightly below this threshold.

In figure 5.1 d), static diffraction images and radial averages of as-deposited and annealed free-standing films of GST are shown. The amorphous state has been described as consisting of disordered atomic ring-like structures [Hua10, Lan07], which leads to broad features in the diffraction image (inlet, blue frame). Heating of the samples prior to the transfer of the grid to the vacuum chamber, as well as heating by consecutive laser-pulses, leads to crystallization and the establishment of long-range order. This can be seen by the appearance of sharp diffraction rings in the diffraction images (inlet, green frame). Radial averages were calculated from the diffraction images as described in appendix A. Several Bragg-peaks used for the analysis are labeled in the figure.

5.2. Optical and structural dynamics in the reversible regime

The dynamics of the crystalline phase for excitation fluences below the threshold for permanent amorphization F_{th} were studied by femtosecond optical spectroscopy and femtosecond electron diffraction, both of which are described in detail in chapter 2. The optical measurements were performed with a different Ti:Sa amplified laser system as the one used in the diffraction experiments, but with a similar temporal and spectral pulse profile. In both measurements, the repetition rates of the lasers were reduced for the higher fluences to avoid accumulate heating of the samples. The lowest repetition rate was 40 Hz in the optical, and 80 Hz in the diffraction measurements. The optical measurements presented in this section were performed by T. Miller and S. Wall at the ICFO Barcelona.

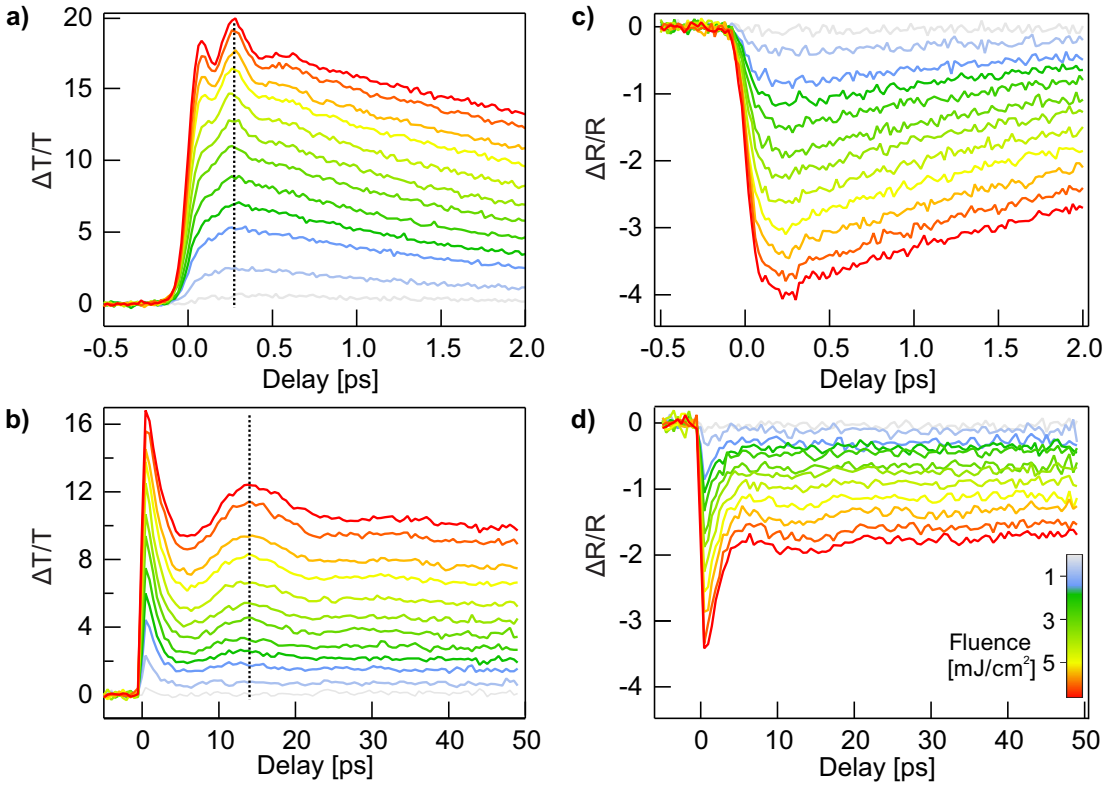

Figure 5.2.: **a)** & **b)** Evolution of the relative transmission $\Delta T/T$ of GST after photoexcitation with a femtosecond laser pulse. The dotted lines show the position of the maximum of the coherent optical phonons (in a)) and the acoustic film breathing mode (b)). **c)** & **d)** Evolution of the relative reflectivity $\Delta R/R$.

5.2.1. Dynamics of the dielectric function

In order to be able to qualitatively interpret all-optical measurements, it is necessary to transfer the typically measured reflectivity or transmissivity, as they also depend on the measurement geometry, into a material-specific quantity, e.g. the dielectric function (see chapter 2.2). Here, the dynamics of the dielectric function were obtained by simultaneously measuring the transient reflectivity and the transmission with a Lock-In amplifier. The two quantities together were then converted to ϵ_1 and ϵ_2, as described in chapter 2.2.2. The raw data of $\Delta T/T$ and $\Delta R/R$ is shown in figure 5.2 a) - d). Whereas the interpretation of the data in the form of the dielectric function is given in the next paragraph, the signatures of coherent phonons can already be seen in the raw data of the transient transmission in a). The Fourier-transform of the oscillation matches the Raman spectrum of the crystalline phase (see figure 5.3 and description in the next paragraph). In b) and d), which show the dynamics on a longer time-scale,

a second oscillation is visible with a period T of slightly more than 20 ps. With the speed of sound being v_s =3.2 nm/ps [Lye06] and the film thickness d = 30 nm, this oscillation corresponds to the breathing motion of the film with a period of $T = 2d/v_s$. The position of the maxima of the oscillations are displayed by the dashed lines in a) and b). The position of the maxima does not shift, indicating that the frequencies do not shift with excitation fluence.

Figure 5.3 a) and b) show the evolution of the dielectric function of GST after photoexcitation for different excitation fluences, calculated from the transient reflectivity and transmission (shown in figure 5.2) by inversion of the transfer matrix formalism presented in chapter 2.2.1. It can be seen that photoexcitation induces in both, real and imaginary parts of the dielectric function, an instantaneous decrease within the temporal resolution of the experiment. For increasing excitation fluence, this amplitude is observed to increase linearly with fluence. The initial fast drop is followed by a recovery of real and imaginary part, which can be well fitted with an exponential function. The fit of a step-like drop and an exponential recovery, convoluted with a Gaussian function, is shown in figure 5.3 c). The remaining oscillation, which is only observed in ϵ_2, whereas no sign of it can be seen in ϵ_1, is caused by coherent phonons, the frequency spectrum of which corresponds well to the Raman-spectrum, shown in d). The time-constant is found to increase with increasing fluence. However, for each investigated fluence it is the same for ϵ_1 and ϵ_2.

Optical excitation at 800 nm excites electrons within the GST film. The enhanced free-carrier density increases the plasma frequency, which usually decreases ϵ_1 and increases ϵ_2 by small amounts when probing at 800 nm [Hua98]. However, the optical response of the crystalline phase shows a large decrease in both ϵ_1 *and* ϵ_2, which can thus not be attributed to the increase in free carriers alone. Instead, the effect is attributed to a photo-bleaching of resonantly bonded states, as the primary effect resulting from the loss of resonant bonding is a large decrease in both parts of the dielectric function [Shp08]. As the Raman-active optical phonon modes are only observed in ϵ_2 and not in ϵ_1, it can be concluded that they do not significantly influence the resonantly bonded states.

5.2.2. Dynamics of the lattice

The dynamics of the crystalline lattice were investigated by recording diffraction images at different pump-probe delays with the setup described in chapter 2.1. Diffraction images were taken with an exposure time of 5 s, and around 10 experimental runs were averaged for each fluence. Diffraction images taken at negative time-delay were com-

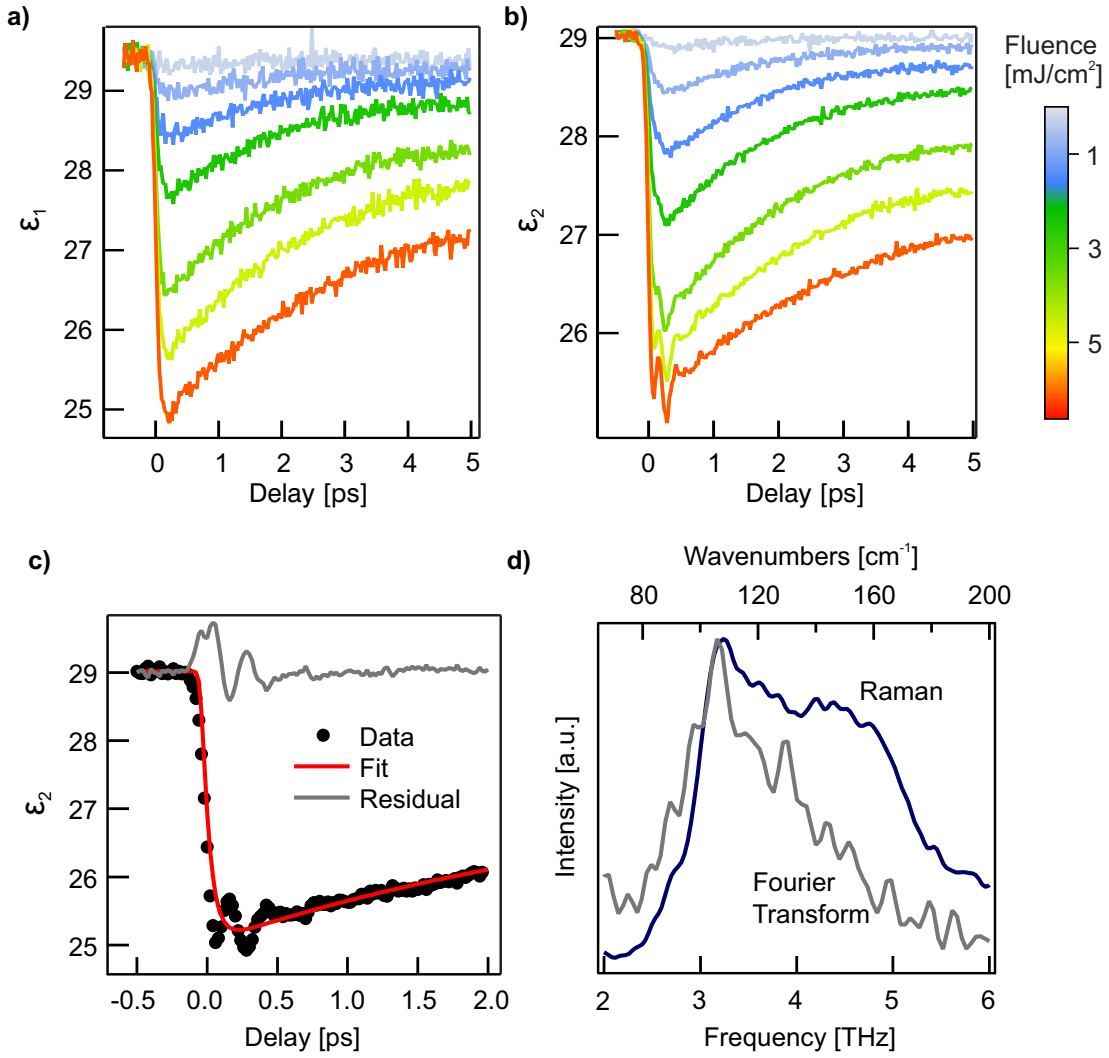

Figure 5.3.: **a)** & **b)** Dynamics of real and imaginary parts of the dielectric function at 1.55 eV for different excitation fluences. The amplitude of the quasi-immediate drop scales linearly with excitation fluence. **c)** Fit of the dynamics with exponential functions and residual of the fit, containing the motion of a coherent phonon. **d** Fourier spectrum of the phonon mode from c), matching the phonon spectrum obtained from Raman-spectroscopy.

pared to images without pump-pulses and the repetition rate of the laser was adjusted, such that no temperature offsets before time zero due to consecutive pump-pulses could be detected. The repetition rate was reduced by mechanically chopping the laser path. For the highest fluences, the repetition rate was reduced to 80 Hz.

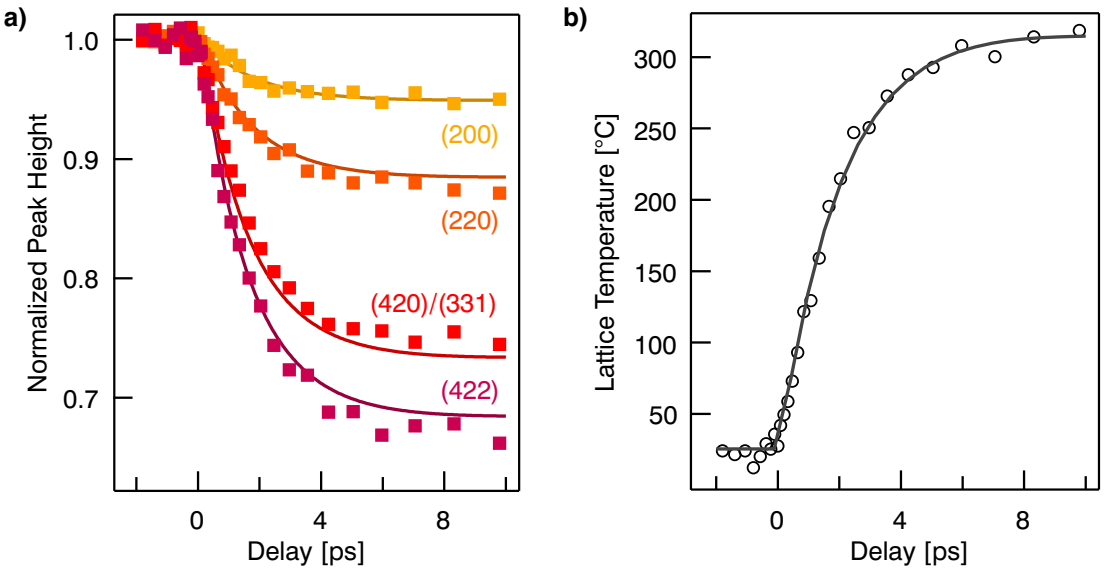

Figure 5.4.: a) Evolution of several diffraction peaks after excitation with a fluence of 5.8 mJ/cm^2. The solid lines are calculated from the fit of an exponential rise of temperature as shown in b). **b)** Lattice temperature, calculated from all diffraction peaks assuming thermal phonon distributions at all times. The solid line is a monoexponential to the temperature.

In figure 5.4 a), the temporal evolution of the intensity of four Bragg peaks (a diffraction pattern is shown in figure 5.1) at an excitation fluence of $F = 5.8\,\mathrm{mJ/cm^2}$ is plotted. The amplitudes of all peaks decrease after $t = 0$ and reach a new value around 8 ps. A comparison of the evolution of the peaks in the form given by equation 3.9 ($\ln(I_{\mathrm{rel},s})/s^2$) shows that the traces of all peaks fall well on top of each other. This indicates that their decrease is governed by the same physical process, leading to an isotropic increase in mean square displacement of the atoms and no strongly coupled modes (see the work on antimony in chapter 4.2) are observed in the diffraction data. This is in line with the optical measurements, which only show a weak sign of coherently excited phonons, which, in addition, are strongly damped.

To quantitatively describe the temporal evolution of the lattice vibrations, the data of all peaks is averaged in the form of equation 3.9. Assuming thermal phonon distributions at all delay times in a first approximation, a lattice temperature can be calculated from this averaged quantity by using Debye-Waller B-factors from [Car10] (see also chapter 3). Non-thermal but isotropic phonon distributions, as observed in aluminium (chapter 4.1), might transiently be excited. A systematic error of the time-constant caused by the assumption of a thermal distribution is therefore possible, but

only of secondary interest here, as the dynamics of optical properties and lattice heating are qualitatively distinct.

The lattice temperature, calculated from the evolution of the Bragg peaks, is shown in figure 5.4 b). Using an exponential function to fit the temporal evolution of the temperature, the data is nicely reproduced for a timeconstant of 2.2 ps (solid line in the figure). The details of the fit are given in section 5.4, where the long-term dynamics of the material are discussed.

The solid lines in figure 5.4 a) are the calculated response of the individual diffraction peaks from the fitted lattice temperature. It can be seen that they reproduce the evolution of each peak well, underlining again that the energy-transfer is isotropic. Together with the observation from the optical measurements that the phonon frequencies do not change with excitation level, this implies that electronic excitation does not significantly change the lattice potential of the ions and the energy transfer from electrons to phonons proceeds via incoherent scattering processes.

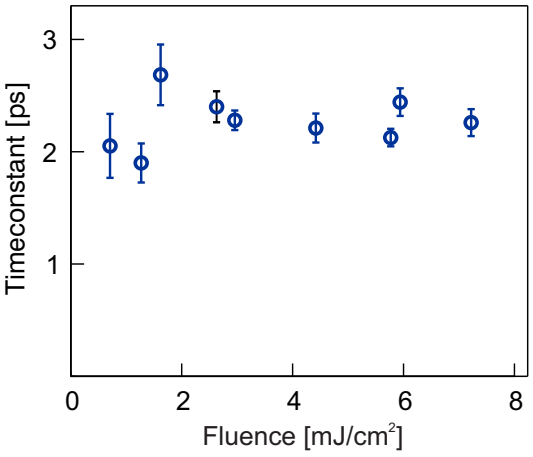

Figure 5.5.: Timeconstant of a single-exponential fit to the dynamics of the lattice heating for different excitation fluences. Within the errorbars of the experiment, the timeconstant is constant over the entire investigated range of fluences.

The dynamics of the lattice heating were studied as a function of excitation fluence. The highest fluence for which no long-time changes of the sample were observed was 7.5 mJ/cm^2. The same type of data-analysis was applied to all measurements to retrieve a lattice temperature as a function of time. The lattice temperature is fitted and the timeconstant of the heating is plotted against excitation fluence in figure 5.5. Within the errorbars of the experiment, the timeconstant of the lattice heating does not change within the range of investigated fluences. Even for the highest fluences, no deviation from the isotropic energy transfer is observed.

5.3. Pathway of the photoinduced amorphization

In this section, the dynamics of GST are described, when the excitation fluence is increased above the single-shot transformation threshold F_{th}. In this regime of irreversible excitation, conventional pump-probe techniques, averaging over many pump-probe cycles, are not able to study the dynamics any more, and alternative approaches are needed. The optical measurements presented in this section were conducted with frequency-domain single-shot spectroscopy (FDSS), which uses chirped probe pulses to map the optical response of a material onto the spectrum of a single probe pulse. An introduction to this technique, as well as technical details, are given in chapter 2.2.3. The diffraction experiments were done by recording diffraction patterns from a single electron pulse as a probe of the structural state of the material. Therefore, modifications to the electron diffraction setup were made, which are described in chapter 2.1.4. In both techniques, the samples were shifted to a new spot after each pump-probe cycle, as single pump-pulses induced irreversible changes to the sample.

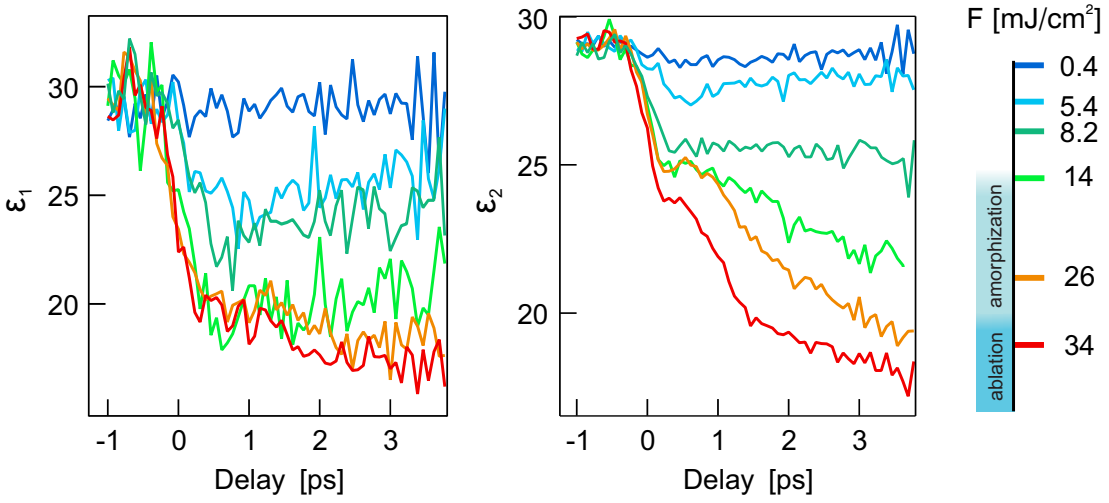

Figure 5.6.: Dynamics of the dielectric function for different fluences (subset of the data) below and above the threshold for permanent amorphization. Below threshold ($F_{th} < 14\,\mathrm{mJ/cm^2}$), the measurements show the same response as the data measured with the conventional Lock-In technique (see figure 5.3). Above threshold, ϵ_1 saturates, but ϵ_2 shows a further slow dynamic. Increasing the fluence of the pump pulse to the ablation threshold ($F > 32\,\mathrm{mJ/cm^2}$) does not cause a significant change in either of the dynamics.

The FDSS method allows to map out approximately 5 ps of dynamics of the optical properties, induced by a single laser pump pulse, with a time resolution of a few hundred femtoseconds. By measuring the dynamics of reflected and transmitted intensities in parallel, the transfer-matrix formalism can again be used to transfer the measured intensities into changes in the dielectric function (see 2.2.1). Figure 5.6 shows the dynamics of the dielectric function of GST for a range of fluences that covers reversible, amorphization and even ablation regimes. At low powers, the FDSS technique reproduces the changes observed in the dielectric function measured with the standard Lock-In technique, i.e. an initial fast drop and a recovery of the signal towards its initial value during a few picoseconds. The amplitude of the initial drop of ϵ_1 increases on increasing excitation density until the pump fluence reaches the threshold value F_{th}. At this point ϵ_1 has decreased by 30% within approximately 100 fs and does not increase by further increasing the pump fluence. Remarkably, the value of ϵ_1, reached immediately after photoexcitation, saturates at the value observed in the quenched amorphous state, as can be seen in figure 5.7. This suggests that resonant bonds are completely depopulated at this point. Furthermore, ϵ_1 does not show any significant temporal evolution on the 3 ps timescale measured. The value of ϵ_2 at short time delays (500 fs) also saturates when crossing the threshold fluence, but at a value that is far from the one of the amorphous phase. Unlike ϵ_1, however, it continues to evolve in time and large changes occur on a slower timescale of several picoseconds.

The ultrafast saturation in ϵ_1 to the amorphous phase value suggests that the population of electrons in resonant bonds has been completely diminished on a sub-picosecond timescale, as would be expected in the case a non-thermal phase transition occurred. Electron diffraction measurements above F_{th}, however, reveal that the lattice responds on a slower timescale. Figure 5.8 a) shows radial averages for different pump-probe delays at an excitation fluence of 22 mJ/cm^2. Each radial average is an average of 10-15 diffraction patterns, each taken with a single electron pulse. The existence of Bragg peaks in the radial averages indicates that the crystalline structure persists for several picoseconds after photoexcitation. The complete loss of long-range order is observed only after approximately 5-10 ps. Figure 5.8 b) shows the temporal evolution of the fitted intensity of the (220) peak for three different excitation densities. The dataset with the excitation fluence of 6 mJ/cm^2 was measured with the standard diffraction technique, averaging over several thousands of shots and the relative decrease was scaled by a factor of two for better comparison. The solid lines are fits to the data using the same exponential decay model with a timeconstant of 2.2 ps used to fit the below-threshold electron diffraction data in section 5.2.2. The good agreement of fit and data implies that the above threshold dynamics are still described by the same physical process as

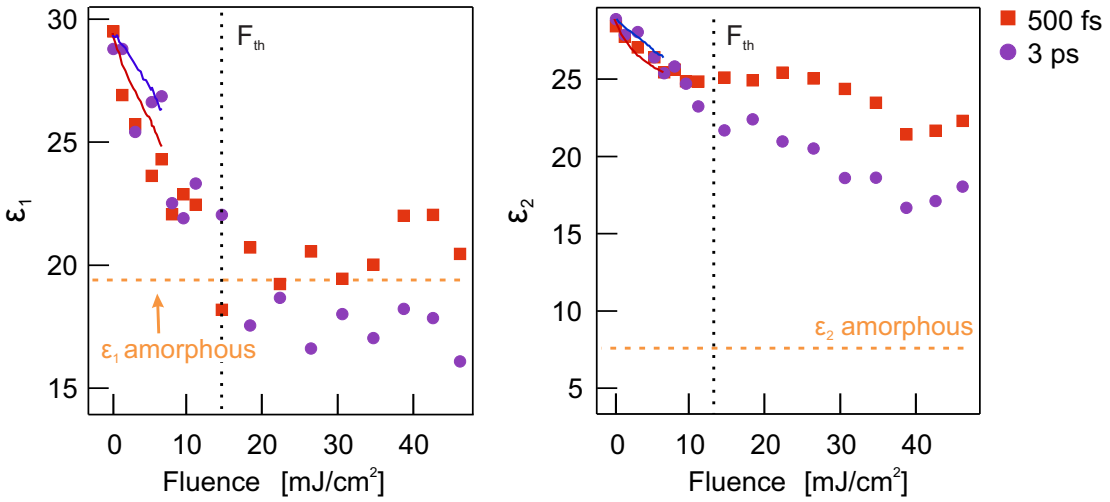

Figure 5.7.: Dependence of the changes in the dielectric function with excitation strength at two time delays. Excellent agreement is found with the low fluence data (solid lines). ϵ_1 saturates with increasing pump fluence to the value observed in the amorphous phase (horizontal dashed line). This occurs at the same fluence which permanently amorphizes the sample (vertical dotted line). The saturation of the value of ϵ_1 is also seen at delay times of 3 ps. ϵ_2 saturates at short time delays to a value that is far from the amorphous value. At longer time delays, further dynamics are observed and the changes in ϵ_2 further increase.

below threshold, i.e. the lattice heats by incoherent electron-phonon collisions rather than an electronically induced change in lattice potential.

Figure 5.8 c) shows the lattice temperatures at long delay times (10 ps) after photoexcitation as a function of pump fluence, obtained from the fits to the below threshold data. A linear dependence of this temperature with fluence is found. Extrapolating the temperature at 10 ps to the threshold fluence shows that the expected temperature at the fluence F_{th} is in good agreement with the temperature required to melt the sample [Kol09]. Even though the signal-to-noise ratio of the single-shot diffraction data does not allow a direct distinction of the radial averages of liquid and amorphous GST, the loss of long-range order, as seen in figure 5.8, can therefore be attributed to thermal melting.

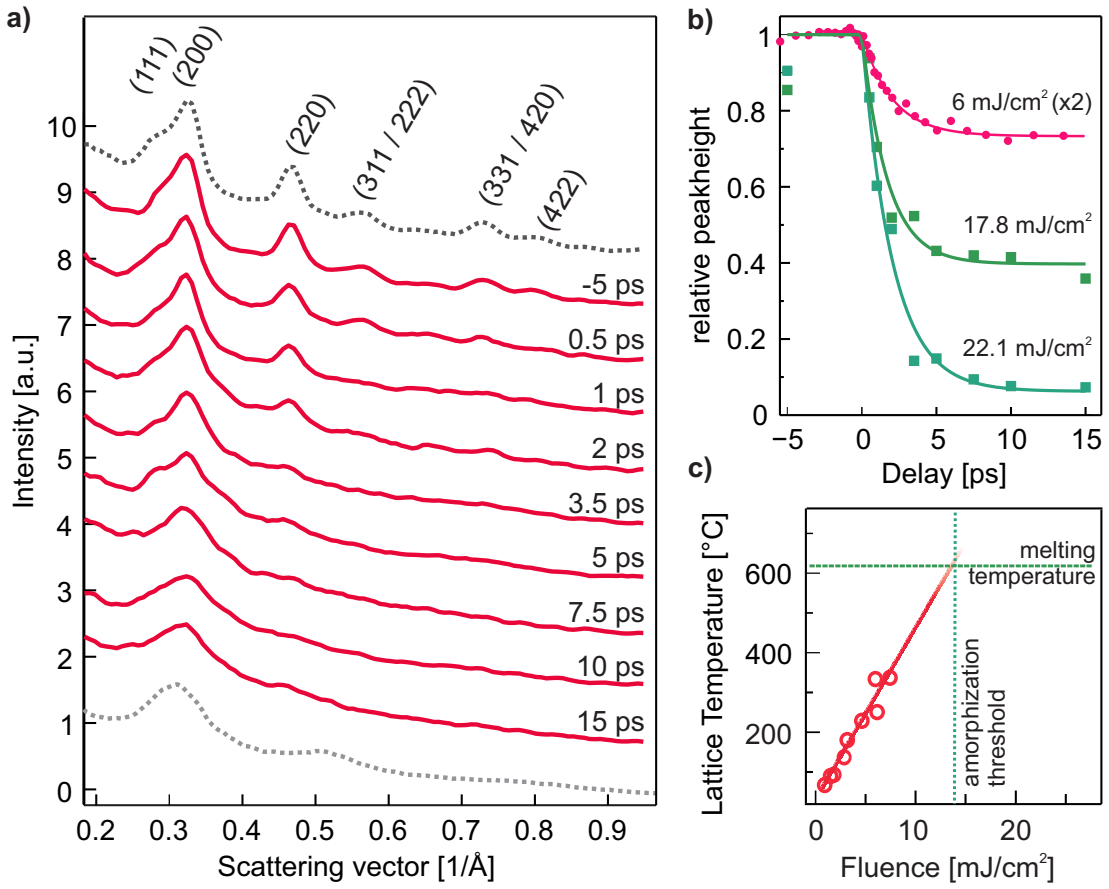

Figure 5.8.: **a)** Radially integrated diffraction pattern measured in the single shot regime for a pump fluence of 22 mJ/cm^2 at several time delays. The Bragg peaks are labeled, with multiple labels indicating that diffraction orders overlap. Long-range order, indicated by the existence of Bragg-peaks, is lost by approximately 5-10 ps. **b)** Fitted peak height of the (220) diffraction peak, for two fluences above threshold, together with a time trace measured in the reversible regime (change scaled by a factor 2 for better comparison) . The same time constant of 2.2 ps can be used to fit the below and the above threshold data. **c)** Sample temperature at long delay times after laser excitation. Linear extrapolation of the temperature to above threshold fluences shows that amorphization occurs as soon as the melting point of the sample is reached.

5.4. Long-term dynamics: influence of the substrate

In the preceding discussion, the influence of the substrate on the dynamics of photoexcited GST has been omitted, since the signatures of vibrational coupling between

GST and the substrate are only observed on longer delay times. Here, the dynamics of GST on timescales up to 100 picoseconds are discussed. In addition, the final states of GST (several seconds after the pump laser pulse initiating the state transformation) are investigated by optical and static (no pump pulses) diffraction images.

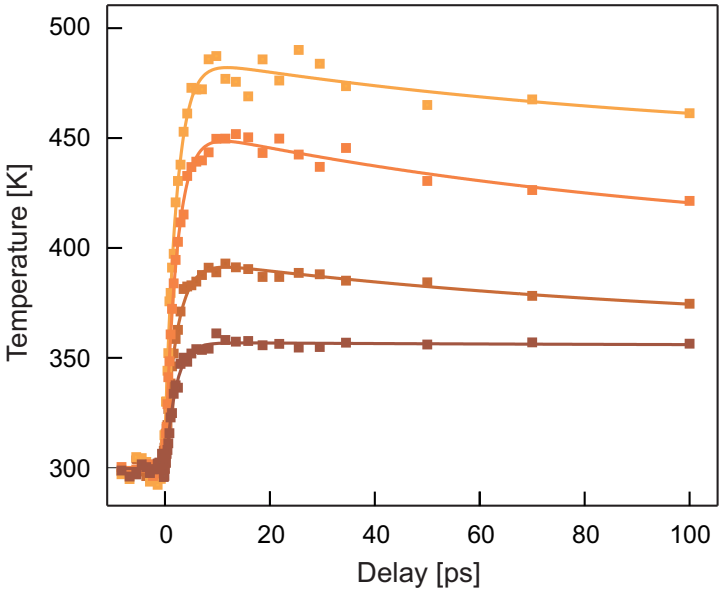

Figure 5.9.: Evolution of the lattice temperature of the GST sample for delays up to 100 ps and for four different excitation fluences. The decrease in lattice temperature is caused by thermalization with the Si_3N_4 capping layers, which do not absorb in the spectral region of the pump laser pulses.

Figure 5.9 shows the evolution of the retrieved lattice temperature for four different excitation densities and delay times up to 100 ps. The data is taken from the same measurements as in section 5.2, where only the initial dynamics have been discussed. Whereas the increase of lattice temperature in the first 10 ps can be well described by a single exponential increase, a clear decrease of lattice temperature on a longer timescale is observed. The lattice temperature over the entire measurement range can be fit by the sum of two exponential functions

$$T(t) = A_1(1 - \exp(-t/\tau_1)) - A_2(1 - \exp(-t/\tau_2)), t > 0, \tag{5.1}$$

where A_i are the temperature amplitudes of the rise and the decay and τ_i the time-constants. It has been shown in the previous sections that thermalization of photoexcited electrons and the lattice leads to an increase in lattice temperature on a 2 ps timescale, which is described by the first amplitude, A_1. A thermalized state is reached within 10 ps, as evidenced by the quasi-stationary diffraction pattern. However, with

the capping layer and the substrate being transparent to the pump-laser wavelength, it is expected that the GST film is still in non-equilibrium with the substrate. The second amplitude of the fit can therefore be attributed to an energy flow from the GST layer to the substrate via vibrational coupling between them. This is supported by a comparison of the amplitudes A_1 and A_2. The temperature reached at long timescales (several hundreds of picoseconds) is fitted to be (on average) 70% of the temperature reached at 10 ps. Considering the thickness and heat capacity of Si_3N_4 and $Ge_2Sb_2Te_5$, a temperature of 50% of the maximum would be expected for long time delays, which is in reasonable agreement with the fitted values.

From geometrical considerations, heat diffusion in lateral direction of the films and into the underlying grid is expected to be many orders of magnitude slower. This is evidenced by static heating induced by consecutive laser shots, which is observed for high repetition rates. To return to the initial state, a time of one to several tens of ms has been found.

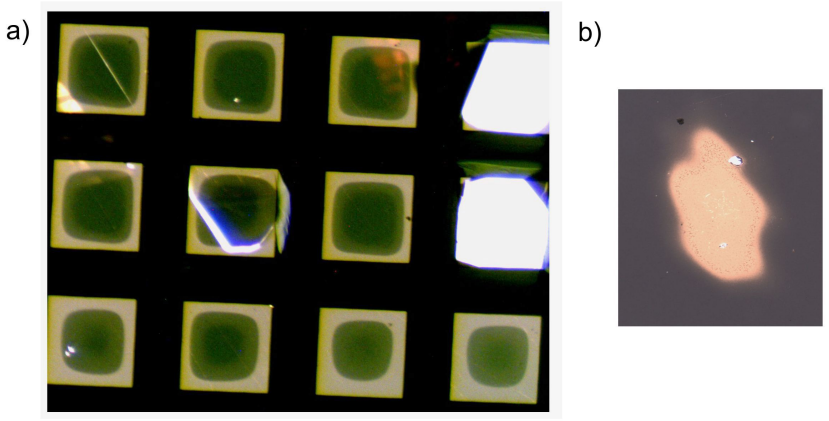

Figure 5.10.: Microscope transmission images of GST films after irradiation with a single laser pulse of $F > F_{th}$. **a)** Free standing films on a silicon grid. The outer regions are amorphous, whereas the central part, in which heat was trapped the longest, re-crystallized. The even darker center in some squares corresponds to the hexagonal phase of GST. **b)** GST on glass slide. The entire area within the pump laser spot amorphized.

A significant difference in heat diffusion into the glass substrate and the Si_3N_4 is expected, since their thicknesses differ by 5 orders of magnitude. Whereas heat has to diffuse laterally in the thin films, it can also diffuse into the depth of the glass substrate. Assuming a similar vibrational coupling from GST to the two substrates, it is estimated that the GST on glass cools down to close to its initial temperature within 1 ns. The difference in cooling speed manifests itself in the final state reached at

quasi-infinite delays: whereas crystalline GST on glass amorphizes, the free-standing GST films amorphize in regions close to the silicon grid, but stay crystalline in areas further away, in which the heat is trapped for longer times. At sufficient fluences (and thus temperatures), the emergence of a different crystalline phase is observed, which is attributed to a previously described hexagonal phase of GST [Fri00]. Laser-induced optical changes of the different samples can be seen in the microscope images presented in figure 5.10. In a), a microscope image of the free-standing films of GST is shown. Three regions of different absorption can be recognized, the darkest one corresponding to the hexagonal phase. In b), an amorphized spot of GST caused by a single pump laser pulse is shown.

5.5. Transient decoupling of optical contrast and lattice structure

Combining the information from the measurements of the time-dependent dielectric function and the lattice dynamics presented in the preceding sections allows to build a detailed picture describing the first steps of the amorphization process of crystalline GST. A schematical drawing is shown in figure 5.11. Femtosecond optical excitation directly removes electrons from resonantly bonded states as evidenced by the immediate decrease in the dielectric function and the saturation of ϵ_1 at the value of the amorphous state. This immediate change in the optical properties does not coincide with a change in crystallinity and thus represents a previously unobserved transient state of GST. No evidence of non-thermal lattice dynamics are observed even for the highest investigated fluences, as they have been found in other materials [Lin05, Har08, Sci09]. Thus, the depopulation of resonant bonds does not significantly effect the potential energy surface of the atoms, which is consistent with the view of a covalently bonded backbone of the crystalline lattice [Kol11].

The transient state is lost by energy transfer from excited electrons to the lattice, which occurs with a 2.2 ps timescale and leads to a thermal state with elevated temperature within 5-10 picoseconds. The further evolution of the system is dictated by the thermal properties of the sample and the substrate, as evidenced by the different final states of the samples on different substrates and the time-constant for equilibration of sample and substrate. Amorphization occurs on long timescales if the heat can be efficiently removed, but insulated samples can also re-crystallize.

The observed decoupling of the optical properties from the structure on ultrashort timescales reveals the potential to induce large and fully reversible changes in the

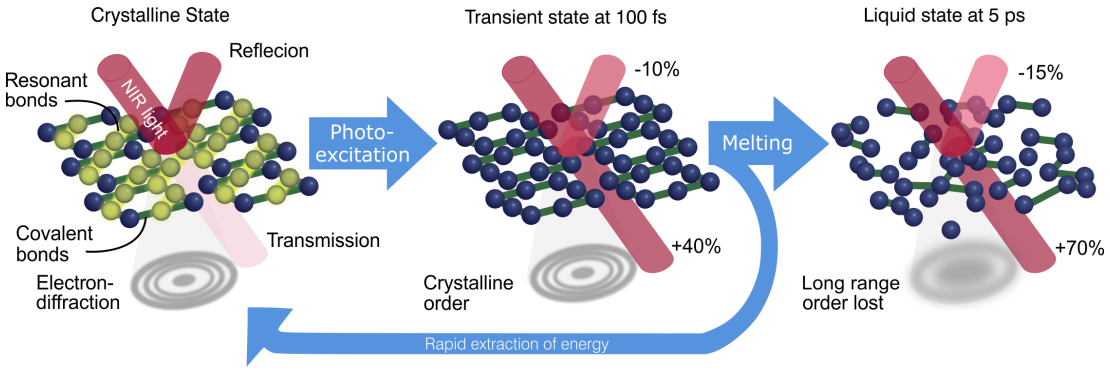

Figure 5.11.: Depiction of the transformation pathway of GST. Crystalline GST exhibits resonant bonds, which have large influence on the optical properties. Femtosecond photoexcitation removes electrons from the resonant bonds and creates a new transient state with big changes in the optical properties and an unchanged lattice. Thermal melting occurs on a few picosecond timescale and the amorphous state is reached after heat has been removed into the substrate and the surrounding. Rapid cooling or carrier extraction could prevent melting and enable the restoration of the resonantly bonded state.

optical properties without significant atomic motion or without inducing a phase transformation. Modulations of the dielectric function on the sub-100 fs timescale of up to 13% are observed, which is over an order of magnitude larger than reported for silicon photo-switches [Kam10]. Improved thermal conductivity and active cooling of the substrates could allow to induce even larger changes without state transformation. The large amplitude of transient changes of the dielectric function might extend into the region of telecommunication wavelengths, as the infrared spectral region has an even greater sensitivity to changes in resonant bonding (see figure 5.1 a)).

A permanent amorphization of the material is needed to stabilize the changes in optical properties over a long time, as needed in data storage applications. However, the ability to harness the ultrafast optical contrast of GST and other phase change materials without a structural transition suggests a new avenue to high-speed optical devices such as all-optical modulators for communications and computations.

6. Electron-lattice coupling in semiconducting transition metal dichalcogenides

Two-dimensional materials exhibit a wealth of fascinating properties, both for fundamental research and as building blocks for future nanoscale devices [Nov12, Wan12]. First experiments were done by K. Novoselov, A. Geim *et al.* on atomically thin, isolated carbon films [Nov04], also named graphene [Boe62, Boe94]. Their experiments triggered tremendous research activities on the properties, preparation procedures and potential applications of graphene as well as on two-dimensional materials in general. It was found that graphene possesses a superb mechanical strength [Lee08], an unusual electronic structure [Nov05a], a very high carrier mobility [Bol08] and an impermeability to gases including helium [Bun08]. Soon, it was widely discussed for being used in many novel applications, including electronic computational devices reaching the ultimate size limit in which the active element consists of a single layer of atoms [Sch10]. However, many electronic applications, such as transistors, are based on modulating electronic properties, e.g. the carrier mobility, which in graphene is hardly possible due to the lack of a bandgap around the Fermi-energy E_F [Nov12]. Whereas doping can change the Fermi-level, the general problem would be overcome by two-dimensional semiconducting materials which possess a sizable bandgap.

The most promising materials are transition metal dichalcogenides (TMDCs), which have the chemical composition MX_2 (M: transition metals, X: chalcogen). Here, the discussion will be restricted to the compounds made from M = Mo, W and X = S, Se, as they are semiconducting and share a set of common properties [Wan12]. They exhibit a layered structure and were found to be producible in stable atomically thin sheets, which was first demonstrated for MoS_2 [Nov05b]. Their bandgaps undergo a transition from indirect to direct when reducing the number of layers to one [Mak10, Chh13, Xu13, Jin13]. The size of the bandgap of the atomically thin versions are comparable to the ones of bulk silicon or germanium [Din11, Ram11], which allows to

transfer design-concepts of the established semi-conducting technology. At the same time, TMDCs exhibit unusually strong excitonic features in their photoluminescence and absorption spectra [Fri63, Qiu13, Bec15], as well as a large spin-splitting of the valence bands [Jon14], which might be used in photonics or opto-electronic devices [He14] or in 'spintronic' applications [Mak12, Gon13].

Time-resolved experiments can contribute in understanding some of the fundamental properties of two-dimensional TMDCs by exploring the real-time evolution of electronic- and vibrational distributions and visualize the underlying interaction mechanisms. Specifically, the coupling of excitonic- or spin-polarized electronic excitations to other electronic states and to lattice vibrations, as well as energy dissipation and transport mechanisms can be addressed. Anisotropic contributions in the coupling mechanisms, which can be expected due to the strong anisotropy of the lattice structure, might be identified and are of general interest. By following the energy transfer between layers of different materials, the vibrational coupling in between layers can be disentangled from intra-layer processes, which might be specifically important for the exploitation of TMDCs in electronic or opto-electronic devices, consisting of heterostructures of different two-dimensional materials [Gei13].

In this chapter, the coupling of differently prepared electronic excitations to lattice vibrations of WSe_2 are studied. By using laser pulses with photon energies close to the excitonic resonances, electronically excited states with a narrow distribution in k-space are prepared. The following relaxation dynamics, specifically the energy transfer to the crystal lattice, are investigated with femtosecond electron diffraction. They are compared to situations in which more delocalized carriers are generated and therefore different relaxation pathways contribute. At the end of the chapter, further investigations of the dynamics of WSe_2 and TMDC-heterostructures are proposed.

6.1. Lattice structure of TMDCs

Transition metal dichalcogenides are layered materials with strong covalent bonds between atoms in a plane and weaker van-der-Waals interactions between neighboring planes [Dic23, Wan12]. Their general chemical composition is MX_2, where M is a transition metal (group IV, V and VI of the periodic system) and X is a chalcogen atom (most commonly S, Se and Te). The semiconducting TMDCs of Mo or W with S or Se, which are described in this chapter, are therefore a subgroup of the TMDCs in general. Their chemical composition is reflected in each of the layers, which are made up of two sheets of chalcogen atoms, separated by a sheet of metal atoms (X-M-X). The inter-

layer distance between two sheets of MoS_2 is 6.5 Å[Rad11] and of WSe_2 6.45 Å[Lin14], indicating the comparably weak binding between neighboring sheets. A sketch of the lattice structure of a multilayer TMDCs, illustrating the layered composition, is shown in figure 6.1 a).

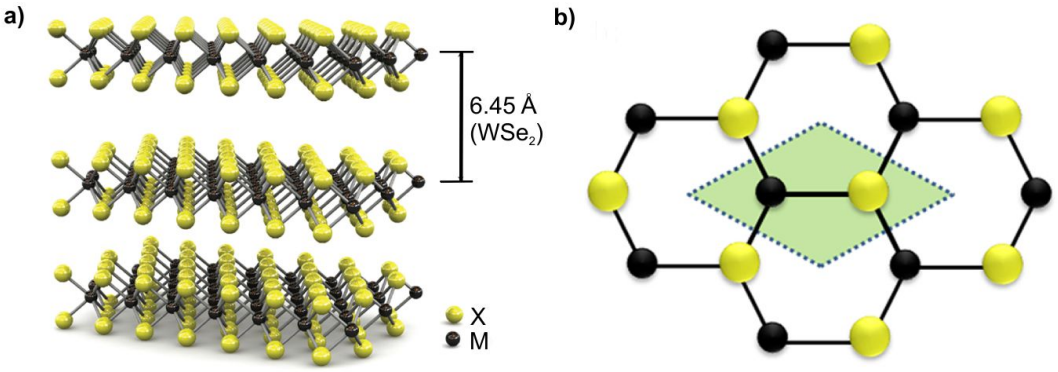

Figure 6.1.: a) Sketch of the crystal structure of TMDCs with composition MX_2. Taken from [Rad11]. The interlayer distance is given for WSe_2, but is similar for other compounds. **b)** Top view onto a layer, showing the honeycomb lattice structure with the broken inversion symmetry. Taken from [Xu13].

The structure within a sheet is depicted in figure 6.1 b), which shows the top view onto a layer. The atoms form a hexagonal honeycomb structure with metal and chalcogen atoms sitting at alternating corners. Several layers of semiconducting TMDCs are usually stacked in the 2H-form, such that the unit-cell comprises two layers [Wan12]. Whereas a monolayer does not have a point of spatial inversion symmetry, such a point exists in the middle of two 2H-stacked layers.

6.2. Electronic structure and photo-excitation of multilayer WSe_2

The electronic band-structure of (bulk) TMDCs has been subject to publications long before their potential to be produced in isolated monolayers was discovered (see e.g. [Fin97]). With the renewed interest in TMDCs, more recent publications focused on different aspects, such as the spin-splitting of the valence bands [Ril14] and the changes of the bandstructure with the number of layers [Jin13].

A calculated (single-particle) band-structure of bulk WSe_2 is shown in figure 6.2 a). WSe_2 possesses an indirect band-gap of size $E_g \approx 1.2\,\text{eV}$ (the values of all band positions differ by around 100 meV between different publications) with the valence band maximum being at Γ in the Brillouin zone and the conduction band minimum at a point X, which is situated between Γ and K [Fin97]. The smallest direct transitions are situated at K, where the valence band exhibits an unusually strong spin-splitting of 0.5 eV [Ril14] and the direct gap size E_g' is 1.6 eV [Fri63]. In monolayers, the spin-splitting is reversed between the two unequal points K and K' [Xia12], which, in reciprocal space, represent the two neighboring corners of the hexagonal Brillouin zone. A schematic drawing of the bandstructure around the K points is shown in figure 6.2 c). The excitation from only one of the bands to the conduction band therefore creates a spin-polarized population of electrons in the valley of the conduction band at K or one of the opposite spin at K', respectively. The overall spin polarization of the conduction minimum is called the valley pseudo-spin and it has been suggested to be used for spintronic applications [Mak12, Gon13, Xu14]. In bulk crystals, the unit cell comprises two layers, and the missing spatial inversion symmetry of isolated monolayers is restored. This means that the K point of one layer falls together with K' of the next layer, lifting the spin degeneracy of the bands. However, it has been suggested that, by considering local atomic site symmetries rather than unit cell symmetries, spin-polarization can also occur in bulk crystals [Zha14].

A measured absorption spectrum [Zha13] of single- and multilayer WSe_2 is shown in figure 6.2 b). The conservation of angular momentum in the process of absorption of a photon leads to a vanishingly small probability of the absorption of photons with energies bigger than the indirect, but smaller than the direct transition, because they require the absorption or creation of a phonon. Above the energy of the direct transition, several absorption peaks can be seen. The one at the smallest photon energies, just on the first absorption edge, was labeled A [Wil69] and corresponds to transitions from the upper of the spin-split bands at K (or K') to the conduction band. The B-resonance is the transition from the lower lying of the two bands to the conduction band. Since the two bands have very large spin polarization, two neighboring valleys at K or K' can be selectively excited with optical light of defined helicity [Mak12, Zen12]. As a result of the reduced dimensionality of TMDCs, the dielectric screening between charged particles is comparably weak, giving rise to many-body phenomena like the formation of bound electron-hole pairs (excitons) [Che12, Ram12, Qiu13, Ye14]. The large absorption at the A and B-transitions are a result of such an excitonic resonance. For the correct description of some effects, the band-structure therefore needs to be modified to include multi-particle effects.

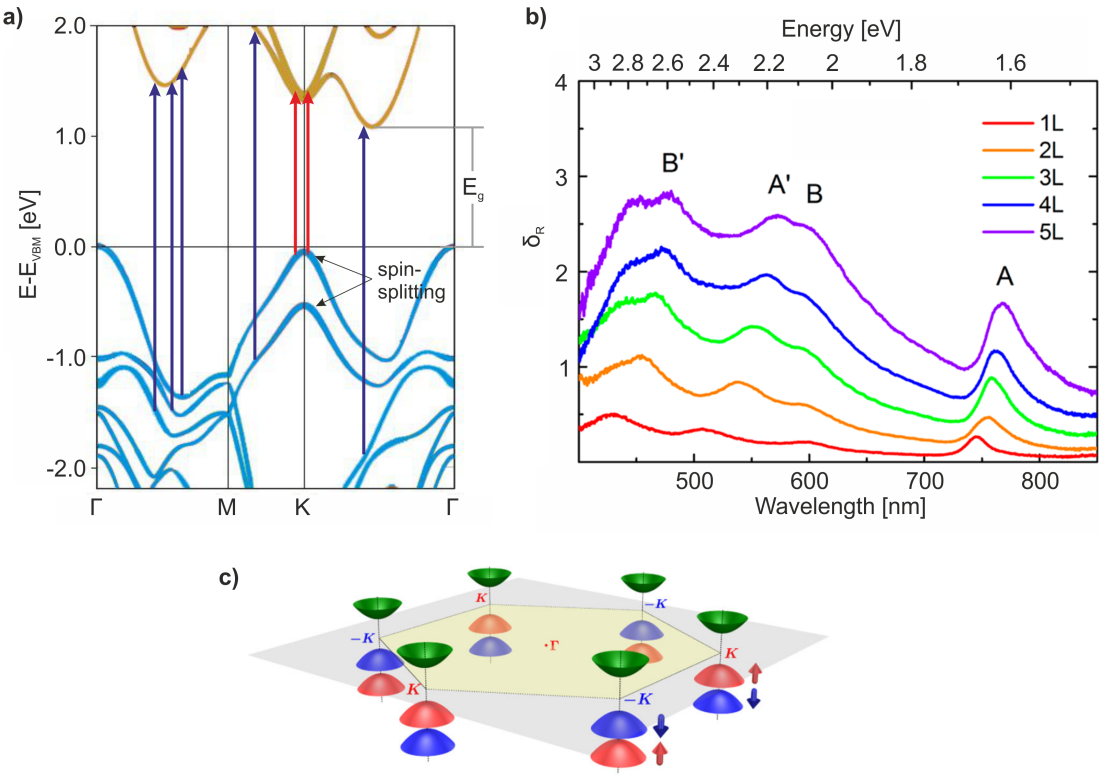

Figure 6.2.: **a)** Band structure of WSe_2 and possible excitations with a laser of 1.6 eV photons (red arrows) and of 3 eV photons (blue arrows). The only transitions of the 1.6 eV photons are around the K-point and provide little excess energy to the electrons. Several transitions all over k-space are allowed for photons of 3 eV energy. Modified from [Ril14]. **b)** Absorbance spectrum of WSe_2 (given as change in reflectivity, which linearly relates to the absorbance). The absorption features labeled A and B correspond to the transitions from the spin-split bands at the K-points. Taken from [Zha13]. **c)** Schematic drawing of the spin-polarized band structure at the K points. Taken from [Xia12].

With the photons of the Ti:Sa laser having energies between $1.47 - 1.63$ eV (FWHM), in WSe_2 the blue part of the spectrum can drive transitions from the valence to the conduction band with little excess energy, while being localized in momentum-space around the two K-points (for monolayers of MoS_2, see [Gru15]). These transitions are shown as red arrows in figure 6.2 a). At low excitation densities, photoexcited electrons and holes have been found to form excitons [Che15, Poe15]. By increasing the excitation density, however, the large amount of free carriers screens the forces between electrons and holes, and the binding energy of the excitons is reduced, until it reaches zero at the so-called Mott transition [Che15]. In this excitation regime, excited electrons are still localized in k-space, but are not bound to holes. By increasing the photon energy,

more direct transitions become available. The second harmonic of a Ti:Sa laser (photon energy centered around 3 eV) can induce transitions at many positions in k-space. The possible transitions are shown as blue arrows in figure 6.2 b). The distribution of excited electrons is in this case more delocalized in k-space, and electrons have, on average, a higher excess-energy with respect to the conduction band minimum.

With decreasing layer thickness, the band-structure of WSe_2 changes gradually and the indirect bandgap increases. At monolayer thicknesses, the transition at K becomes the smallest band-gap, such that WSe_2 becomes a direct semiconductor [Spl10, Zha13]. Due to the reduced Coulomb screening, the excitonic binding energies increase to around 0.5 meV [He14, Che14].

6.3. Preparation of free-standing WSe_2 samples

The lattice structure of TMDCs, consisting of 2-dimensional sheets with weak interlayer couplings, facilitates the preparation of thin, free-standing films. In a top-down approach, they can be thinned out, down to a single layer, by repeated micromechanical cleaving of a bulk crystal with an adhesive tape, similarly as reported for graphite [Nov05b]. Here, a bulk crystal of a TMDC (HQ graphene) was glued to the flat surface of a polished glass cylinder with a glue which is entirely dissolvable in acetone (crystal bond, Plano GmbH). The crystal is then thinned out by repeated cleaving, and after each cleaving step, the optical transmission of the film is monitored in an optical microscope. Once a sufficiently thin flake of large enough lateral size is produced, it is transferred to a TEM grid by dissolving the glue in acetone and carefully picking up the floating film with the TEM grid, which is held by tweezers. The film thickness is then characterized by its optical transmission and by static diffraction images.

Figure 6.3 a) shows a microscope image of a micromechanically thinned flake of WSe_2, illuminated from the backside. Areas with different thickness can be identified by the intensity of transmitted light. The area, marked with II, has a thickness of around 30-60 nm, judging by the color in which they appear [Fri63]. More precise optical measurements of the thickness are possible if the absorption of a single layer and the spectral dependence of the absorptivity as a function of layers were known, which was not the case at the time the images were taken. In b), a real-space electron microscope image of WSe_2 with atomic resolution, taken by M. Willinger of the inorganic chemistry department of the FHI, is presented. The regular hexagonal structure of the atoms is visible, and no signs of defects are found in the image. A diffraction pattern, taken

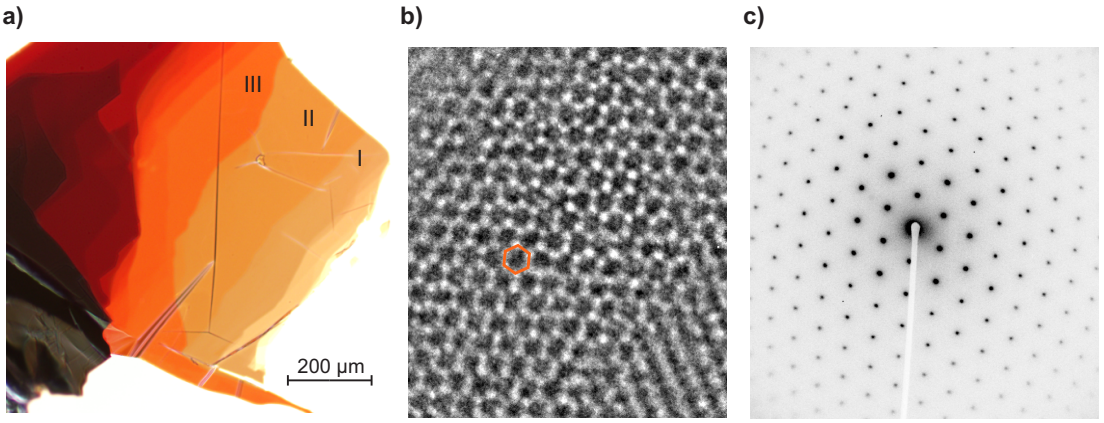

Figure 6.3.: **a)** Microscope image of exfoliated WSe_2 on a glass substrate illuminated with a broadband white-light source in transmission geometry. Areas of different thickness are recognizable by their transmission characteristics. Area II has, judging purely from their color, a thickness of 30-60 nm. **b)** Transmission electron microscope image. The hexagonal lattice structure can be seen with atomic resolution and is highlighted by the orange hexagon. Taken by M. Willinger, FHI. **c)** Typical diffraction pattern, taken with the FED setup. More than 100 Bragg peaks are visible.

with the femtosecond electron diffractometer is shown in c). More than 100 individual Bragg-peaks are visible and the high symmetry of intensities of all orders shows that the sample has an orientation with its surface normal almost parallel to the electron pulse propagation direction.

6.4. Excited state dependent electron-lattice coupling

All measurements of this section were performed with the electron diffraction setup described in chapter 2.1. In figure 6.4 a), a detail of a typical diffraction pattern of a thin film of WSe_2 is shown. The image was taken with an integration time of 5 s, which almost saturates the first order peaks on the camera. Two reciprocal lattice vectors are drawn in the image, which define the labeling of the peaks. The diffraction images are then analyzed as described in detail in appendix A. Since the angle of incidence of the electrons was close to normal to the film surface in the experiments, only diffraction spots with index (jk0) are observed and all peaks of the same diffraction order, indicated by the same color of the boxes drawn around the peaks, are similar in intensity. In the

case of normal incidence, they are symmetrically equivalent and their intensity is thus averaged in the following.

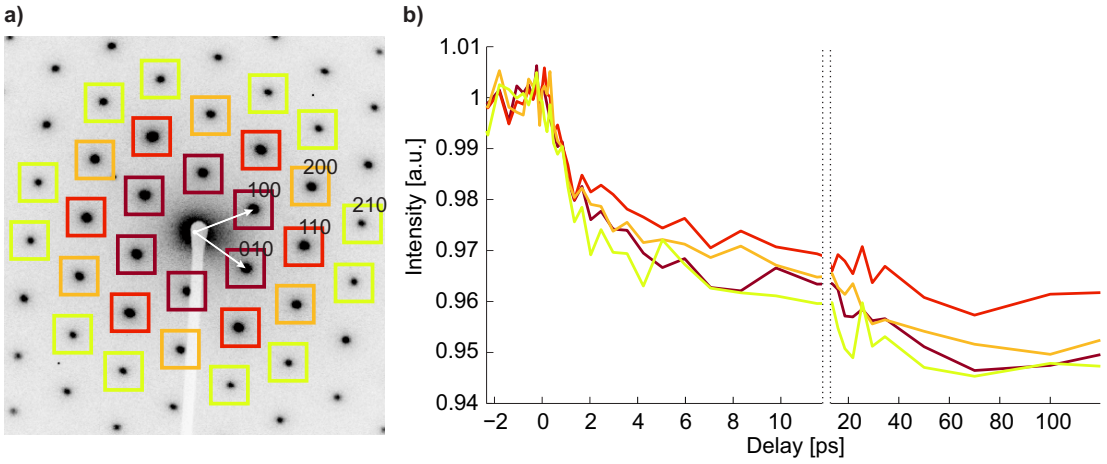

Figure 6.4.: a) Detail of a diffraction pattern of WSe_2. Two reciprocal lattice vectors are shown. Bragg-peaks in boxes of the same color are symmetrically equivalent and their dynamics are thus averaged. **b)** Temporal evolution of the peak intensity of four orders of Bragg-peaks excited with a pump fluence of 19 mJ/cm^2 and 1.6 eV photon energy (fundamental of the Ti:Sa laser). The curves are the average of all boxes of the respective color in a).

Figure 6.4 b) shows the dynamics of the intensity of different orders of Bragg-peaks after photoexcitation with the fundamental frequency of the laser at an incoming fluence of 19 mJ/cm^2. With photoexcitation, the intensity of all peaks decreases within few picoseconds and then continues to decrease until it reaches a new steady state at around 100 ps, which is emphasized by the broken time-axis. Interestingly, the amplitudes of the peaks do not follow the typical $1/s^2$ dependence, which is predicted by the Debye-Waller factor. Reference experiments with cooled samples indicate that the failure of the DW factor is not a non-thermal effect. A possible explanation could be multiple scattering of electrons in the sample. Since the origin of this behavior is not clear, in the following only the (100)-family of peaks is analyzed.

Figure 6.5 a) & b) show the evolution of the average intensity of the family of (100)-peaks after excitation with photons of 1.6 (red circles), corresponding to the high-energy side of the laser spectrum, and 3 eV (blue boxes, center of the second harmonic of the laser spectrum) on two different timescales. To be able to compare the two measurements, the incoming fluences were chosen to lead to a comparable peak-decrease at long time-delays. This means that the energy, which is eventually transferred to the lattice, is similar in both cases. Note that the absorbed total energy can be different,

since the amount of radiatively released energy is unknown. The two figures show that the peakheight decreases on a few ps timescale, but continues to decrease over several tens of picoseconds. To quantify the timescales, a bi-exponential decay is fitted to the data, which is found to well reproduce the dynamics of the peaks of both datasets. In the case of excitation with photons of 1.6 eV, the retrieved timescales are $\tau_1 = (1.4 \pm 0.6)$ ps and $\tau_2 = (26 \pm 7)$ ps. Excitation with photons of 3 eV gives time-constants of $\tau_1 = (0.58 \pm 0.52)$ ps and $\tau_2 = (10.4 \pm 6.6)$ ps. The amplitudes of the two exponentials contribute similarly to the overall peakdecay, in both experimental configurations.

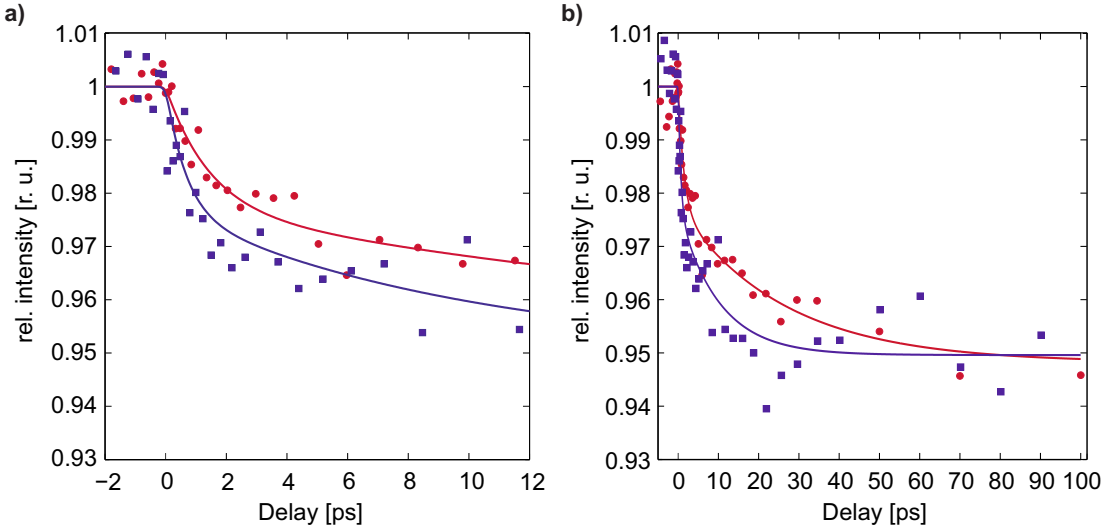

Figure 6.5.: a) & **b)** Temporal evolution of the peak intensity of the family of (100) reflections for pump-pulses centered at 400 nm (blue boxes) and 800 nm (red circles) leading to a comparable total decrease in peak-intensity at long time-delays. Differently fast dynamics are observed in a window of short, as well as long delay times.

The significantly different lattice-dynamics are a manifestation of the different pathways of electron and lattice relaxation. By analyzing the timescales and amplitudes, some information about the underlying physical processes can be obtained. Several processes are expected to contribute to the peak-decrease of the diffraction measurements: energy transfer from electrons to phonons by carrier cooling in the conduction band (and holes in the valence band), including the released energy from exciton dissociation, energy transfer through non-radiative CB-VB recombination (the radiative decay is strongly quenched for multilayers [Mak10]) and the redistribution of phonons, which can lead to an increase in MSD if phonons of higher frequency decay into phonons of lower frequency, as described in chapters 3.2 and 4.1.3. Due to the complexity of the possible pathways, the following explanations can only be considered as a working hypothesis.

The relative energy transfer to phonons by electronic intra-band transitions compared to the total energy release including non-radiative inter-band transitions is around 60% for excitation with 3 eV phonons and around 25% for pumping with photons of 1.6 eV, since the direct bandgap is 1.2 eV [Fin97]. In both experiments, the relative amplitudes of the exponentials are similar, namely around 50% of the entire peak decrease at long delays. It is therefore unlikely that the second exponential decrease is caused by inter-band recombination, since the relative amplitudes are comparable in the two experiments. Values for interband recombination times have been reported to be in the nanosecond range [Shi13]. The first exponential decrease is therefore ascribed to electronic cooling by energy transfer to phonons and the second exponential to phononic thermalization. The different timescales of the first exponential can then be explained by the different phase-space volume available for electron scattering. Excitation of WSe_2 with photons of 1.6 eV creates electronically excited states in the conduction band which are localized around the K-points in reciprocal space, as described in the previous section. The excitation densities here are presumably above the Mott-transition, where the formation of bound excitons is hindered since it has been reported (for bilayer WS_2 excited at the B-resonance) to occur at fluences below 100 $\mu J/cm^2$ [Che15]. Since the electrons are localized in k-space and free states in the conduction band with lower energy are only available at X, the phase space for electron-electron and electron-phonon scattering is reduced to transitions including these electronic initial and final states. Excitation with the second harmonic of the laser (photon energy 3 eV) creates a broader distribution of excited electrons with bigger excess energy per electron as well as a broader distribution of holes in the valence band. The phase-space of possible scattering of electrons and holes is therefore bigger in this case and the initial cooling of electrons and the excitation of phonons is faster. To fulfill momentum conservation, an electron scattering from K to X requires a phonon to be excited with opposite momentum. The reduced phase-space for electronic scattering processes therefore also decreases the phonon modes, which can be excited by theses processes. The different timescales of the second decay could thus be caused by differently narrow phonon distributions, excited through electron cooling, which then relax on different timescales via phonon-phonon coupling. Also the equilibration with out-of-plane phonons might influence the relaxation dynamics, but can not accessed in the experimental geometry used here. Tilting the sample with respect to the electron beam would allow to monitor also Bragg reflections with index (hkl) instead of exclusively (hk0), as is the case here, and therefore allow to measure in-plane as well as out-of-plane dynamics.

The experiments presented here show that different lattice heating dynamics can be identified with femtosecond electron diffraction. Even though the experiment of this chapter have a somewhat preliminary nature, they show that the dynamics can in princi-

ple be attributed to different physical processes. Further experiments can be conducted to more precisely specify the relaxation pathways of electrons and lattice. Electron-scattering processes might be directly investigated with time- and angle resolved photoemission spectroscopy, and transient phonon distributions can be examined by analyzing the incoherently scattered background in diffraction patterns [Tri13, Zhu15]. By tilting the samples, in- and out-of-plane dynamics can be distinguished. The same experimental concepts presented here can also be applied on thinner samples, down to monolayer thicknesses. Such experiments can address the fundamental physical question of how dimensionality changes the electron-phonon coupling in monolayer samples, and at the same time yield valuable information for novel applications employing single-layer TMDCs.

6.5. Outlook: Heterostructures

By combining several layered materials into stacks, new macro-materials with very interesting and tunable properties are imaginable [Gei13, Yu13, Lin15, Riv15]. By effectively controlling the interlayer couplings through the use of different layer-orders, the macroscopic electrical or optical properties can be tuned [Yu13, Bri13]. Time-resolved experiments on multilayer-samples can contribute to the understanding of such devices as they are able to reveal fundamental properties of such multilayer stacks. Specifically, changes of the electronic and coupling properties of single layers as well as the electronic and vibrational coupling between layers by selectively exciting only one material can be addressed.

Heterostructures of two-dimensional materials have been produced in top-down approaches by pressing together two exfoliated samples [CG14] and in bottom-up approaches by metal-organic chemical vapor deposition [Lin15]. Figure 6.6 shows the efforts in our lab to produce heterostructures of different TMDCs. In a), a microscope image of a flake of MoS_2 on WSe_2 is shown. The sample was produced by separately cleaving crystals of the two materials, glued to a rigid substrate , down to the desired thickness. Two flakes are chosen, one of which should be glued on the substrate, and the other one attached to the flexible tape. The two flakes are combined by simply pressing the two films together and slowly removing the tape, similarly as reported in [CG14]. In most cases, the film on the tape is cleaved again, yet leaving a heterostructure behind. In b), a diffraction pattern of the heterostructure is shown. The slightly different lattice constants of 3.16 Å (MoS_2, [Sch83]) and 3.28 Å (WSe_2, [Sch87b]) allow to identify the reflections and to assign them to the two materials. From the rotation of the two patterns pattern, a rotation of the lattice structure in real space of the two

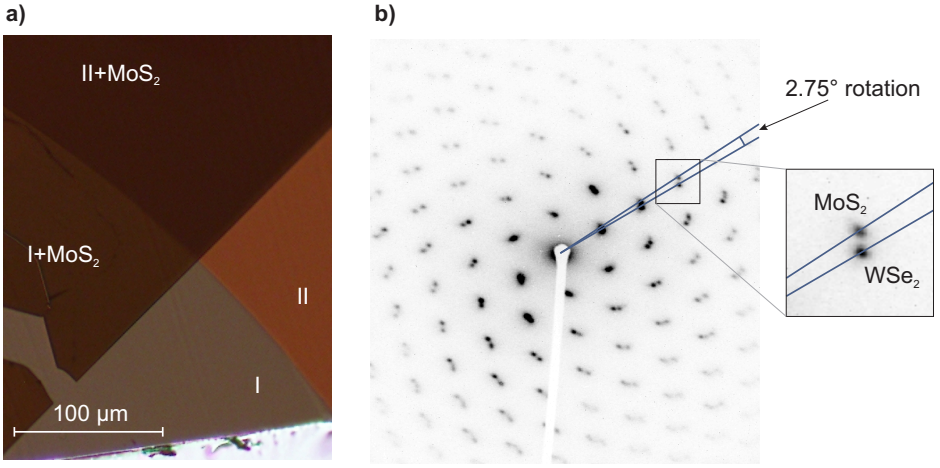

Figure 6.6.: **a)** Transmission microscope image of a heterostructure of WSe_2 and MoS_2. Areas I and II are different thicknesses of WSe_2. The darker areas are the same thicknesses as I and II with a flake of MoS_2 on top. **b)** Diffraction pattern of a TMDC heterostructure of WSe_2 and MoS_2. The rotation of the two patterns is 2.75°, which corresponds to a real-space rotation of the same magnitude. A zoom into a pair of Bragg-peaks emphasizes the different distances to the center due to the different lattice constants of MoS_2 and WSe_2, which allows to assign the reflections.

films of 2.75° is deduced. This method allows for the production of heterostructure samples with areas large enough to conduct electron diffraction studies with them.

7. Summary

The work presented in this thesis investigates optical- and structural dynamics of laser-excited solids by employing different and complementary time-resolved techniques. Structural dynamics are triggered indirectly, by creating non-equilibrium states through the photoexcitation of electrons. These then equilibrate by the interaction with other electrons and by scattering with phonons. The experimental determination of the coupling mechanisms and coupling strengths is therefore possible by the observation of the temporal evolution of the lattice vibrations. Whereas equilibrium interactions can be studied by gently perturbing the system, time-resolved techniques offer the possibility to also study situations far-from equilibrium, like they occur during phase transitions. Different material systems were studied, covering different aspects of the electron-phonon interactions.

In chapter 4.1, femtosecond electron diffraction measurements were performed on the free-electron metal aluminium, which serves as a model system for the description of out-of-equilibrium dynamics, since photoexcitation is known to leave the equilibrium band-structure unperturbed. The incoherent energy transfer from photoexcited electrons to phonons is modeled with rate-equations and the results are compared to first principle calculations. It is found that photoexcitation of aluminium leads to an increase in the measured mean-square displacement on a time-scale well below one picosecond, which is much faster than previously observed [Nie06, Zhu13]. The experimentally observed dynamics are described in the framework of a two temperature model (TTM), but the retrieved coupling parameter is in quantitative disagreement with first principle calculations. The difference is explained by the spectral shape of the Eliashberg function and the phonon density of states, obtained by the *ab initio* calculations, which suggests that the transient phonon distribution should not be described by Bose-Einstein statistics. An increased coupling to high-frequency phonons rather leads to a transiently non-thermal lattice. By dividing the phonons into different subsystems, a new model is introduced (non-thermal-lattice model, NLM). Applying the NLM, a quantitative match between theory and experiment is obtained for electron-phonon coupling parameters taken from the *ab inito* calculations and a phonon-phonon coupling parameter of

$3.5 \cdot 10^{17}\,\mathrm{W/(m^3K)}$. It is shown, that in the NLM, the energy transfer from electrons to phonons proceeds approximately 50% faster than in the TTM. This has far reaching implications on the applicability of the TTM, since it might lead to systematic errors in the quantitative analysis of time-resolved experiments. The concept of subdividing the lattice degrees of freedom into phononic subsystems for describing the energy flow in a material, as introduced here for the case of aluminium, may be applied to a range of materials. In the case of metals, a pronounced spectral dependence of $\alpha^2(\omega)$ suggests that this approach should be followed, and it is expected that a subdivision into the phonon branches may be a generally suitable approach. More complex materials may require partitioning into a larger number of phononic subsystems. Additionally, non-thermal electron-distributions might need to be considered for materials exhibiting weak electron-electron scattering [Mue13].

The non-equilibrium dynamics become more complicated in the case when laser-excitation changes the lattice potential, which is the case in the Peierls-like distorted element antimony. Here, a sudden shift of the potential energy surface induces lattice oscillations in the crystallographic direction of the distortion. Using femtosecond electron diffraction and thin film polycrystalline samples, the coupling of hot electrons to the coherently excited A_{1g} phonon mode and the incoherent energy-transfer to other phonon modes is observed simultaneously. The A_{1g} mode manifests itself in a decrease of the (111) Bragg peak within the time-resolution of the experiment. The other Bragg peaks are used to fit the increase of mean-square displacement, which proceeds with a 2 ps timeconstant. By separating the motion of the A_{1g} phonons from the rest of the lattice vibrations, as proposed in [Gir11], a model of the dynamics of all phonons is obtained. An electron-phonon coupling of $G_{ep} = 1.6 \cdot 10^{16}\,\mathrm{W(m^3K)}$ is obtained for the incoherent energy transfer to the lattice. A quantitative analysis of the phonon-phonon coupling between the A_{1g} mode and all other phonons is theoretically possible from the model and the type of analysis, but requires further measurements with a different sample geometry or an increased coherence of the setup.

The possibility to reversibly switch the phase change material $Ge_2Sb_2Te_5$ (GST) between different crystallographic states is widely used in data-storage applications. In standard technology, the material is heated to above the melting point and the speed of cooling is controlled to initiate a phase change. Based on measurements of the local atomic order, it has been proposed that laser excitation can lead to amorphization pathways that do not require the material to classically melt, but would induce changes to the potential energy surface [Kol04, Kol11]. In chapter 5, optical and diffraction techniques are applied to study the optical and structural dynamics of GST below and above the threshold for amorphization. It is found, that femtosecond near-infrared

pulses immediately excite electrons from resonant bonds, which are responsible for the huge differences in optical properties between the crystalline and amorphous states of GST [Shp08]. When crossing the excitation density for permanent amorphization, resonant bonds are completely suppressed and the optical properties are transiently changed by 30% within the time-resolution of the experiment. Femtosecond electron diffraction reveals that the excitation of resonant bonds does not coincide with immediate structural rearrangements. Instead, it is found that energy is transferred to the lattice in a purely incoherent way, and an exponential increase of lattice temperature with a timeconstant of 2.2 ps is found to best reproduce the data. By increasing the excitation above the threshold for permanent amorphization, the lattice is found to still be describable by the same incoherent energy transfer, with a timeconstant that does not change within the error of the measurement. The threshold fluence of the phase transition is found to coincide with the final lattice temperature reaching the melting temperature. Summarizing the combined optical and diffraction measurements, it is concluded that photoexcitation of GST transiently leads to a state with largely changed optical properties, but a lattice retaining its long-range order. With the optical changes being an order of magnitude larger than in todays silicon photo-switches [Kam10], the decoupling of optical properties from the structural transition is suggested to be exploited in future applications such as all-optical modulators for communications or computations.

Electron diffraction experiments have been performed on the layered semiconducting transition metal dichalcogenide WSe_2, which are described in chapter 6. The complex electronic structure of those material exhibits unusually pronounced many-body effects, in particular the creation of excitons [Fri63, Qiu13] and a strong spin-orbit coupling [Jon14]. Their smallest direct band-transition is situated at the edge of the Brillouin zone. Using pump-pulses with two different photon energies, localized electronic excitations at these points as well as more delocalized electronic excitations are prepared. Significantly different rates of energy transfer are observed in the two cases. These are ascribed to stem from the different possible scattering pathways of photoexcited electrons and holes, which are significantly reduced in the case of the localized excitation. The measurements constitute a basis for future experiments on atomically thin films, for which the reduced dimensionality and the reduced screening of electrons is expected to influence the coupling of electrons to phonons.

This thesis provides experiments, which show that femtosecond electron diffraction can be applied to quantitatively study the interaction of electrons and phonons. Next to established techniques like time-resolved photoemission spectroscopy or *ab initio* theory, it can be used to describe the microscopic interaction mechanisms in solids,

beyond models based on subsystem averages as the two-temperature model. This work suggests that such descriptions can be necessary, in the case of simple metals as well as in more complex materials. In addition, the potential of identifying microscopic pathways of irreversible processes allows for studying far-from equilibrium situations, as they occur during photoinduced phase transitions or chemical reactions.

A. Diffraction data treatment

All electron diffraction experiments presented in this work used an electron camera (TVIPS TemCam F416) to take two-dimensional diffraction images. The analysis of those images was done in several steps, which are described in this section.

Diffraction images were saved as 16 bit integer tiff (tagged image file format) images and the following data-treatment and analysis of all diffraction experiments was done with MATLAB. The images are converted to double precision to be able to properly subtract a background (negative values are needed to have an average of zero counts). The images are multiplied with a flatfield image, which accounts for the inhomogeneous sensitivity of the pixels of the camera. Especially the fiber-bundle, which connects the phosphor screen of the camera to the CMOS chip, shows up as a hexagonal structure of darker pixels and is removed by the flatfield. A flatfield is usually created (in commercial electron microscopes) by taking images without specimen and a widened electron beam, such that a homogeneous illumination of the camera is achieved. Normalizing this image to have an average pixel count of one results in the flatfield. Since a divergent beam can not be created with the magnetic lens alone, here, an amorphous sample was used to create a somewhat similar situation as in an electron microscope. The illumination of the camera is in this case not constant in the radial direction of the diffraction plane, but in its angular direction. Instead of normalizing the entire image by the average count, the pixels are divided by the average count of all pixels with the same distance to the center of the beam. All diffraction images are multiplied by this so-obtained flatfield, effectively removing inhomogeneities of the pixels.

A.1. Polycrystalline samples

In the analysis of diffraction images of polycrystalline samples, as used in most experiments of this work, the diffraction images are integrated angularly to obtain radial averages. Finding the central pixel is crucial in this step to obtain narrow, undistorted radial averages. With the zero order being blocked to protect the camera, the central

pixel is determined iteratively by determination of the width of the Bragg-peaks as a function of the central pixel. The center yielding the most narrow peak is used in the analysis. In the radial integration, parts of the image covered by the beamblock are disregarded in the averaging.

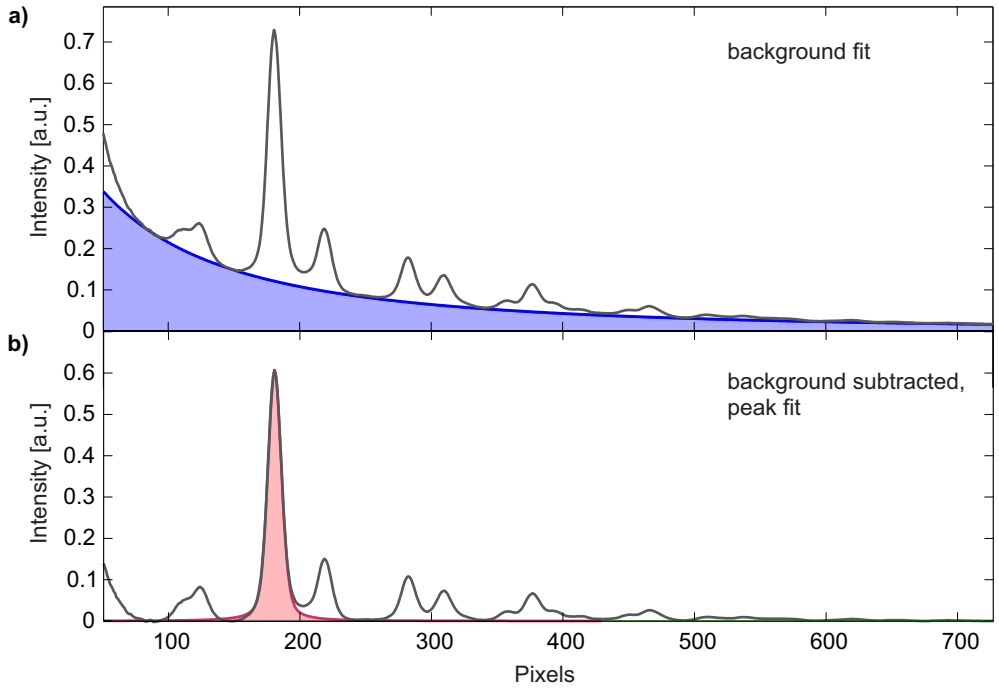

Figure A.1.: a) Raw radial average of antimony and fitted background (dark blue line and shaded area). **b)** Radial average in which the background has been subtracted. The peak is fitted with a pseudo-Voigt line profile (red curve and shaded area).

The radial averages are fitted in several steps. First, a background function is fitted to areas between the peaks which are dominated by (thermal) diffuse scattering. Scattering by the Si_3N_4 capping layers, as used in some of the experiments, is also subtracted like this. The function is chosen empirically for every material to give reasonable fits. Whereas a $1/S^2$ dependence did describe the background of Sb very well, the radial averages of Al were fitted with a sum of a Lorentzian (centered at $S = 0$) and a polynomial of degree 2. The radial averages of GST were fitted with a similar function, but with an additional polynomial of degree 4. The high order polynomial was needed to to correctly subtract also the scattering from the Si_3N_4 layers. An exemplary radial average (of antimony) with a fitted background function is shown in figure A.1 (upper plot). The peaks are subsequently fitted with pseudo-Voigt line profiles, which are defined as a linear combination of a Gaussian and a Lorentzian lineshape and look like the horn of a unicorn: $P(x) = \eta \cdot G(x) + (1 - \eta) \cdot L(x)$. Several iterations of fitting

background and peaks are used to obtain a good measure of the peak's width, intensity, position and mixing parameter η. A fit of a peak is shown in figure A.1 (lower pane).

The calibration of pixel to scattering vector was done separately for every measurement, since it changes with electron energy, lens current and sample position in propagation direction. For samples with known lattice parameters, the calibration could be done directly by fitting the peak's position in pixels against the position known from literature (this method was chosen for Al). The magnetic lens induces aberrations for higher scattering vectors, such that a linear dependence was insufficient in the calibration and a quadratic term was included. The scattering vector in the patterns of antimony and GST were once calibrated by the comparison to a pattern of gold, taken at the same conditions of the setup. Subsequent scattering vector calibration could be done by pattern comparison to these firstly calibrated patterns.

A.2. Single crystalline samples

The emergence of diffraction peaks from single crystalline samples, in contrast to diffraction rings of polycrystalline samples, requires different procedures in the image analysis. In a first step, a background is subtracted and a flatfield is multiplied on the raw diffraction image.

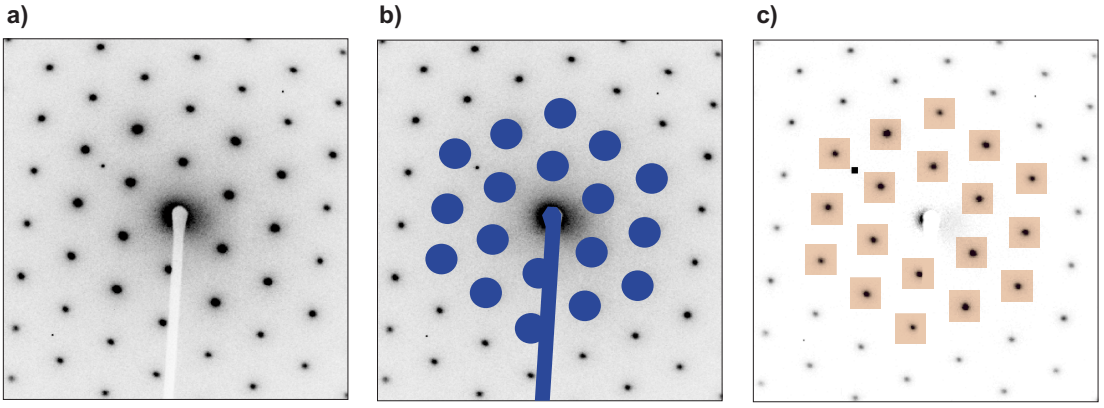

Figure A.2.: **a)** Diffraction image of WSe_2. **b)** The dark blue areas are masked and excluded from the following step of determining the background of inelastically scattered electrons (masks on outer peaks not shown). **c)** Diffraction image with inelastically scattered electrons subtracted. In each orange area, a 2D pseudo-Voigt function is fitted to the respective Bragg-peak.

Assuming little variations in the dynamics of the background intensity in k-space, it is easy to remove the background of inelastically scattered electrons. The procedure

is shown in figure A.2. First, the center is defined by finding the position of a set of diffraction peaks and averaging of their positions, as shown in a). From this set of peaks, all other diffraction peaks are calculated, which is possible if the symmetry of the diffraction pattern is known. All peaks are covered by circular masks of value NaN (not a number), shown in b) in dark blue. A radially averaged intensity is then calculated, excluding all masked areas. By subtracting this averaged intensity, the image of c) is obtained. It contains only diffraction peaks and almost no background. The peak's intensity, position and width are then fitted with 2D pseudo-Voigt functions $P(x, y) = \eta \cdot G(x, y) + (1 - \eta) \cdot L(x, y)$, where G(x,y) and L(x,y) are two-dimensional Gaussian and Lorentzian lineshapes, respectively, in an area around one diffraction peak (orange boxes).

B. Two-temperature model fits

In chapter 4.1, experimentally obtained data of the time-dependent mean square displacement was converted to a time-dependent lattice temperature. Then, the parameters of a two-temperature model were optimized to best fit the data. In a first step, the TTM was optimized using a constant electron-phonon coupling. In a second step, an electron-temperature dependent coupling was fitted. The scripts for fitting were written in MATLAB and the flow of the procedure is described in the following.

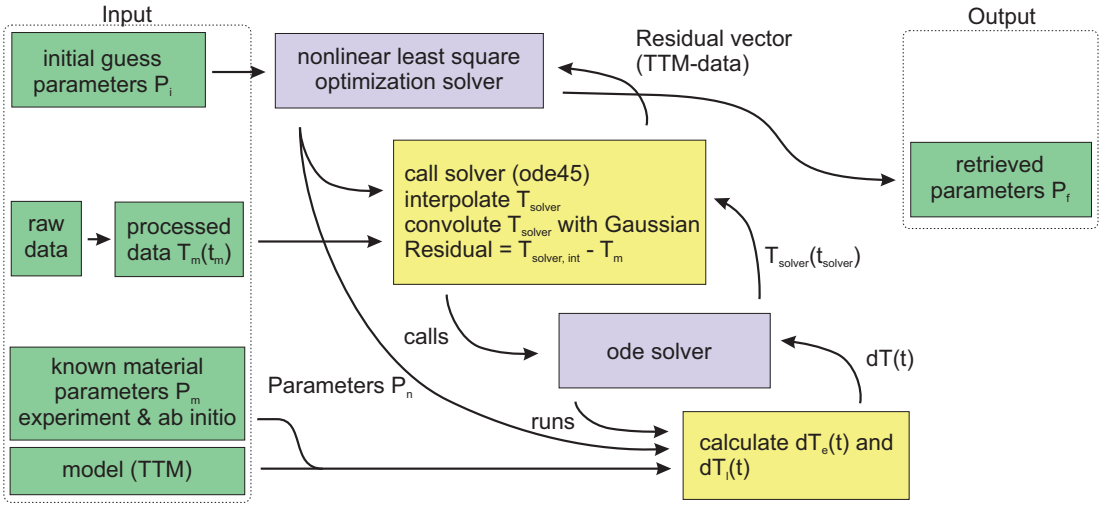

Figure B.1.: Diagram of the principle of fitting a TTM to the diffraction data. Details are given in the text. Functions are depicted in yellow, solvers in blue, parameters and data in green.

A diagram of the work flow in the scripts is shown in figure B.1. Input to the scripts are the measured lattice temperatures at the delay times of the experiment $T_m(t_m)$, which are calculated from the raw data, and a set of known material parameters, i.e. the electronic and lattice heat capacities $C_e(T_e)$ and $C_l(T_l)$ of the material (from *ab initio* calculations), the atomic mass M and the laser pulse duration τ_l. The second set of parameters P is the parameters which are not known and are to be optimized.

Initially, reasonable values P_i are guessed. These are the electron-phonon coupling $G_{ep,i}$, the absorbed energy density $u_{E,i}$, the temporal zero point $t_{0,i}$ and a convolution width $\tau_{conv,i}$, which models the finite time-resolution of the experiment. The latter set of parameters is the input to a non-linear optimization solver (lsqnonlin), which in the end optimizes them to best reproduce the data. It can, however, only minimize the values of a vector. Therefore, a function was written that compares the output of the TTM to the data and returns the difference of the two. Within this function, firstly an ode solver is called (MATLAB ode45), which solves the differential equations of the TTM (given in a second function) with the known parameters and the to be optimized parameters, which are directly supplied by the optimization-solver. The ode solver's output are an electronic and a lattice temperature $T_{l,solver}(t_{solver})$ at certain delay times t_{solver}. To be able to calculate a difference between the ode-solvers output and the data, the temperatures $T_{l,solver}(t_{solver})$ are convoluted with a Gaussian function to account for the time-resolution of the experiment, and then interpolated at the delay times of the experiment t_m. The output of this function therefore is a vector, for which the initial solver can calculate a standard deviation, which it then optimizes. It gives out the final parameters P_f.

Fitting a TTM with an electronic temperature dependent electron-phonon coupling requires one extra parameter, but is similar otherwise. The electron-phonon coupling is split into a low-temperature one (300 K) and a high-temperature one (4000 K). In the function of the TTM, the electron-phonon coupling is then interpolated to the electronic temperature at the respective time-step.

The entire fitting procedure converges only if the start-parameters are not too far off. Also, several local minima are possible. Therefore, the fitting was done for several start-parameters. The deviation in the obtained final parameters directly served as a measure for its error, shown in the respective plots.

Bibliography

[Aid10] M. Aidelsburger, F. O. Kirchner, F. Krausz, & P. Baum. *Single-electron pulses for ultrafast diffraction.* PNAS **107**, 46, (2010) 19714.

[Akh79] D. Akhtar, V. D. Vankar, T. C. Goel, & K. L. Chopra. *Metastable structures of splat-cooled and vapour- depodited lead and antimony films.* Thin Solid Films **58**, (1979) 327.

[All87] P. B. Allen. *Theory of thermal relaxation of electrons in metals.* Physical Review Letters **59**, 13, (1987) 1460.

[And07] K. S. Andrikopoulos, S. N. Yannopoulos, A. V. Kolobov, P. Fons, & J. Tominaga. *Raman scattering study of GeTe and $Ge_2Sb_2Te_5$ phase-change materials.* Journal of Physics and Chemistry of Solids **68**, (2007) 1074.

[Ani67] S. I. Anisimov, A. M. Bonch-Bruevich, M. A. El'yashevich, Ya. A. Imas, N. A. Pavlenko, & G. S. Romanov. *Effect of powerful light fluxes on metals.* Soviet Physics-Technical Physics **11**, (1967) 945.

[Ani74] S. I. Anisimov, B. L. Kapeliovich, & T. L. Perel'man. *Electron emission from metal surfaces exposed to ultrashort laser pulses.* Soviet Physics-JETP **66**, (1974) 776.

[Ash76] N. W. Ashcroft & N. D. Mermin. *Solid State Physics.* Brooks/Cole, 1976.

[Bau98] M. Bauer, S. Pawlik, & Martin Aeschlimann. *Electron dynamics of aluminum investigated by means of time-resolved photoemission.* Proceedings SPIE **3272**, (1998) 201.

[Bec15] F. Bechstedt. *Many-Body Approach to Electronic Excitations.* Springer-Verlag Berlin Heidelberg, 2015.

[Bed92] G. S. Beddard, G. G. McFadyen, G. D. Reid, & J. R. G. Thorne. *Pulse transform transient absorption spectroscopy.* Chemical Physics Letters **198**, (1992) 641.

[Boe62] H. P. Boehm, A. Clauss, G. O. Fischer, & U. Hofmann. *Das Adsorptionsverhalten sehr dünner Kohlenstoff-Folien.* Zeitschrift für anorganische und allgemeine Chemie **316**, (1962) 119.

[Boe94] H. P. Boehm, R. Setton, & E. Stumpp. *Nomenclature and terminology of graphite intercalation compounds.* Pure & Applied Chemistry **66**, 9, (1994) 1893.

[Bol08] K. I. Bolotin, K. J. Sikes, Z. Jiang, M. Klima, G. Fudenberg, J. Hone, P. Kim, & H. L. Stormer. *Ultrahigh electron mobility in suspended graphene.* Solid State Communications **146**, (2008) 351.

[Bor01] M. Born & E. Wolf. *Principles of Optics.* Cambridge university press, 2001.

[Bos08] D. Boschetto, T. Garl, A. Rousse, E. G. Gamaly, & A. V. Rode. *Lifetime of optical phonons in fs-laser excited bismuth.* Applied Physics A: Materials Science and Processing **92**, (2008) 873.

[Bot13] E. M. Bothschafter, A. Paarmann, E. S. Zijlstra, N. Karpowicz, M. E. Garcia, R. Kienberger, & R. Ernstorfer. *Ultrafast Evolution of the Excited-State Potential Energy Surface of TiO_2 Single Crystals Induced by Carrier Cooling.* Physical Review Letters **110**, 6, (2013) 067402.

[Boy08] R. W. Boyd (Hg.). *Nonlinear Optics.* Academic Press, 2008.

[Bri13] L. Britnell, R. M. Ribeiro, A. Eckmann, R. Jalil, B. D. Belle, A. Mishchenko, Y. J. Kim, R. V. Gorbachev, T. Georgiou, S. V. Morozov, A. N. Grigorenko, A. K. Geim, C. Casiraghi, A. H. Castro Neto, & K. S. Novoselov. *Strong light-matter interactions in heterostructures of atomically thin films.* Science **340**, (2013) 1311.

[Bro90] S. D. Brorson, A. Kazeroonian, J. S. Moodera, D. W. Face, T. K. Cheng, E. P. Ippen, M. S. Dresselhaus, & G. Dresselhaus. *Femtosecond room-temperature measurement of the electron-phonon coupling constant γ in metallic superconductors.* Physical Review Letters **64**, 18, (1990) 2172.

[Bru47] F. M. Bruce. *Calibration of uniform-field spark-gaps for high-voltage measurement at power frequencies.* Journal of the Institution of Electrical Engineers - Part II: Power Engineering **94**, (1947) 138.

[Bun08] J. S. Bunch, S. S. Verbridge, J. S. Alden, A. M. Van Der Zande, J. M. Parpia, H. G. Craighead, & P. L. McEuen. *Impermeable atomic membranes from graphene sheets.* Nano Letters **8**, (2008) 2458.

[Cal01] J. Callan, A. Kim, C. Roeser, E. Mazur, J. Solis, J. Siegel, C. Afonso, & J. de Sande. *Ultrafast Laser-Induced Phase Transitions in Amorphous GeSb Films.* Physical Review Letters **86**, 16, (2001) 3650.

[Car10] S. Caravati, M. Bernasconi, T. D. Kühne, M. Krack, & M. Parrinello. *First principles study of crystalline and amorphous $Ge_2Sb_2Te_5$ and the effects of stoichiometric defects.* Journal of Physics: Condensed Matter **22**, 39, (2010) 399801.

[CG14] A. Castellanos-Gomez, M. Buscema, R. Molenaar, V. Singh, L. Janssen, H. S. J. van der Zant, & G. A. Steele. *Deterministic transfer of two-dimensional materials by all-dry viscoelastic stamping.* 2D Materials **1**, (2014) 011002.

[Cha12] R. P. Chatelain, V. R. Morrison, C. Godbout, & B. J. Siwick. *Ultrafast electron diffraction with radio-frequency compressed electron pulses.* Applied Physics Letters **101**, 8, (2012) 081901.

[Cha14] R. P. Chatelain, V. R. Morrison, B. L. M. Klarenaar, & B. J. Siwick. *Coherent and Incoherent Electron-Phonon Coupling in Graphite Observed with Radio-Frequency Compressed Ultrafast Electron Diffraction.* Physical Review Letters **113**, (2014) 235502.

[Che90] T. K. Cheng, S. D. Brorson, a. S. Kazeroonian, J. S. Moodera, G. Dresselhaus, M. S. Dresselhaus, & E. P. Ippen. *Impulsive excitation of coherent phonons observed in reflection in bismuth and antimony.* Applied Physics Letters **57**, (1990) 1004.

[Che12] T. Cheiwchanchamnangij & W. R. L. Lambrecht. *Quasiparticle band structure calculation of monolayer, bilayer, and bulk MoS_2.* Physical Review B **85**, (2012) 205302.

[Che14] A. Chernikov, T. C. Berkelbach, H. M. Hill, A. Rigosi, Y. Li, O. B. Aslan, D. R. Reichman, M. S. Hybertsen, & T. F. Heinz. *Exciton Binding Energy and Nonhydrogenic Rydberg Series in Monolayer WS_2*. Physical Review Letters **113**, (2014) 076802.

[Che15] A. Chernikov, C. Ruppert, H. M. Hill, A. F. Rigosi, & T. F. Heinz. *Population inversion and giant bandgap renormalization in atomically thin WS_2 layers.* Nature Photonics **9**, (2015) 466.

[Chh13] M. Chhowalla, H. S. Shin, G. Eda, L. J. Li, K. P. Loh, & H. Zhang. *The chemistry of two-dimensional layered transition metal dichalcogenide nanosheets.* Nature chemistry **5**, 4, (2013) 263.

[Dac85] M. M. Dacorogna, M. L. Cohen, & P. K. Lam. *Self-Consistent Calculation of the q Dependence of the Electron-Phonon Coupling in Aluminum.* Physical Review Letters **55**, 8, (1985) 837.

[Dan94] M. Dantus, S. B. Kim, J. C. Williamson, & A. H. Zewail. *Ultrafast Electron Diffraction. 5. Experimental Time Resolution and Applications.* Journal of Physical Chemistry **98**, (1994) 2782.

[De 85] S. De Silvestri, J. G. Fujimoto, E. P. Ippen, E. B. Gamble, L. R. Williams, & K. A. Nelson. *Femtosecond time-resolved measurements of optic phonon dephasing by impulsive stimulated raman scattering in α-perylene crystal from 20 to 300 K.* Chemical Physics Letters **116**, 2, (1985) 146.

[Dek00] T. Dekorsy, G. C. Cho, & H. Kurz. *Light Scattering in Solids VIII.* Springer, 2000.

[Dew66] J. F. Dewald, W. R. Northover, & A. D. Pearson. *Multiple resistance semiconductor elements* (1966). U.S. Patent 3,241,009.

[Dia09] M. S. Diakhate, E. S. Zijlstra, & M. E. Garcia. *Quantum dynamical study of the amplitude collapse and revival of coherent A_{1g} phonons in bismuth: A classical phenomenon?* Applied Physics A **96**, (2009) 5.

[Dic23] R. G. Dickinson & L. Pauling. *The crystal structure of molybdenite.* Journal of the American Chemical Society **45**, (1923) 1466.

[Din11] Y. Ding, Y. Wang, J. Ni, L. Shi, S. Shi, & W. Tang. *First principles study of structural, vibrational and electronic properties of graphene-like MX_2 (M=Mo, Nb, W, Ta; X=S, Se, Te) monolayers.* Physica B **406**, 11, (2011) 2254.

[Dre08] M. S. Dresselhaus, G. Dresselhaus, & A. Jorio. *Group Theory: Application to the Physics of Condensed Matter.* Springer, 2008.

[Dwy06] J. R. Dwyer, C. T. Hebeisen, R. Ernstorfer, M. Harb, V. B. Deyirmenjian, R. E. Jordan, & R. J. D. Miller. *Femtosecond electron diffraction: 'making the molecular movie'.* Philosophical Transactions of the Royal Society A **364**, 1840, (2006) 741.

[EA87] H. E. Elsayed-Ali, T. B. Norris, M. A. Pessot, & G. A. Mourou. *Time-resolved observation of electron-phonon relaxation in copper.* Physical Review Letters **58**, 12, (1987) 1212.

[Eic10] M. Eichberger, H. Schäfer, M. Krumova, M. Beyer, J. Demsar, H. Berger, G. Moriena, G. Sciaini, & R. J. D. Miller. *Snapshots of cooperative atomic motions in the optical suppression of charge density waves.* Nature **468**, 7325, (2010) 799.

[Els14] T. Elsaesser & M. Woerner. *Perspective: Structural dynamics in condensed matter mapped by femtosecond x-ray diffraction.* The Journal of Chemical Physics **140**, 2014, (2014) 020901.

[Ern09] R. Ernstorfer, M. Harb, C. T. Hebeisen, G. Sciaini, T. Dartigalongue, & R. J. D. Miller. *The formation of warm dense matter: experimental evidence for electronic bond hardening in gold.* Science **323**, 5917, (2009) 1033.

[Fau13] J. Faure, J. Mauchain, E. Papalazarou, M. Marsi, D. Boschetto, I. Timrov, N. Vast, Y. Ohtsubo, B. Arnaud, & L. Perfetti. *Direct observation of electron thermalization and electron-phonon coupling in photoexcited bismuth.* Physical Review B **88**, (2013) 075120.

[Fil06] E. Fill, L. Veisz, A. Apolonski, & F. Krausz. *Sub-fs electron pulses for ultrafast electron diffraction.* New Journal of Physics **8**, 11, (2006) 272.

[Fin97] T. Finteis, M. Hengsberger, T. Straub, K. Fauth, R. Claessen, P. Auer, P. Steiner, S. Hüfner, P. Blaha, M. Vögt, M. Lux-Steiner, & E. Bucher. *Oc-*

cupied and unoccupied electronic band structure of WSe_2. Physical Review B **55**, 16, (1997) 10400.

[Fis77] P. Fischer, I. Sosnowska, & M. Szymanski. *Debye-Waller factor and thermal expansion of arsenic, antimony and bismuth.* Journal of Physics C **11**, (1977) 1043.

[Fri63] R. F. Frindt. *The optical properties of single crystals of WSe_2 and $MoTe_2$.* Journal of Physics and Chemistry of Solids **24**, (1963) 1107.

[Fri00] I. Friedrich, V. Weidenhof, W. Njoroge, P. Franz, & M. Wuttig. *Structural transformations of $Ge_2Sb_2Te_5$ films studied by electrical resistance measurements.* Journal of Applied Physics **87**, 9, (2000) 4130.

[Fri07] D. M. Fritz, D. A. Reis, B. Adams, R. A. Akre, J. Arthur, C. Blome, P. H. Bucksbaum, A. L. Cavalieri, S. Engemann, S. Fahy, R. W. Falcone, P. H. Fuoss, K. J. Gaffney, M. J. George, J. Hajdu, M. P. Hertlein, P. B. Hillyard, M. Horn-von Hoegen, M. Kammler, J. Kaspar, R. Kienberger, P. Krejcik, S. H. Lee, A. M. Lindenberg, B. McFarland, D. Meyer, T. Montagne, E. D. Murray, A. J. Nelson, M. Nicoul, R. Pahl, J. Rudati, H. Schlarb, D. P. Siddons, K. Sokolowski-Tinten, T. Tschentscher, D. von der Linde, & J. B. Hastings. *Ultrafast bond softening in bismuth: mapping a solid's interatomic potential with X-rays.* Science **315**, 5812, (2007) 633.

[Gao12] M. Gao, H. Jean-Ruel, R. R. Cooney, J. Stampe, M. De Jong, M. Harb, G. Sciaini, G. Moriena, & R. J. D. Miller. *Full characterization of RF compressed femtosecond electron pulses using ponderomotive scattering.* Optics Express **20**, 11, (2012) 12048.

[Gar96] G. Garrett, T. Albrecht, J. Whitaker, & R. Merlin. *Coherent THz Phonons Driven by Light Pulses and the Sb Problem: What is the Mechanism?* Physical Review Letters **77**, (1996) 3661.

[Gei13] A. K. Geim & I. V. Grigorieva. *Van der Waals heterostructures.* Nature **499**, 7459, (2013) 419.

[Ger12] C. Gerbig, S. Morgenstern, C. Sarpe, M. Wollenhaupt, & T. Baumert. *Femtosecond Transmission Electron Diffraction on Single Crystalline Graphite.*

In *Research in Optical Sciences*. Osa, Washington, D.C., 2012 IT3D.3. URL http://www.opticsinfobase.org/abstract.cfm?URI=ICUSD-2012-IT3D.3.

[Ger15] C. Gerbig, A. Senftleben, S. Morgenstern, C. Sarpe, & T. Baumert. *Spatio-temporal resolution studies on a highly compact ultrafast electron diffractometer*. New Journal of Physics **17**, 4, (2015) 043050.

[Gir11] Y. Giret, A. Gellé, & B. Arnaud. *Entropy driven atomic motion in laser-excited bismuth*. Physical Review Letters **106**, (2011) 155503.

[Gon13] Z. Gong, G. B. Liu, H. Yu, D. Xiao, X. Cui, X. Xu, & W. Yao. *Magnetoelectric effects and valley-controlled spin quantum gates in transition metal dichalcogenide bilayers*. Nature communications **4**, (2013) 2053.

[Gri81] G. Grimvall & E. P. Wohlfahrt (Hg.). *The Electron-Phonon Interaction in Metals*, Bd. 16 von *Selected Topics in Solid State Physics*. North-Holland publishing, 1981.

[Gru15] A. Grubišić Čabo, J. A. Miwa, S. S. Grønborg, J. M. Riley, J. C. Johannsen, C. Cacho, O. Alexander, R. T. Chapman, E. Springate, M. Grioni, J. V. Lauritsen, P. D. C. King, P. Hofmann, & S. Ulstrup. *Observation of Ultrafast Free Carrier Dynamics in Single Layer MoS_2*. Nano Letters **15**, (2015) 5883.

[Har08] M. Harb, R. Ernstorfer, C. T. Hebeisen, G. Sciaini, W. Peng, T. Dartigalongue, M. Eriksson, M. Lagally, S. Kruglik, & R. J. D. Miller. *Electronically Driven Structure Changes of Si Captured by Femtosecond Electron Diffraction*. Physical Review Letters **100**, 15, (2008) 1.

[Has98] M. Hase, K. Mizoguchi, H. Harima, S. I. Nakashima, & K. Sakai. *Dynamics of coherent phonons in bismuth generated by ultrashort laser pulses*. Physical Review B **58**, 9, (1998) 5448.

[Has10] M. Hase & M. Kitajima. *Interaction of coherent phonons with defects and elementary excitations*. Journal of Physics: Condensed matter **22**, (2010) 073201.

[He14] K. He, N. Kumar, L. Zhao, Z. Wang, K. F. Mak, H. Zhao, & J. Shan. *Tightly Bound Excitons in Monolayer WSe_2*. Physical Review Letters **113**, 2, (2014) 026803.

[Heb06] C. T. Hebeisen, R. Ernstorfer, M. Harb, T. Dartigalongue, R. E. Jordan, & R. J. D. Miller. *Femtosecond electron pulse characterization using laser ponderomotive scattering.* Optics Letters **31**, 23, (2006) 3517.

[Heb08] C. T. Hebeisen, G. Sciaini, M. Harb, R. Ernstorfer, T. Dartigalongue, Sergei G. Kruglik, & R. J. D. Miller. *Grating enhanced ponderomotive scattering for visualization and full characterization of femtosecond electron pulses.* Optics Express **16**, 5, (2008) 3334.

[Hop09] P. E. Hopkins & P. M. Norris. *Contribution of Ballistic Electron Transport to Energy Transfer During Electron-Phonon Nonequilibrium in Thin Metal Films.* Journal of Heat Transfer **131**, 4, (2009) 043208.

[Hos99] J. L. Hostetler, A. N. Smith, D. M. Czajkowsky, & P. M. Norris. *Measurement of the Electron-Phonon Coupling Factor Dependence on Film Thickness and Grain Size in Au, Cr, and Al.* Applied Optics **38**, 16, (1999) 3614.

[Hos14] P. Hosseini, C. D. Wright, & H. Bhaskaran. *An optoelectronic framework enabled by low-dimensional phase-change films.* Nature **511**, 7508, (2014) 206.

[Hsi13] W. P. Hsieh, P. Zalden, M. Wuttig, A. M. Lindenberg, & W. L. Mao. *High-pressure Raman spectroscopy of phase change materials.* Applied Physics Letters **103**, (2013) 191908.

[Hua98] L. Huang, J. Callan, E. Glezer, & E. Mazur. *GaAs under Intense Ultrafast Excitation: Response of the Dielectric Function.* Physical Review Letters **80**, 1, (1998) 185.

[Hua10] B. Huang & J. Robertson. *Bonding origin of optical contrast in phase-change memory materials.* Physical Review B **81**, 8, (2010) 081204.

[Int92] International Union of Crystallography. *Report of the Executive Committee for 1991.* Acta Crystallographica Section A **48**, 6, (1992) 928.

[Ish06] K. Ishioka, M. Hase, M. Kitajima, & H. Petek. *Coherent optical phonons in diamond.* Applied Physics Letters **89**, (2006) 231916.

[Ish08] K. Ishioka, M. Kitajima, & O. V. Misochko. *Coherent A_{1g} and E_g phonons of antimony.* Journal of Applied Physics **103**, 12, (2008) 123505.

[Ish10] K. Ishioka & O. V. Misochko. *Coherent Lattice Oscillations in Solids and Their Optical Control.* In Kaoru Yamanouchi, Antonio Giulietti, & Kenneth Ledingham (Hg.), *Progress in Ultrafast Intense Laser Science*, Bd. V von *Springer Series in Chemical Physics*. Springer Berlin Heidelberg, 2010 23–46.

[Jin13] W. Jin, P. C. Yeh, N. Zaki, D. Zhang, J. T. Sadowski, A. Al-Mahboob, A. M. Van Der Zande, D. A. Chenet, J. I. Dadap, I. P. Herman, P. Sutter, J. Hone, & R. M. Osgood. *Direct measurement of the thickness-dependent electronic band structure of MoS_2 using angle-resolved photoemission spectroscopy.* Physical Review Letters **111**, (2013) 106801.

[Joh08] S. L. Johnson, P. Beaud, C. J. Milne, F. S. Krasniqi, E. S. Zijlstra, M. E. Garcia, M. Kaiser, D. Grolimund, R. Abela, & G. Ingold. *Nanoscale depth-resolved coherent femtosecond motion in laser-excited bismuth.* Physical Review Letters **100**, (2008) 155501.

[Jon14] A. M. Jones, H. Yu, J. S. Ross, P. Klement, N. J. Ghimire, J. Yan, D. G. Mandrus, W. Yao, & X. Xu. *Spin-layer locking effects in optical orientation of exciton spin in bilayer WSe_2.* Nature Physics **10**, 2, (2014) 130.

[Kam10] T. Kampfrath, D. M. Beggs, T. P. White, A. Melloni, T. F. Krauss, & L. Kuipers. *Ultrafast adiabatic manipulation of slow light in a photonic crystal.* Physical Review A **81**, (2010) 043837.

[Kas09] G. H. Kassier, K. Haupt, N. Erasmus, E. G. Rohwer, & H. Schwoerer. *Achromatic reflectron compressor design for bright pulses in femtosecond electron diffraction.* Journal of Applied Physics **105**, 11, (2009) 113111.

[Kas10] G. H. Kassier, K. Haupt, N. Erasmus, E. G. Rohwer, H. M. von Bergmann, H. Schwoerer, S. M. M. Coelho, & F. D. Auret. *A compact streak camera for 150 fs time resolved measurement of bright pulses in ultrafast electron diffraction.* Review of Scientific Instruments **81**, 10, (2010) 105103.

[Kat13] H. Katsuki, J.C. Delagnes, K. Hosaka, K. Ishioka, H. Chiba, E.S. Zijlstra, M.E. Garcia, H. Takahashi, K. Watanabe, M. Kitajima, Y. Matsumoto, K.G. Nakamura, & K. Ohmori. *All-optical control and visualization of ultrafast two-dimensional atomic motions in a single crystal of bismuth.* Nature Communications **4**, (2013) 2801.

[Kim98] J. H. Kim & M. R. Kim. *Effects of Microstructure on Optical Properties of $Ge_2Sb_2Te_5$ Thin Films.* Japanese Journal of Applied Physics **37**, (1998) 2116.

[Kir13a] F. O. Kirchner, A. Gliserin, F. Krausz, & P. Baum. *Laser streaking of free electrons at 25 keV.* Nature Photonics **8**, 1, (2013) 52.

[Kir13b] F. O. Kirchner, S. Lahme, F. Krausz, & P. Baum. *Coherence of femtosecond single electrons exceeds biomolecular dimensions.* New Journal of Physics **15**, 6, (2013) 063021.

[Kit05] C. Kittel. *Introduction to Solid State Physics, 8th Edition.* Wiley, 2005.

[Koh06] S. Kohara, K. Kato, S. Kimura, H. Tanaka, T. Usuki, K. Suzuya, H. Tanaka, Y. Moritomo, T. Matsunaga, N. Yamada, Y. Tanaka, H. Suematsu, & M. Takata. *Structural basis for the fast phase change of $Ge_2Sb_2Te_5$: Ring statistics analogy between the crystal and amorphous states.* Applied Physics Letters **89**, 20, (2006) 201910.

[Kol04] A. V. Kolobov, P. Fons, A. I. Frenkel, A. L. Ankudinov, J. Tominaga, & T. Uruga. *Understanding the phase-change mechanism of rewritable optical media.* Nature Materials **3**, 10, (2004) 703.

[Kol09] A. V. Kolobov, P. Fons, M. Krbal, R. E. Simpson, S. Hosokawa, T. Uruga, H. Tanida, & J. Tominaga. *Liquid $Ge_2Sb_2Te_5$ studied by extended x-ray absorption.* Applied Physics Letters **95**, (2009) 241902.

[Kol11] A. V. Kolobov, M. Krbal, P. Fons, J. Tominaga, & T. Uruga. *Distortion-triggered loss of long-range order in solids with bonding energy hierarchy.* Nature Chemistry **3**, 4, (2011) 311.

[Lan05] M. H. R. Lankhorst, B. W. S. M. M. Ketelaars, & R. A. M. Wolters. *Low-cost and nanoscale non-volatile memory concept for future silicon chips.* Nature Materials **4**, 4, (2005) 347.

[Lan07] C. Lang, S. Song, D. Manh, & D. Cockayne. *Building blocks of amorphous $Ge_2Sb_2Te_5$.* Physical Review B **76**, (2007) 054101.

[Lat95] R. Latham (Hg.). *High Voltage Vacuum Insulation.* Academic Press, 1995.

[Lee08] C. Lee, X. Wei, J. W. Kysar, & J. Hone. *Measurement of the elastic properties and intrinsic strength of monolayer graphene.* Science **321**, (2008) 385.

[Leg13] P. M. Leguay, A. Lévy, B. Chimier, F. Deneuville, D. Descamps, C. Fourment, C. Goyon, S. Hulin, S. Petit, O. Peyrusse, J. J. Santos, P. Combis, B. Holst, V. Recoules, P. Renaudin, L. Videau, & F. Dorchies. *Ultrafast Short-Range Disordering of Femtosecond-Laser-Heated Warm Dense Aluminum.* Physical Review Letters **111**, 24, (2013) 245004.

[Len08] D. Lencer, M. Salinga, B. Grabowski, T. Hickel, J. Neugebauer, & M. Wuttig. *A map for phase-change materials.* Nature Materials **7**, (2008) 972.

[Lie55] G. Liebmann. *A unified representation of magnetic electron lens properties.* Proceedings of the Physical Society Section B **68**, (1955) 737.

[Lin05] A. M. Lindenberg, J. Larsson, K. Sokolowski-Tinten, K. J. Gaffney, C. Blome, O. Synnergren, J. Sheppard, C. Caleman, A. G. Macphee, D. Weinstein, D. P. Lowney, T. K. Allison, T. Matthews, R. W. Falcone, A. L. Cavalieri, D. M. Fritz, S. H. Lee, P. H. Bucksbaum, D. A. Reis, J. Rudati, P. H. Fuoss, C. C. Kao, D. P. Siddons, R. Pahl, J. Als-Nielsen, S. Duesterer, R. Ischebeck, H. Schlarb, H. Schulte-Schrepping, T. Tschentscher, J. Schneider, D. von der Linde, O. Hignette, F. Sette, H. N. Chapman, R. W. Lee, T. N. Hansen, S. Techert, J. S. Wark, M. Bergh, G. Huldt, D. van der Spoel, N. Timneanu, J. Hajdu, R. A. Akre, E. Bong, P. Krejcik, J. Arthur, S. Brennan, K. Luening, & J. B. Hastings. *Atomic-scale visualization of inertial dynamics.* Science **308**, 5720, (2005) 392.

[Lin08] Z. Lin, L. Zhigilei, & V. Celli. *Electron-phonon coupling and electron heat capacity of metals under conditions of strong electron-phonon nonequilibrium.* Physical Review B **77**, 7, (2008) 075133.

[Lin14] Y.-C. Lin, C.-Y. S Chang, R. K. Ghosh, J. Li, H. Zhu, R. Addou, B. Diaconescu, T. Ohta, X. Peng, N. Lu, M. J. Kim, J. T. Robinson, R. M. Wallace, T. S. Mayer, S. Datta, L.-J. Li, & J. A. Robinson. *Atomically thin heterostructures based on single-layer tungsten diselenide and graphene.* Nano letters **14**, (2014) 6936.

[Lin15] Y.-C. Lin, R. K. Ghosh, R. Addou, N. Lu, S. M. Eichfeld, H. Zhu, M.-Y. Li, X. Peng, M. J. Kim, L.-J. Li, R. M. Wallace, S. Datta, & J. A. Robinson.

Atomically thin resonant tunnel diodes built from synthetic van der Waals heterostructures. Nature communications **6**, (2015) 7311.

[Lok12] D. Loke, T. H. Lee, W. J. Wang, L. P. Shi, R. Zhao, Y. C. Yeo, T. C. Chong, & S. R. Elliott. *Breaking the speed limits of phase-change memory.* Science **336**, 6088, (2012) 1566.

[Lok14] D. Loke, J. M. Skelton, W. J. Wang, T. H. Lee, R. Zhao, T. C. Chong, & S. R. Elliott. *Ultrafast phase-change logic device driven by melting processes.* Proceedings of the National Academy of Sciences **111**, (2014) 13272.

[Luc73] G. Lucovsky & R. White. *Effects of Resonance Bonding on the Properties of Crystalline and Amorphous Semiconductors.* Physical Review B **8**, 2, (1973) 660.

[Lye06] H. K. Lyeo, D. G. Cahill, B. S. Lee, J. R. Abelson, M. H. Kwon, K. B. Kim, S. G. Bishop, & B. K Cheong. *Thermal conductivity of phase-change material* $Ge_2Sb_2Te_5$. Applied Physics Letters **89**, (2006) 151904.

[Mak10] K. F. Mak, C. Lee, J. Hone, J. Shan, & T. F. Heinz. *Atomically thin* MoS_2*: A new direct-gap semiconductor.* Physical Review Letters **105**, (2010) 136805.

[Mak12] Ki. F. Mak, K. He, Ji. Shan, & T. F. Heinz. *Control of valley polarization in monolayer* MoS_2 *by optical helicity.* Nature Nanotechnology **7**, (2012) 494.

[Man12] G. F. Mancini, B. Mansart, S. Pagano, Bas van der Geer, M. de Loos, & F. Carbone. *Design and implementation of a flexible beamline for fs electron diffraction experiments.* Nuclear Instruments and Methods in Physics Research A **691**, (2012) 113.

[Mar47] L. Marton & K. Bol. *Spherical Aberration of Compound Magnetic Lenses.* Journal of Applied Physics **18**, 6, (1947) 522.

[McM65] W. L. McMillan & J. M. Rowell. *Lead phonon spectrum calculated from superconducting density of states.* Physical Review Letters **14**, 4, (1965) 108.

[Mic08] A. M. Michalik, E. Ya. Sherman, & J. E. Sipe. *Theory of ultrafast electron diffraction: The role of the electron bunch properties.* Journal of Applied Physics **104**, 5, (2008) 054905.

[Mil10] R. J. D. Miller, R. Ernstorfer, M. Harb, M. Gao, C. T. Hebeisen, H. Jean-Ruel, C. Lu, G. Moriena, & G. Sciaini. *'Making the molecular movie': first frames.* Acta crystallographica Section A **66**, (2010) 137.

[Mis04] O. V. Misochko, M. Hase, K. Ishioka, & M. Kitajima. *Observation of an amplitude collapse and revival of chirped coherent phonons in bismuth.* Physical Review Letters **92**, (2004) 197401.

[Mue13] B. Y. Mueller & B. Rethfeld. *Relaxation dynamics in laser-excited metals under nonequilibrium conditions.* Physical Review B **87**, (2013) 035139.

[Nee86] R. J. Needs, R. M. Martin, & O. H. Nielsen. *Total-energy calculations of the structural properties of the group-V element arsenic.* Physical Review B **33**, 6, (1986) 3778.

[Něm09] P. Němec, A. Moreac, V. Nazabal, M. Pavlišta, J. Přikryl, & M. Frumar. *Ge-Sb-Te thin films deposited by pulsed laser: An ellipsometry and Raman scattering spectroscopy study.* Journal of Applied Physics **106**, (2009) 103509.

[Nie06] S. Nie, X. Wang, H. Park, R. Clinite, & J. Cao. *Measurement of the Electronic Grüneisen Constant Using Femtosecond Electron Diffraction.* Physical Review Letters **96**, 2, (2006) 025901.

[Nov04] K. S. Novoselov, A. K. Geim, S. V. Morozov, D. Jiang, Y. Zhang, S. V. Dubonos, I. V. Grigorieva, & A. A. Firsov. *Electric field effect in atomically thin carbon films.* Science **306**, (2004) 666.

[Nov05a] K. S. Novoselov, A. K. Geim, S. V. Morozov, D. Jiang, M. I. Katsnelson, I. V. Grigorieva, S. V. Dubonos, & A. A. Firsov. *Two-dimensional gas of massless Dirac fermions in graphene.* Nature **438**, (2005) 197.

[Nov05b] K. S. Novoselov, D. Jiang, F. Schedin, T. J. Booth, V. V. Khotkevich, S. V. Morozov, & A. K. Geim. *Two-dimensional atomic crystals.* Proceedings of the National Academy of Sciences of the United States of America **102**, 30, (2005) 10451.

[Nov12] K. S. Novoselov, V. I. Fal'ko, L. Colombo, P. R. Gellert, M. G. Schwab, & K. Kim. *A roadmap for graphene.* Nature **490**, 7419, (2012) 192.

[Ols06] J. K. Olson, Heng Li, T. Ju, J. M. Viner, & P. C. Taylor. *Optical properties of amorphous GeTe, Sb_2Te_3, and $Ge_2Sb_2Te_5$: The role of oxygen.* Journal of Applied Physics **99**, (2006) 103508.

[Ovs68] S. R. Ovshinsky. *Reversible electrical switching phenomena in disordered structures.* Physical Review Letters **21**, 20, (1968) 1450.

[Pal84] S. L. Palfrey & T. F. Heinz. *Coherent interactions in pump-probe absorption measurements: the effect of phase gratings.* Journal of the Optical Society of America B **2**, 4, (1984) 674.

[Pap12] E. Papalazarou, J. Faure, J. Mauchain, M. Marsi, A. Taleb-Ibrahimi, I. Reshetnyak, A. Van Roekeghem, I. Timrov, N. Vast, B. Arnaud, & L. Perfetti. *Coherent phonon coupling to individual Bloch states in photoexcited bismuth.* Physical Review Letters **108**, (2012) 256808.

[Par09] J. W. Park, S. H. Eom, H. Lee, J. L. F. Da Silva, Y. S. Kang, T. Y. Lee, & Y. H. Khang. *Optical properties of pseudobinary GeTe, $Ge_2Sb_2Te_5$, $GeSb_2Te_4$, $GeSb_4Te_7$, and Sb_2Te_3 from ellipsometry and density functional theory.* Physical Review B **80**, (2009) 115209.

[Pat79] A. R. Patel, K. V. Rao, & G. K. Shivakumar. *Initial stages of growth and orientation of bismuth and antimony films.* Journal of Materials Science **14**, (1979) 483.

[Pat10] J. Patterson & B. Bailey (Hg.). *Solid-State Physics.* Springer Verlag Berlin Heidelberg, 2010.

[Pen04] L. M. Peng, S. L. Dudarev, & M. J. Whelan. *High-Energy Electron Diffraction and Microscopy.* Oxford Science Publications, 2004.

[Plu03] E. W. Plummer, J. Shi, S. J. Tang, E. Rotenberg, & S. D. Kevan. *Enhanced electron-phonon coupling at metal surfaces.* Progress in Surface Science **74**, (2003) 251.

[Poe15] C. Poellmann, P. Steinleitner, U. Leierseder, P. Nagler, G. Plechinger, M. Porer, R. Bratschitsch, C. Schüller, T. Korn, & R. Huber. *Resonant internal quantum transitions and femtosecond radiative decay of excitons in monolayer WSe_2.* Nature Materials **14**, (2015) 889.

[Pol10] D. Polli, D. Brida, S. Mukamel, G. Lanzani, & G. Cerullo. *Effective temporal resolution in pump-probe spectroscopy with strongly chirped pulses.* Physical Review A **82**, 5, (2010) 053809.

[Qia03] B. L. Qian & H. E. Elsayed-Ali. *Comment on "Ultrafast electron optics: Propagation dynamics of femtosecond electron packets" [J. Appl. Phys. 92, 1643 (2002)].* Journal of Applied Physics **94**, 1, (2003) 803.

[Qiu13] D. Y. Qiu, F. H. Da Jornada, & S. G. Louie. *Optical spectrum of MoS_2: Many-body effects and diversity of exciton states.* Physical Review Letters **111**, (2013) 216805.

[Rad11] B. Radisavljevic, A. Radenovic, J. Brivio, V. Giacometti, & A. Kis. *Single-layer MoS_2 transistors.* Nature nanotechnology **6**, (2011) 147.

[Ram11] A. Ramasubramaniam, D. Naveh, & E. Towe. *Tunable band gaps in bilayer transition-metal dichalcogenides.* Physical Review B **84**, (2011) 205325.

[Ram12] A. Ramasubramaniam. *Large excitonic effects in monolayers of molybdenum and tungsten dichalcogenides.* Physical Review B **86**, (2012) 115409.

[Rao09] S. Raoux & M. Wuttig (Hg.). *Phase Change Materials - Science and Applications.* Springer Science+Business Media, 2009.

[Rec06] V. Recoules, J. Clérouin, G. Zérah, P. Anglade, & S. Mazevet. *Effect of Intense Laser Irradiation on the Lattice Stability of Semiconductors and Metals.* Physical Review Letters **96**, 5, (2006) 055503.

[Rif07] D. M. Riffe & A. J. Sabbah. *Coherent excitation of the optic phonon in Si: Transiently stimulated Raman scattering with a finite-lifetime electronic excitation.* Physical Review B **76**, (2007) 085207.

[Ril14] J. M. Riley, F. Mazzola, M. Dendzik, M. Michiardi, T. Takayama, L. Bawden, C. Granerød, M. Leandersson, T. Balasubramanian, M. Hoesch, T. K. Kim, H. Takagi, W. Meevasana, P. Hofmann, M. S. Bahramy, J. W. Wells, & P. D. C. King. *Direct observation of spin-polarized bulk in an semiconductor bulk inversion-symmetric.* Nature Physics **10**, (2014) 835.

[Rio14] C. Rios, P. Hosseini, C. D. Wright, H. Bhaskaran, & W. H. P. Pernice. *On-chip photonic memory elements employing phase-change materials.* Advanced Materials **26**, (2014) 1372.

[Riv15] P. Rivera, J. R. Schaibley, A. M. Jones, J. S. Ross, S. Wu, G. Aivazian, P. Klement, K. Seyler, G. Clark, N. J Ghimire, J. Yan, D. G. Mandrus, W. Yao, & X. Xu. *Observation of long-lived interlayer excitons in monolayer $MoSe_2$-WSe_2 heterostructures.* Nature communications **6**, (2015) 6242.

[Ros86] M. J. Rosker, F. W. Wise, & C. L. Tang. *Femtosecond relaxation dynamics of large molecules.* Physical Review Letters **57**, 3, (1986) 321.

[Rud13] M. Rudé, J. Pello, R. E. Simpson, J. Osmond, G. Roelkens, J. J. G. M. van der Tol, & V. Pruneri. *Optical switching at 1.55 μm in silicon racetrack resonators using phase change materials.* Applied Physics Letters **103**, (2013) 141119.

[Sac66] W. M. H. Sachtler, G. J. H. Dorgelo, & A. A. Holscher. *The work function of gold.* Surface Science **5**, (1966) 221.

[Sch83] B. Schönfeld, J. J. Huang, & S. C. Moss. *Anisotropic mean-square displacements (MSD) in single-crystals of 2H- and 3R-MoS_2.* Acta Crystallographica B **39**, 1976, (1983) 404.

[Sch87a] R. W. Schoenlein, W. Z. Lin, J. G. Fujimoto, & G. L. Eesley. *Femtosecond studies of nonequilibrium electronic processes in metals.* Physical Review Letters **58**, 16, (1987) 1680.

[Sch87b] W. J. Schutte, J. L. De Boer, & F. Jellinek. *Crystal structures of tungsten disulfide and diselenide.* Journal of Solid State Chemistry **70**, (1987) 207.

[Sch10] F. Schwierz. *Graphene transistors.* Nature Nanotechnology **5**, 7, (2010) 487.

[Sch11] S. Schäfer, W. Liang, & A. H. Zewail. *Primary structural dynamics in graphite.* New Journal of Physics **13**, (2011) 063030.

[Sci09] G. Sciaini, M. Harb, S. G Kruglik, T. Payer, C. T. Hebeisen, F. J. Meyer zu Heringdorf, M. Yamaguchi, M. Horn-von Hoegen, R. Ernstorfer, & R. J. Dwayne Miller. *Electronic acceleration of atomic motions and disordering in bismuth.* Nature **458**, 7234, (2009) 56.

[Sea91] V. F. Sears & S. A. Shelley. *Debye-Waller Factor for Elemental Crystals.* Acta Crystallographica A **47**, (1991) 441.

[Sen13] M. Sentef, A. F. Kemper, B. Moritz, J. K. Freericks, Z.-X. Shen, & T. P. Devereaux. *Examining Electron-Boson Coupling Using Time-Resolved Spectroscopy.* Physical Review X **3**, 4, (2013) 041033.

[She84] D. Shechtman, I. Blech, D. Gratias, & J. W. Cahn. *Metallic phase with long-range orientational order and no translational symmetry.* Physical Review Letters **53**, 20, (1984) 1951.

[Shi13] H. Shi, R. Yan, S. Bertolazzi, J. Brivio, B. Gao, A. Kis, D. Jena, H. G. Xing, & L. Huang. *Exciton dynamics in suspended monolayer and few-layer MoS_2 2D crystals.* ACS Nano **7**, 2, (2013) 1072.

[Shi14] T. Shin, J. W. Wolfson, S. Teitelbaum, M. Kandyla, & K. A. Nelson. *Dual Echelon Femtosecond Single-Shot Spectroscopy.* Review of Scientific Instruments **85**, (2014) 083115.

[Shk04] I. A. Shkrob, D. A. Oulianov, R. A. Crowell, & S. Pommeret. *Frequency-domain "single-shot" ultrafast transient absorption spectroscopy using chirped laser pulses.* Journal of Applied Physics **96**, 1, (2004) 25.

[Shp08] K. Shportko, S. Kremers, M. Woda, D. Lencer, J. Robertson, & M. Wuttig. *Resonant bonding in crystalline phase-change materials.* Nature Materials **7**, 8, (2008) 653.

[Siw02] B. J. Siwick, J. R. Dwyer, R. E. Jordan, & R. J. D. Miller. *Ultrafast electron optics: Propagation dynamics of femtosecond electron packets.* Journal of Applied Physics **92**, 3, (2002) 1643.

[Siw03] B. J. Siwick, J. R. Dwyer, R. E. Jordan, & R. J. D. Miller. *An atomic-level view of melting using femtosecond electron diffraction.* Science **302**, 5649, (2003) 1382.

[Sos75] I. Sosnowska, P. Fischer, & W. von Wartburg. *Temperature factors of polycrystalline arsenic, antimony and bismuth in the low-temperature range.* Journal of Physics C **8**, (1975) 1144.

[Spl10] A. Splendiani, L. Sun, Y. Zhang, T. Li, J. Kim, C. Y. Chim, G. Galli, & F. Wang. *Emerging photoluminescence in monolayer MoS_2.* Nano Letters **10**, (2010) 1271.

[ST98] K. Sokolowski-Tinten, J. Solis, J. Bialkowski, J. Siegel, C. Afonso, & D. von der Linde. *Dynamics of Ultrafast Phase Changes in Amorphous GeSb Films.* Physical Review Letters **81**, 17, (1998) 3679.

[ST03] K. Sokolowski-Tinten, C. Blome, J. Blums, A. Cavalleri, C. Dietrich, A. Tarasevitch, I. Uschmann, E. Förster, M. Kammler, M. Horn-von-Hoegen, & D. von der Linde. *Femtosecond X-ray measurement of coherent lattice vibrations near the Lindemann stability limit.* Nature **422**, 222, (2003) 287.

[Ste67] R. Stedman, L. Almqvist, & G. Nilsson. *Phonon-frequency distributions and heat capacities of aluminum and lead.* Physical Review **162**, 3, (1967) 549.

[Ste83] G. R. Stewart. *Measurement of low-temperature specific heat.* Review of Scientific Instruments **54**, (1983) 1.

[Ste02] T. Stevens, J. Kuhl, & R. Merlin. *Coherent phonon generation and the two stimulated Raman tensors.* Physical Review B **65**, 14, (2002) 144304.

[Sti12] J. Stingl, F. Zamponi, B. Freyer, M. Woerner, T. Elsaesser, & A. Borgschulte. *Electron transfer in a virtual quantum state of $LiBH_4$ induced by strong optical fields and mapped by femtosecond x-ray diffraction.* Physical Review Letters **109**, (2012) 147402.

[Sto14] L. Stojchevska, I. Vaskivskyi, T. Mertelj, P. Kusar, D. Svetin, S. Brazovskii, & D. Mihailovic. *Ultrafast switching to a stable hidden quantum state in an electronic crystal.* Science **344**, (2014) 177.

[Tan10] X. Tang, C. W. Li, & B. Fultz. *Anharmonicity-induced phonon broadening in aluminum at high temperatures.* Physical Review B **82**, (2010) 184301.

[Tri10] M. Trigo, J. Chen, V. H. Vishwanath, Y. M. Sheu, T. Graber, R. Henning, & D. A. Reis. *Imaging nonequilibrium atomic vibrations with x-ray diffuse scattering.* Physical Review B **82**, (2010) 235205.

[Tri13] M. Trigo, M. Fuchs, J. Chen, M. P. Jiang, M. Cammarata, S. Fahy, D. M. Fritz, K. Gaffney, S. Ghimire, a. Higginbotham, S. L. Johnson, M. E. Kozina, J. Larsson, H. Lemke, a. M. Lindenberg, G. Ndabashimiye, F. Quirin, K. Sokolowski-Tinten, C. Uher, G. Wang, J. S. Wark, D. Zhu, & D. a. Reis. *Fourier-transform inelastic X-ray scattering from time- and momentum-dependent phonon-phonon correlations.* Nature Physics **9**, 12, (2013) 790.

[vO07] T. van Oudheusden, E. F. de Jong, S. B. van der Geer, W. P. E. M. Op 't Root, O. J. Luiten, & B. J. Siwick. *Electron source concept for single-shot sub-100 fs electron diffraction in the 100 keV range.* Journal of Applied Physics **102**, 9, (2007) 093501.

[Wak00] G. P. Wakeham & K. A. Nelson. *Dual-echelon single-shot femtosecond spectroscopy.* Optics letters **25**, 7, (2000) 505.

[Wal56] C. B. Walker. *X-Ray Study of Lattice Vibrations.* Physical Review **103**, 3, (1956) 547.

[Wal12] S. Wall, D. Wegkamp, L. Foglia, K. Appavoo, J. Nag, R. F. Haglund, J. Stähler, & M. Wolf. *Ultrafast changes in lattice symmetry probed by coherent phonons.* Nature communications **3**, (2012) 721.

[Wal15a] L. Waldecker, R. Bertoni, & R. Ernstorfer. *Compact femtosecond electron diffractometer with 100 keV electron bunches approaching the single-electron pulse duration limit.* Journal of Applied Physics **117**, (2015) 044903.

[Wal15b] L. Waldecker, T. A. Miller, M. Rude, R. Bertoni, J. Osmond, V. Pruneri, R. Simpson, R. Ernstorfer, & S. Wall. *Time-domain separation of optical properties from structural transitions in resonantly bonded materials.* Nature Materials **14**, (2015) 991.

[Wal16] L. Waldecker, R. Bertoni, J. Vorberger, & R. Ernstorfer. *Electron-phonon coupling and energy flow in a simple metal beyond the two-temperature approximation.* Physical Review X **6**, (2016) 021003.

[Wan94] X. Y. Wang, D. M. Riffe, Y.-S. Lee, & M. C. Downer. *Time-resolved electron-temperature measurement in a highly excited gold target using femtosecond thermionic emission.* Physical Review B **50**, (1994) 8016.

[Wan12] Q. H. Wang, K. Kalantar-Zadeh, A. Kis, J. N. Coleman, & M. S. Strano. *Electronics and optoelectronics of two-dimensional transition metal dichalcogenides.* Nature Nanotechnology **7**, 11, (2012) 699.

[Wen12] C. Weninger & P. Baum. *Temporal distortions in magnetic lenses.* Ultramicroscopy **113**, (2012) 145.

[Whi72] G. K. White. *Thermal expansion of trigonal elements at low temperatures: As, Sb and Bi.* Journal of Physics C **5**, (1972) 2731.

[Wil69] J. A. Wilson & A.D. Yoffe. *The transition metal dichalcogenides Discussion and interpretation of the observed optical, electrical and structural properties.* Advances in Physics **18**, 73, (1969) 193.

[Wil84] S. Williamson, G. Mourou, & J. C. M. Li. *Time-resolved, laser-induced phase transformation in aluminum.* Physical Review Letters **52**, 26, (1984) 2364.

[Wil97] T. Wilhelm, J. Piel, & E. Riedle. *Sub-20-fs pulses tunable across the visible from a blue-pumped single-pass noncollinear parametric converter.* Optics letters **22**, 19, (1997) 1494.

[Wut05] M. Wuttig. *Phase-change materials: Towards a universal memory?* Nature Materials **4**, (2005) 265.

[Xia12] D. Xiao, G.-B. Liu, W. Feng, X. Xu, & W. Yao. *Coupled Spin and Valley Physics in Monolayers of MoS_2 and Other Group-VI Dichalcogenides.* Physical Review Letters **108**, (2012) 196802.

[Xu13] M. Xu, T. Liang, M. Shi, & H. Chen. *Graphene-Like Two-Dimensional Materials.* Chemical Reviews **113**, (2013) 3766.

[Xu14] X. Xu, W. Yao, D. Xiao, & T. F. Heinz. *Spin and pseudospins in layered transition metal dichalcogenides.* Nature Physics **10**, (2014) 343.

[Ye14] Z. Ye, T. Cao, K. O'Brien, H. Zhu, X. Yin, Y. Wang, S. G. Louie, & X. Zhang. *Probing Excitonic Dark States in Single-layer Tungsten Disulfide.* Nature **513**, (2014) 214.

[Yu13] W. J. Yu, Y. Liu, H. Zhou, A. Yin, Z. Li, Y. Huang, & X. Duan. *Highly efficient gate-tunable photocurrent generation in vertical heterostructures of layered materials.* Nature Nanotechnology **8**, (2013) 952.

[Zei92] H. J. Zeiger, J. Vidal, T. K. Cheng, E. P. Ippen, G. Dresselhaus, & M. S. Dresselhaus. *Theory for displacive excitation of coherent phonons.* Physical Review B **45**, 2, (1992) 768.

[Zen12] H. Zeng, J. Dai, W. Yao, D. Xiao, & X. Cui. *Valley polarization in MoS2 monolayers by optical pumping.* Nature nanotechnology **7**, 8, (2012) 490.

[Zha13] W. Zhao, Z. Ghorannevis, L. Chu, M. Toh, C. Kloc, P. H. Tan, & G. Eda. *Evolution of Electronic Structure in Atomically Thin Sheets of WS_2 and WSe_2.* ACS nano **7**, 1, (2013) 791.

[Zha14] X. Zhang, Q. Liu, J.-W. Luo, A. J. Freeman, & A. Zunger. *Hidden spin polarization in inversion-symmetric bulk crystals.* Nature Physics **10**, (2014) 387.

[Zhu13] P. Zhu, J. Chen, R. Li, L. Chen, J. Cao, Z. Sheng, & J. Zhang. *Laser-induced short-range disorder in aluminum revealed by ultrafast electron diffuse scattering.* Applied Physics Letters **103**, 23, (2013) 231914.

[Zhu15] D. Zhu, A. Robert, T. Henighan, H. T. Lemke, M. Chollet, J. M. Glownia, D. A. Reis, & M. Trigo. *Phonon spectroscopy with sub-meV resolution by femtosecond x-ray diffuse scattering.* Physical Review B **92**, (2015) 054303.

[Zij06] E. S. Zijlstra, L. L. Tatarinova, & M. E. Garcia. *Laser-induced phonon-phonon interactions in bismuth.* Physical Review B **74**, (2006) 220301.

List of Publications

Publications within this thesis

L. Waldecker, R. Bertoni, R. Ernstorfer, *Compact femtosecond electron diffractometer with 100 keV electron bunches approaching the single-electron pulse duration limit*, Journal of Applied Physics **117**, (2015), 044903

L. Waldecker, T. Miller, M. Rude, R. Bertoni, J. Osmond, V. Pruneri, R. Simpson, R. Ernstorfer, S. Wall, *Decoupled optical response and structural transition in phase change materials*, Nature Materials **14**, (2015), 991

L. Waldecker, R. Bertoni, J. Vorberger, R. Ernstorfer, *Electron-Phonon Coupling and Energy Flow in a Simple Metal beyond the Two-Temperature Approximation*, Physical Review X **6**, (2016), 021003

Publications concerning other topics

L. Waldecker, P. Heissler, R. Hörlein, K. Allinger, M. Heigoldt, K. Khrennikov, J. Wenz, S. Karsch, F. Krausz, G. D. Tsakiris, *Focusing of high order harmonics from solid density plasmas*, Plasma Physics and Controlled Fusion **53**, (2011), 124021

P. Heissler, P. Tzallas, J. M. Mikhailova, K. Khrennikov, L. Waldecker, F. Krausz, S. Karsch, D. Charalambidis, G. D. Tsakiris, *Two-photon above-threshold ionization using extreme-ultraviolet harmonic emission from relativistic laser-plasma interaction*, New Journal of Physics **14**, (2012), 043025

P. Heissler, R. Hörlein, J. M. Mikhailova, L. Waldecker, P. Tzallas, A. Buck, K. Schmid, C. M. S. Sears, F. Krausz, L. Veisz, M. Zepf, G. D. Tsakiris, *Few-Cycle driven relativistically oscillating plasma mirrors: a source of intense isolated attosecond pulses*, Physical Review Letters **108**, (2012), 235003

P. Heissler, E. Lugovoy, R. Hörlein, L. Waldecker, J. Wenz, M. Heigoldt, K. Khrennikov, S. Karsch, F. Krausz, B. Abel, G. D. Tsakiris, *Using the third state of matter: high harmonic generation from liquid targets*,
New Journal of Physics **16**, (2014), 113045

Acknowledgments

I would like to thank everyone who took part and helped in the work related to this thesis.

Many thanks to Ralph Ernstorfer, who provided the opportunity to start a new project in his group. He shared his knowledge about electron diffraction, but nevertheless gave me the freedom to try out things myself and make my own mistakes. Thanks for the continuous help and support.

Thanks to everyone in the group for the continously nice atmosphere, which is one of the most important reasons for me enjoying the last years. These are, again, Ralph Ernstorfer, Roman Bertoni, who joined me in the lab (and for Pétanque and Pastis), Melanie Müller and Alex Paarmann, who were particularly helping in the planning of the setup, Michele Puppin, Thomas Vasileiadis, Yunpei Deng, Sebastian Lüneburg and Jannik Malter, who, in between school and university, wrote most of the software for the experiment.

In the same spirit thanks to everyone in the departement for making life here most enjoyable, especially Jan, Daniel, Clemens, Lea, Laura, Selene, Marc, Sebastian, Lukas ... I hope I din't forget anyone. Thanks to Martin Wolf for providing the environment in which all the experiments and the exchange with everyone from the department takes place.

Thanks to Simon Wall, with whom I spent some time in the lab, and probably even more time in the bars of Berlin and Barcelona and who stayed in close contact while discussing the GST data and writing the paper (884 emails...). Thanks also to Timothy Miller and all other people from Barcelona.

Thanks to Jan Vorberger, who contributed on the interpretation of the measurements on aluminiun and in writing the paper.

I would like to thank Martin Weinelt for setting up and coordinating the graduate school 'Dynamics in new Light' (DinL), which provided nice seminars and helped establishing contact to phD students from other groups in Berlin and Potsdam.

Thanks to all technicians, especially Sven Kubala, Albrecht Ropers, Marcel Krenz and Pascal Thuge for their assistance.

My gratitude to Emma, my parents, grandparents and my sister, who have continuously given their full support.